Department of Physics and Astronomy

University of Heidelberg, Germany

Master's thesis in Physics

submitted by

Gergana Dimitrova Borisova

born in Novi pazar (Bulgaria)

1 December 2017

Theoretical and Experimental Studies of XUV Multielectron (Auto-)Ionization Dynamics in Helium and Molecular Hydrogen

This Master's thesis has been carried out by

Gergana Dimitrova Borisova

at the MAX-PLANCK-INSTITUT FÜR KERNPHYSIK in Heidelberg

under the supervision of

Prof. Dr. Thomas Pfeifer

Theoretical and Experimental Studies of XUV Multielectron (Auto-)Ionization Dynamics in Helium and Molecular Hydrogen

This work consists of two parts: theoretical studies of laser-intensity dependent ionization processes in the helium atom and experimental attosecond transient-absorption spectroscopy studies of the (auto-)ionization dynamics of the Q_n resonances of molecular hydrogen. In an experiment, motivating the simulations of ionization processes in helium, abrupt ionization of doubly excited states above a certain critical NIR-laser intensity was observed. Numerically solving the quantum-mechanical one-dimensional time-dependent Schrödinger equation for two electrons, the time-dependent population of relevant atomic states during the laser-pulse interaction is directly accessed. With respect to the theoretical results, an ionization mechanism for the doubly excited states is suggested, where non-sequential double ionization, arising due to electron–electron interaction, plays an important role. The investigations of the (auto-)ionization processes of doubly excited states in the hydrogen molecule concentrated on measuring time- and energy-dependent XUV absorption signals to separate the autoionization effects from the overall continuum absorption of H_2. First results of (auto-)ionization effects in the hydrogen molecule were obtained in a technically challenging absorption spectroscopy study.

Theoretische und experimentelle Untersuchungen der XUV Multielektronen- und (Auto-)Ionisationsdynamiken in Helium und molekularem Wasserstoff

Diese Arbeit besteht aus zwei Teilen: Theoretische Studien von Ionisationsprozessen in atomarem Helium, abhängig von der Laser-Intensität, und Experimente mittels Attosekunden zeitaufgelöster Absorptionspektroskopie, die die (Auto-)Ionisationsdynamik der Q_n-Resonanzen in molekularem Wasserstoff untersuchen. Motiviert durch experimentelle Ergebnisse, bei denen abrupte Ionisation der doppelt angeregten Zustände ab einer gewissen kritischen NIR-Laserintensität auftrat, wurden Simulationen der Ionisationsprozesse in Helium durchgeführt. Durch numerisches Lösen der zeitabhängigen eindimensionalen Schrödinger Gleichung für zwei Elektronen, erhält man direkten Zugriff auf die zeitabhängige Population von relevanten atomaren Zuständen während der Wechselwirkung mit dem Laserpuls. Die theoretischen Ergebnisse deuten auf einen Ionisationsmechanismus für doppelt angeregte Zustände hin, bei dem, aufgrund der Elektron-Elektron Wechselwirkung, nichtsequentielle Doppelionisation eine signifikante Rolle spielt. Die Untersuchungen von (Auto-)Ionisationsprozessen in Wasserstoff-Molekülen haben sich auf Messungen von zeit- und energieabhängigen XUV Absorptionssignalen konzentriert, um die Autoionisationseffekte von der Kontinuumsabsorption in H_2 zu trennen. Erste Hinweise auf (Auto-)Ionisationseffekte in molekularem Wasserstoff wurden in einem technisch anspruchvollen Absorptionsexperiment gemessen.

Abbreviations and Symbols

ADK	after M. V. Ammosov, N. B. Delone and V. P. Krainov
AOFS	Acousto-Optical Frequency Shifter
BS	Beam Splitter
CCD	Charge-Coupled Device
CEO	Cerrier-Envelope Offset
CEP	Carrier-Envelope Phase
CPA	Chirped Pulse Amplification
DES	Doubly Excited State
DFG	Difference Frequency Generation
DI	Double Ionization
DIY	Double Ionization Yield
D-Scan	Dispersion Scan
FEL	Free-Electron Laser
FWHM	Full Width at Half Maximum
HHG	High-order Harmonic Generation
MCP	MicroChannel Plate
NF	Notch Filter
NIR	Near-InfraRed
OD	Optical Density
SES	Singly Excited State
SFM	Self-Phase Modulation
SHG	Second Harmonic Generation
SI	Single Ionization
SIY	Single Ionization Yield
TAS	Transient Absorption Spectroscopy
TD	Time Delay
TD-Scan	Time-Delay Scan
TDSE	Time-Dependent Schrödinger Equation
Ti:Sa	Titanium-doped Sapphire

VLS	Variable Line Spacing
WF	Wave Function
XUV	eXtreme UltraViolet

Contents

Introduction

Each and every scientific publication, regardless of it being a letter or an article in a journal having or not the so-called high impact factor, a thesis on any research subject, a lecture book or even a specialized textbook, can give only a glimpse into the matter of a problem it is dealing with and by no means, no matter the author's effort of completeness, include everything ever written, discussed about or thought of a subject. Along the same lines, this master's thesis will only give a glimpse into the (auto-)ionization dynamics of atoms and molecules, or to be more precise: it will present theoretical and experimental work on XUV[1] multielectron (auto-)ionization dynamics in helium and molecular hydrogen, which the title already suggests.

The choice of the studied species, He and H_2, was not at all arbitrary. Both of them happen to be an exemplary system with two electrons, thus exhibiting electron-electron correlation: helium being a benchmark atomic system and the hydrogen dimer its molecular analogue. The two quantum systems are simple enough for one's mind to think of them but complex enough for their equations of motion (in the context of quantum mechanics – the time-dependent Schrödinger equation, TDSE) to not be analytically solvable. Furthermore, they are some of the most abundant species in the entire universe, thus being important to understand, or at least try to understand the ongoing processes in them. In either way, both atomic helium and molecular hydrogen have attracted plenty of theoretical as well as experimental interest over the last decades, after quantum theory was introduced at the beginning of the twentieth century.

The most substantial reason to study the dynamics of helium and hydrogen in the scope of this thesis is indeed the fact that they are the simplest systems with correlated electron dynamics having an effect on, for example, light–matter interaction processes. Having two electrons, if the two-electron wave function can be described in such a way, both He and H_2 can electronically be excited to doubly excited states (DESs) with eigenenergies above the corresponding first ionization threshold. All DESs of the two considered systems are thus embedded in the one-electron ionization continuum, which gives rise, for example, to autoionization, and in the case of H_2 to dissociation dynamics.

In helium, DES resonances have manifested themselves in photoabsorption spectra in the form of Fano resonances, being studied extensively in the last couple of decades [1, 2, 3, 4]. Possibly, because of the additional fast (a few femtoseconds[2]) dissociation dynamics, no Fano

[1] eXtreme UltraViolet

[2] 1 fs = 10^{-15} s

profiles have been encountered in absorption or photoionization-electron theoretical or experimental studies of molecular hydrogen so far. Thus, the nuclei could very likely introduce decoherence in the Fano interference mechanism, as addressed in [5] and references therein. Motivated by the works referenced here as well as other theoretical and experimental ones, for an overview see [6], treating the autoionization dynamics of doubly excited, Q_n resonances in hydrogen and similar systems like D_2, O_2 and HD, by detecting electrons, this thesis focuses on the possibility to study autoionization imprinted in absorption signals, Sec. 1. Such an absorption experiment, turned out to be extremely challenging because of the short autoionization lifetime of a lot of the Q_n states, 1 fs or less [7]. Despite all the difficulties in finding and correcting for systematical problems, absorption signatures giving an insight into the (auto-)ionization dynamics of molecular hydrogen have been detected, Cha. 4.

The chosen experimental approach to study (auto-)ionization in molecular hydrogen, namely the attosecond transient-absorption spectroscopy (ATAS) technique and the transient-coupling scheme, have extensively been employed to study (auto-)ionization dynamics in helium [2, 8, 3, 9, 4]. Even though a lot of multielectron effects in He have been investigated in great detail, there are still other multielectron quantum mechanisms from which new insights into its correlated electron dynamics can be gained. An experiment dealing with the ionization of both singly and doubly excited states in helium motivated a theoretical study with a view to gaining insight into the ongoing ionization dynamics, being dependent on the intensity of the NIR (Near-InfraRed) light pulses interacting with excited states (SESs[3] and DESs) populated after coherent XUV excitation, Cha. 3. The theoretical concepts of the two-dimensional TDSE simulations carried out can easily be transferred to the hydrogen system in a semiclassical two-nuclei extension of the two-electron model quantum system, as discussed in Sec. 4.4.

Of course, none of the work presented here, would have been possible without an appropriate experimental apparatus, Cha. 2. The one employed for the measurements, discussed in Cha. 3 and Cha. 4, consists of two major parts: a femtosecond LASER[4] system and a vacuum beamline for spectroscopic pump-probe studies with NIR and XUV laser pulses.

At the end of this thesis, as always, a summary of the main presented ideas is given.

[3] SES standing for Singly Excited State

[4] Light Amplification by Stimulated Emission of Radiation

Chapter 1

Theoretical Framework

Ionization is an integral part of the dynamics in the experiments, presented in this work. Therefore, an overview of the fundamental concepts, required to study ionization processes, is presented in this chapter. First of all, the attention is drawn to the systems under investigation in this thesis, the helium atom and the hydrogen molecule. Their structure, as well as the energy levels of helium and the potential energy curves of H_2, are represented in Section 1.1. After becoming familiar with the studied species, the experimental approach is introduced in Section 1.2.2. The basics of light-matter interactions, with emphasis on the ionization process, are summarized in Secs 1.2 and 1.3. Section 1.3.3 then points out the autoionization process as being of major importance in the ionization dynamics of doubly excited states in both atoms and molecules. At the end, two key experimental components are depicted: the production of XUV pulses by high-harmonic generation, Sec. 1.4.1, and the stabilization of the carrier-envelope phase of NIR pulses, Section 1.4.2, which is particularly important when making an effort of generating stable isolated attosecond pulses in the XUV spectral range, required for the experiments, discussed in Chapter 4.

1.1 Simplest Systems with Two Electrons

Apart for the strong and weak forces, keeping the nuclei of atoms and molecules together, the two other forces, acting inside such microscopic systems, are gravity and the electromagnetic force. Since all constituents of small atoms and molecules have relatively low masses, the gravitational force is usually neglected, drawing the attention of atom and molecular physicists to the electromagnetic force as the one, keeping atoms and molecules together. Here we should however bear in mind, that the electromagnetic force is charge-dependent, so that objects with opposite charge attract each other and those with same charge repel each other. Focusing on atoms and molecules with more than one electron, in the case of molecules also with at least two positively charged nuclei, one easily becomes aware of the fact, that such systems come to existence as stable chemical species, only if the acting attracting and repelling electromagnetic

forces are suitably balanced. This means, that if, for example, the electrons in the simplest atom with two of those, helium, or the nuclei of the simplest molecule, molecular hydrogen, are forced to come closer together than usual, both species could fall apart in the processes of autoionization and dissociation. To study those processes in systems exhibiting correlation, i.e. interactions, between their electrons, the aforementioned simplest two-electron systems - helium and molecular hydrogen - have become the subject of this work, where the dynamics of correlated electrons is investigated.

1.1.1 The Helium Atom

The most simple system with two electrons, being under investigation in the scope of this thesis, is the helium atom. It consists of two protons and two neutrons, bound together in a nucleus, and two electrons in the electron shell. The atomic structure of the atom will be discussed with a restriction to resonances, accessible via one-photon transitions from the ground state, with total spin quantum number $S = 0$, using linearly polarized radiation in the extreme ultraviolet spectral range. The accessible states are therefore of $^1\mathrm{P}^\mathrm{o}$-symmetry, where the notation $^{2S+1}L^\pi$ with quantum numbers for the total angular momentum $L \in \{0,1,2,\dots\} \cong \{\mathrm{S},\mathrm{P},\mathrm{D},\dots\}$ and total spin S is used. Furthermore, π represents the parity of L with "o" and "e", standing for odd and even parity, respectively. This means, that the considered singly and doubly excited states of helium, accessible from the $1s^2$ ground state, are spin singlet states with an antisymmetric spin wave function, assuring that the spatial wave function must be symmetric, obeying

Series	**State configuration**	**Energy (eV)**	**Energy (a.u.)**	**Decay rate (meV)**
Singly excited states, N=1	$1s^2$	0	0	
	1s2p	21.2180	0.77979	0.0074
	1s3p	23.0870	0.84847	0.0023
	1s4p	23.7421	0.87255	0.0010
	1s5p	24.0458	0.88371	0.0005
	1s6p	24.2110	0.88978	0.0003
	1s7p	24.3107	0.89345	0.0002
Doubly excited states, N=2	2s2p	60.147	2.2105	37.4
	$sp_{2,3+}$	63.658	2.3395	8.2
	$sp_{2,4+}$	64.466	2.3692	3.5
	$sp_{2,5+}$	64.816	2.3821	1.8
	$sp_{2,6+}$	65.000	2.3888	1.0
	$sp_{2,7+}$	65.110	2.3929	0.7
	$sp_{2,8+}$	65.179	2.3951	0.4

Table 1.1: Energies and decay rates of considered singly and doubly excited states in helium
The one-photon excitation of the ground state of helium to one of the listed states in the table is dipole allowed. Data taken from [10, 11, 12, 13].

Paili's exclusion principle for fermions.

Using broad-band XUV radiation, not only singly but also doubly excited states are accessible from the ground state of helium. The manifold of singly excited states with only one electron lifted above the 1s electron shell ranges from 21.22 eV, the energy level of the first excited state, up to the ionization threshold of the N = 1 manifold at 24.59 eV. The series of accessible singly excited states is denoted as 1snp, where $n = 2, 3, 4, \ldots$. The energy levels of those states, converging to the N = 1 ionization threshold, are listed in Table 1.1 together with the states' decay rate back to the ground state.

For energies above the first ionization threshold, one of the electrons can either ionize or both electrons are excited to higher states for energies higher than 60.15 eV. There are three dipole allowed N = 2 resonance series, the 2snp, 2pns and 2pnd series, which all converge to the N = 2 ionization threshold at 65.40 eV. The 2snp and 2pns configuration series can be populated with higher probability than the 2pnd series, since only one electron has to absorb angular momentum from the radiation field, whereas both electrons have to exchange angular momentum for excitations from the $1s^2$ ground state in the case of the 2pnd series. The upper probabilistic argument is also imprinted on the photo-absorption cross sections for the three mentioned series, i.e. it is much larger for the 2snp and 2pns, that is why only those two are considered in the scope of this work. The 2snp- and 2pns-states are energetically degenerate, so that superposition states

$$\mathrm{sp}_{2,n\pm} = \frac{1}{\sqrt{2}}\left(2\mathrm{s}n\mathrm{p} \pm 2\mathrm{p}n\mathrm{s}\right), \tag{1.1}$$

can be defined [14], where "+" describes the observed strong series, and "−" the weaker one. The energies of the here considered $\mathrm{sp}_{2,n+}$ series are summarized in Table 1.1.

1.1.2 Molecular Hydrogen

Not only the simplest atomic system with two electrons, exhibiting correlations, but also the simplest molecule with two electrons, hydrogen, has been an object of the studies in this work. Resonances in the hydrogen molecule could, just as in the case of helium, discussed in the previous section, be populated by XUV radiation. Here, again transitions from the $^1\Sigma_g^+$ ground state through a one-photon interaction are most probable, such that as a result of this, states with ungerade inversion symmetry are populated. The symmetry properties of a molecular state are given by the response of such a state upon transformations of the corresponding point group. The symmetry operations of the 2-electron homonuclear point group are the identity E, the rotation around the molecular axis C_∞^ϕ, reflection at planes including the molecular axis σ_v, inversion i, improper rotations around the molecular axis S_∞^ϕ and 2-fold rotations C_2, as described in [15] and references therein. All those symmetry operations build the point group of homonuclear diatomic molecules. The states, belonging to it, are labeled accordingly with the symbols $\Sigma_g^+, \Sigma_u^+, \Sigma_g^-, \Sigma_u^-, \Pi_g, \Pi_u, \Delta_g, \Delta_u, \ldots$, where the general notation follows $^{2S+1}\Lambda_{g,u}^{\pm}$, with $\pm$ for symmetry, antisymmetry under the σ_v transformation, S being the total spin and Λ the

Molecular state	Symmetry operations					
	E	C_∞^ϕ	σ_v	i	S_∞^ϕ	C_2
Σ_g^+	1	1	1	1	1	1
Σ_u^+	1	1	1	-1	-1	-1
Σ_g^-	1	1	-1	1	1	-1
Σ_u^-	1	1	-1	-1	-1	1
Π_g	2	$2\cos(\phi)$	0	2	$-2\cos(\phi)$	0
Π_u	2	$2\cos(\phi)$	0	-2	$2\cos(\phi)$	0
Δ_g	2	$2\cos(2\phi)$	0	2	$2\cos(\phi)$	0
Δ_u	2	$2\cos(2\phi)$	0	-2	$-2\cos(\phi)$	0

Table 1.2: Character table for the point group of a diatomic homonuclear molecule. The symmetry operation of the point group are the identity E, the rotation around the molecular axis C_∞^ϕ, reflection at planes including the molecular axis σ_v, inversion i, improper rotations around the molecular axis S_∞^ϕ and the 2-fold rotations C_2.

z-component of the total angular momentum ($\Sigma, \Pi, \Delta, \ldots$ stand for $1, 2, 3, \ldots$ and the subscript g,u for $\mathrm{sgn}(\Lambda) = 1, -1$, respectively). A character table for the point group of the hydrogen molecule, where each line describes one molecular state, is shown in Table 1.2.

Being a molecule, the energy levels in H_2 depend on the distance between its nuclei, so that potential energy curves become rather important. The potential energy curves for H_2 are shown in Fig. 1.1, adapted from [6] and [16]. In Fig. 1.1 (a) in full thick lines appear the $X^1\,\Sigma_g^+$ ground state of the neutral molecule, the six lowest states in H_2^+, $1s\sigma_g, 2p\sigma_u, 2p\pi_u, 2s\sigma_g, 3p\sigma_u$ and $3d\sigma_g$, each marking a single ionization threshold, and the double ionization threshold. The six lowest singly excited states of $^1\Sigma_u^+$ and $^1\Sigma_g^+$ symmetry below the first ionization threshold, i.e. the ground states of $H_2^+\ ^2\Sigma_g^+(1s\sigma_g)$, are also shown. Above the latter threshold and below the second $H_2^+\ ^2\Sigma_u^+(2p\sigma_u)$ ionization threshold the $Q_1\ ^1\Sigma_u^+$ and $Q_1\ ^1\Sigma_g^+$ doubly excited states of H_2 are displayed. Between the second and the third ionization threshold the $Q_2\ ^1\Sigma_u^+$ and $Q_2\ ^1\Sigma_g^+$ doubly excited states are plotted. Apart for showing all aforementioned potential curves, Fig. 1.1 (b) also shows the lowest Q_3 and Q_4 energy curves. The labels of the doubly excited states are based on the respective series limits, with the Q_1 states converging to the first excited state of the H_2-ion, Q_2 states to the second, Q_3 to the third, etc. The Q_1 and Q_2 states lie in the range around $26 - 45$ eV for the Franck-Condon region. Classically, this is the region, where vertical electronic transitions, without change in the position of the nuclei, are most likely to appear. The most fundamental assumption, leading to the Franck-Condon principle, is the Born-Oppenheimer approximation, separating the electronic and nuclear motion. All of the doubly excited states lie above the first ionization potential and could be thought of as superexcited Rydberg states, converging to excited states of the molecular ion. The doubly excited states are all repulsive in their nature and therefore perfectly suitable to study the competition between autoionization and neutral dissociation.

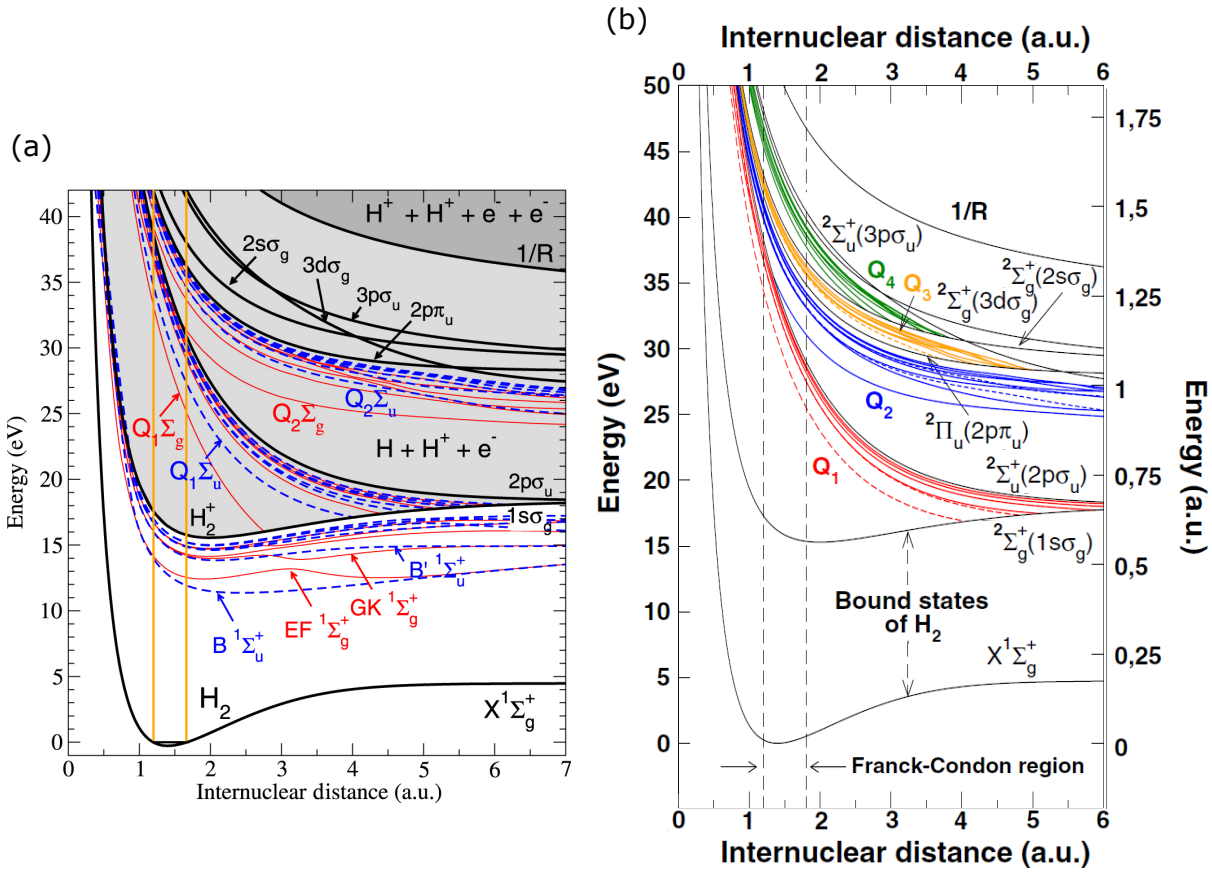

Figure 1.1: Potential energy curves of H_2 and H_2^+

Potential energy curves of some H_2 and H_2^+ states, relevant for the present study. The Franck-Condon region of highest overlap for transitions from the molecular ground state is confined between the two vertical lines, orange in **(a)** and dashed in **(b)**. All states above the first ionization threshold, the ground state of the H_2^+-ion, are plotted inside a gray shadowed area in **(a)**, emphasizing that all those states eventually ionize. **(b)** shows additional doubly excited states, the Q_3 and Q_4 resonances. Figures taken from [6] and [16] for **(a)** and **(b)**, respectively; adapted to be more easily comparable.

1.2 Light–Matter Interactions

The most common way to study quantum systems and processes occurring in them is by focusing on light–matter interactions. Those could be observed by a variety of optical approaches where a radiation field, i.e. light, is used as a probe for the studied material system. Most simply, the light–matter interaction could be described as a process, in which the incoming light of intensity $I_0(\omega)$ enters a black box, a material to be studied, is affected by the sample inside the black box, changing the throughput $I(\omega)$, which is then detected at the black box's exit, as shown in Fig. 1.2 (a). To resolve energy dependent properties of the black box photons, ions or changes in macroscopic properties of the studied matter sample can be detected. Most importantly, if the choice falls on photon detection, there is not only one exit of that very black box, or in other words, light could be detected in different directions, as shown in Fig. 1.2 (b). If we detect the directly transmitted light through the studied sample, then we are looking at an

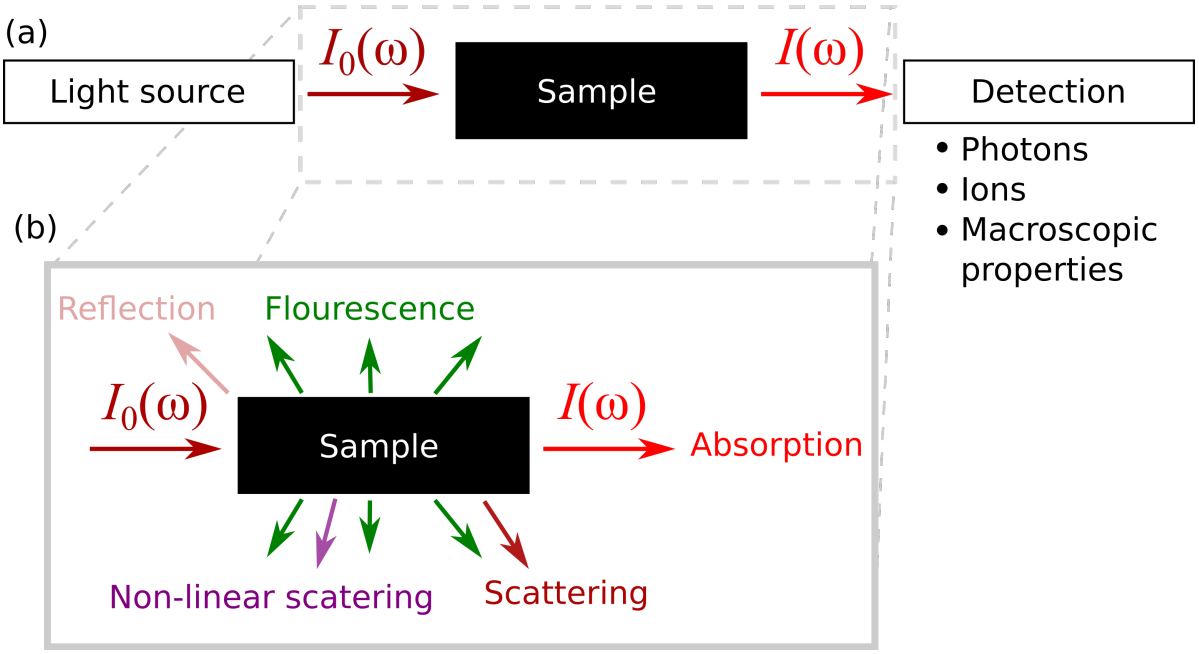

Figure 1.2: Detection of light-matter interactions
(a) General spectroscopy experiment. **(b)** Photon detection signals.

absorption signal. Placing a detector at other positions, we would be able to study reflection, fluorescence or scattering signals. In this work, absorption signals are detected and studied spectroscopically, so that a brief overview of the absorption process is presented in the next section.

1.2.1 Linear Absorption in Atoms and Molecules

One of the possibilities to look at an absorption signal is by determining the light attenuation by the studied spectroscopic sample, which according to the Lambert-Beer's law

$$I(\omega, z) = I_0(\omega) \cdot \mathrm{e}^{-\alpha(\omega) z} \tag{1.2}$$

gives access to the macroscopic absorption coefficient $\alpha(\omega)$ and thereby to the microscopic atomic/molecular absorption cross section $\sigma(\omega)$ via

$$\alpha(\omega) = \rho_{\mathrm{N}} \cdot \sigma(\omega), \tag{1.3}$$

where ρ_{N} denotes the number of illuminated atoms or molecules. The absorption cross section quantifies the probability that an absorber (atom or molecule of a given species in a particular excitation state and ionization level) will interact with an incident photon with energy $\hbar\omega$. For a given absorber, the cross section can vary by orders of magnitude as a function of ω. In the case of bound-bound transitions, the cross section has a narrow and large amplitude peak symmetrically centered on the resonance energy. In the case of bound-free transitions, the cross

section exhibits ionization edges, where absorption is only present for photon energies above the ionization potential. The dependency of the absorption cross section and all other quantities in equations (1.2) and (1.3) on ω, i.e. atomic energy, is explicitly shown, since it is of greatest interest in the spectroscopic studies, presented in this work.

Looking at the light–matter interaction in the studied absorption case from another perspective, one is able to obtain the absorption cross section in the following manner [17]:

Assuming once again a light beam, propagating through a gas of near resonant atoms, we recall the wave equation for the light electric field $\boldsymbol{E}(\boldsymbol{x},t)$ in homogeneous media without currents and charges

$$\left(\boldsymbol{\nabla}^2 - \frac{1}{c^2}\frac{\partial^2}{\partial t^2}\right)\boldsymbol{E}(\boldsymbol{x},t) = \mu_0 \frac{\partial^2}{\partial t^2}\boldsymbol{P}(\boldsymbol{x},t), \tag{1.4}$$

which in its one-dimensional form reads

$$\left(\frac{\partial^2}{\partial z^2} - \frac{1}{c^2}\frac{\partial^2}{\partial t^2}\right)E(z,t) = \mu_0 \frac{\partial^2}{\partial t^2}P(z,t). \tag{1.5}$$

Here μ_0 stands for the vacuum permeability and the linear polarization $\boldsymbol{P}(\boldsymbol{x},t)$, or $P(z,t)$, is given via the susceptibility χ by

$$P(z,t) = \epsilon_0 \int_0^\infty \chi(\tau)E(z,t-\tau)d\tau. \tag{1.6}$$

According to Eq. (1.6), after a Fourier transformation, the linear polarization can be related to the electric field in the frequency domain by

$$\tilde{P}(z,\omega) = \epsilon_0 \chi(\omega)\tilde{E}(z,\omega). \tag{1.7}$$

In general, $\chi(\omega)$ is a tensor quantity. However, in the linear approximation only its first order component is taken into account and the polarization is then just linearly proportional to the electric field, as denoted in eq. (1.7).

Assuming a plane wave for the electric field, propagating in z-direction, one easily arrives at the dispersion relation

$$k^2 - \frac{\omega^2}{c^2}(1+\chi(\omega)) = 0, \tag{1.8}$$

with its usual form, obtained by inserting the relation between the index of refraction n and the susceptibility $n = \sqrt{1+\chi(\omega)}$. Exploiting the complex notation, one can decompose $\chi(\omega)$ into a real and imaginary part,

$$\chi(\omega) = \chi'(\omega) + i\chi''(\omega). \tag{1.9}$$

For a dilute gas-phase sample $\chi(\omega)$ is smaller than unity, such that the complex wave number k can be approximated to

$$k \approx \frac{\omega}{c}\left(1 + \frac{\chi'(\omega)}{2} + \frac{i\chi''(\omega)}{2}\right), \tag{1.10}$$

where we recognize the real part of the complex wave number as related to the dispersion,

whereas the imaginary part relates to the absorption of a wave propagation in a medium, and define

$$\alpha(\omega) = \frac{\omega}{c}\chi''(\omega). \tag{1.11}$$

With this, we again arrive at an equation for the absorption coefficient $\alpha(\omega)$. Setting equations (1.3) and (1.11) to be equal, the atomic cross section is finally formulated as

$$\sigma(\omega) = \frac{1}{\rho_N}\frac{\omega}{c}\mathrm{Im}(\chi) = \frac{\omega}{\epsilon_0 c}\mathrm{Im}\left(\frac{\langle\mu(\omega)\rangle}{E(\omega)}\right), \tag{1.12}$$

for which we recall, that classically the polarization $\tilde{P}(z,\omega)$ is interpreted as the dipole moment per unit volume, or as the average dipole moment per atom or molecule $\langle\mu\rangle$, multiplied by the atomic number density ρ_N.

Coming back to the Lambert-Beer's law, we find that the attenuation of the light intensity, after passing through a sample of a length l, is proportional to the absorption cross section. Spectroscopic studies, looking for changes in $\sigma(\omega)$, quantify the cross section changes by a change in the observable $\mathrm{OD}(\omega)$, called optical density and defined through

$$\mathrm{OD}(\omega) = -\log_{10}\left(\frac{I(\omega)}{I_0(\omega)}\right) = \frac{\sigma(\omega)}{\ln 10}\cdot\rho_N\cdot l. \tag{1.13}$$

1.2.2 The Concept of Transient Absorption Spectroscopy

Traditionally, an absorption signal is detected using an absorption spectroscopy setup, for which an appropriate light source, a target to be investigated and a spectrometer with suitable resolution is needed, as indicated in the previous section. Recording the transmitted light from the light source trough the spectroscopic target and comparing it to reference spectra, one is then able to reconstruct static spectrally resolved absorption signals, revealing information about level spacing of the accessible states in the investigated target as well as the lifetime of those states. If one is however interested in the dynamics of the examined system, a time-resolved extension of the traditional absorption spectroscopy technique, in other words, the transient-absorption spectroscopy (TAS) scheme should be the preferred choice. As its name suggests, this technique reveals information about processes, which evolve in time, and are therefore not stationary. In order to access the time-evolution with the TAS technique, not only one but two light sources, usually short time-shifted laser pulses, are used, thus making TAS a pump-probe-scheme version of traditional absorption spectroscopy. In the pump-probe scheme a pump pulse, often stronger than the probe pulse, initiates some dynamics in the spectroscopy target. After a time delay τ, the effect of the pump pulse is probed by the probe pulse and is thus imprinted in the recorded probe signal. By varying the time separation between both pulses, the dynamics in the studied system is resolved in time. Changing the time delay between the laser pulses from negative to positive, one is able to exploit both the TAS scheme (for $\tau < 0$) as well as the transient-coupling scheme (for $\tau > 0$), in which a weak XUV pulse is used as a pump pulse

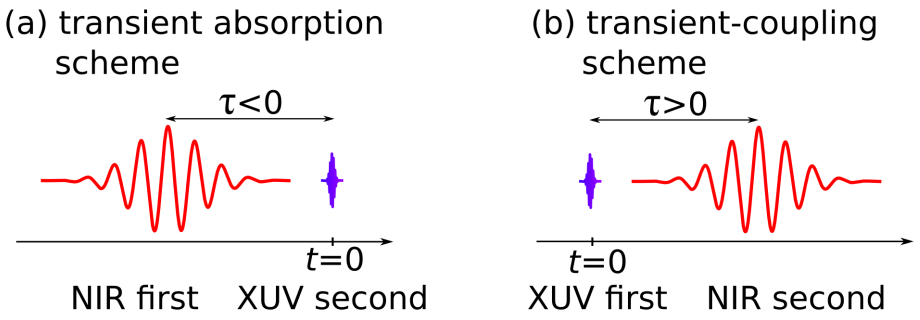

Figure 1.3: Pulse geometry in the used experimental scheme
(a) Transient absorption spectroscopy scheme with NIR pulse coming first and XUV pulse coming second, negative time delay between the pulses. **(b)** Transient-coupling scheme with an XUV pulse first and an NIR pulse afterwards, positive time delays.

and an NIR pulse as a probe. The role change of both pulses compared to the traditional TAS technique exploits the fact that the XUV excitation in the first step initiates temporal dynamics in the studied spectroscopic target inducing coherent dipole emission, which is present until all induced dynamics have naturally decayed. A perturbation with an NIR probe pulse in the life-span of the XUV-induced dynamics is then still imprinted in the measured collected absorption signal. Since at the end still the XUV-signal is detected, the two pulses are referred to as XUV-excitation and NIR-interaction pulse in the transient-coupling scheme. A sketch of the pulse geometry in the used experimental scheme is found in Fig. 1.3.

1.2.3 Photoabsorption Cross Sections of He and H_2

Going back to Eq. (1.13), it stands out, that the intrinsic quantity accessed in a spectroscopic experiment, which characterizes a quantum system, is the absorption cross section $\sigma(\omega)$. It is a measure of the probability of the absorption process at a particular energy to happen, encoding on top of the information about energy level spacing between bound states and transition types. Measuring time-dependent signals, hence detecting changes in $\sigma(\omega)$ for different time-delays between the XUV-excitation and NIR-interaction pulse, brings information about the evolution of the states population inside a quantum system. To be able to accurately interpret transient absorption signals, one should be familiar with calculations or experimental data of static absorption cross sections. Both theoretical and experimental interest in the He and H_2 systems have led to tons of publications of cross section data, e.g. [18]. Figure 1.4 and 1.5 show graphs of the photabsorption cross-section values in the relevant energetic regions for helium and molecular hydrogen, respectively.

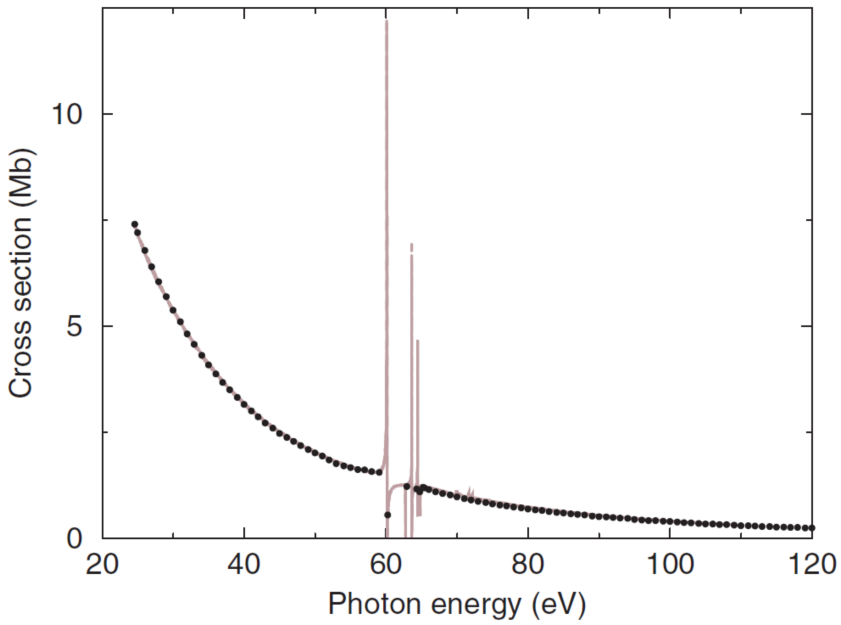

Figure 1.4: Helium photoionization cross section as a function of photon energy Experimental synchrotron data (black dots) and theoretical calculation (grey curve). Graph reprinted from [?].

1.3 Ionization Processes in Atoms and Molecules

The ionization process in both atoms and molecules is thoroughly investigated in the scope of this thesis. As shown in Chapter 1.1 and in Section 1.2.3, ion states of helium and molecular hydrogen can be easily accessed, when using XUV radiation to interact with He and H_2. Ionization can also occur as a result of interaction with less energetic photons, as those coming out of optical lasers with energy around 1 eV in the NIR spectral range. On the other side, we distinguish between single- and double ionization processes, i.e. processes leading to singly or doubly ionized atoms or molecules. Since the studied systems have 2 electrons in their neutral states, speaking of double ionization, the bare atomic or molecular core remains intact, whereas both electrons are removed from the corresponding system. Details about the possible ionization processes are summarized in this section.

1.3.1 Single-Ionization Processes

First and foremost, single ionization is discussed.

Single-Photon Ionization

The most natural way to think of single ionization is in the photon picture, and particularly, that an electron is removed from the neutral system after interaction with a single photon with energy at least as much as the ionization potential of the initial system's state. For single-

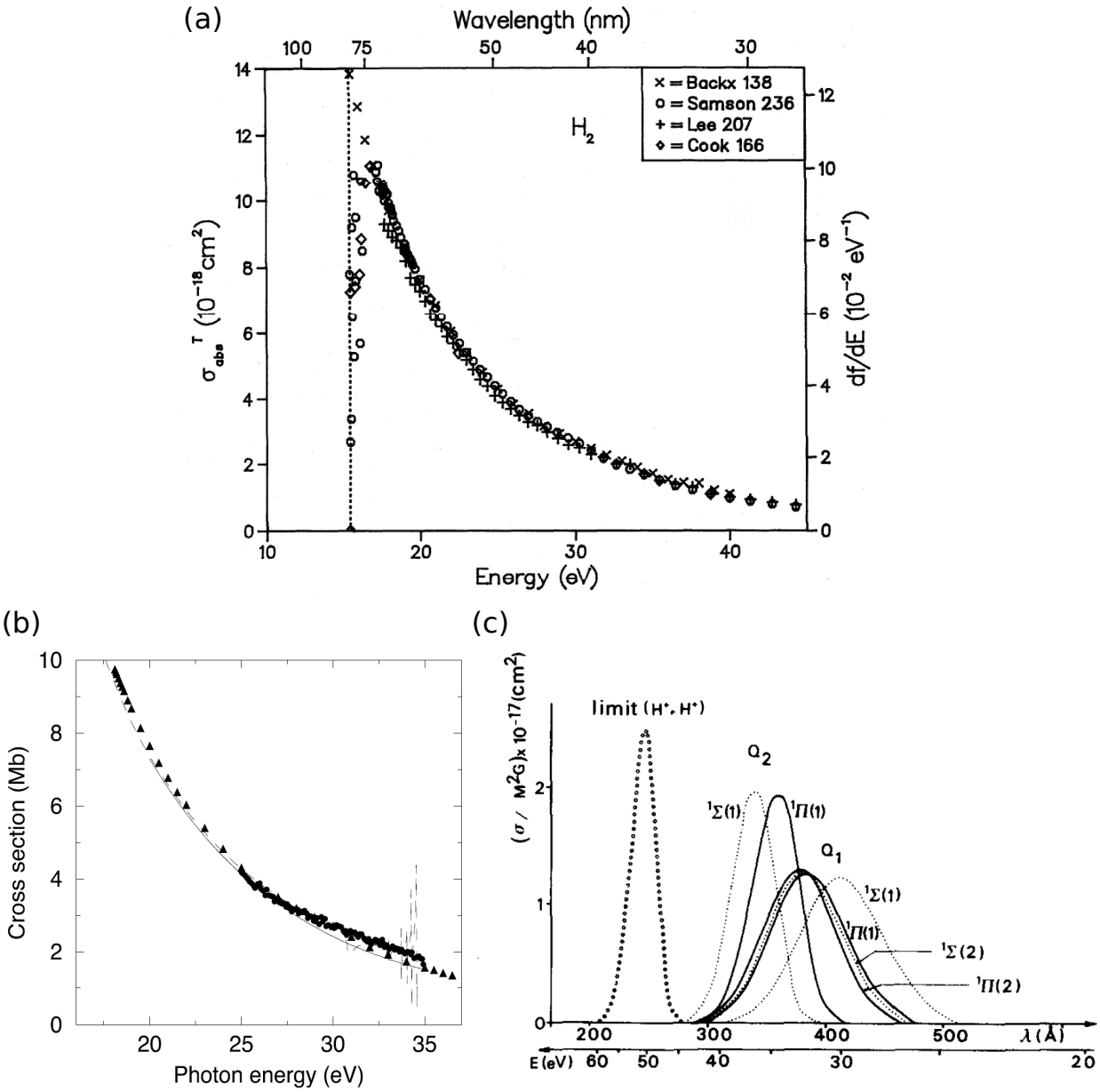

Figure 1.5: Absorption cross sections of H_2

(a) Synchrotron photoabsorption cross sections for H_2, taken from [18]. **(b)** Total photoionization absorption cross section of H_2. Triangles and dots are experimental data. Black and dashed curve are calculations. Plot taken from [19]. **(c)** Computed absorption cross sections for optically allowed doubly excited states in hydrogen. Graph reprinted from [20].

photon ionization to occur, very low pulse intensities, even individual photons are sufficient. The ionization amplitude, related to the ionization probability, is very well described in perturbation theory, including only the first term of the perturbation series. An overview of the time-dependent perturbation treatment of laser-atom interaction is found, for example, in [15].

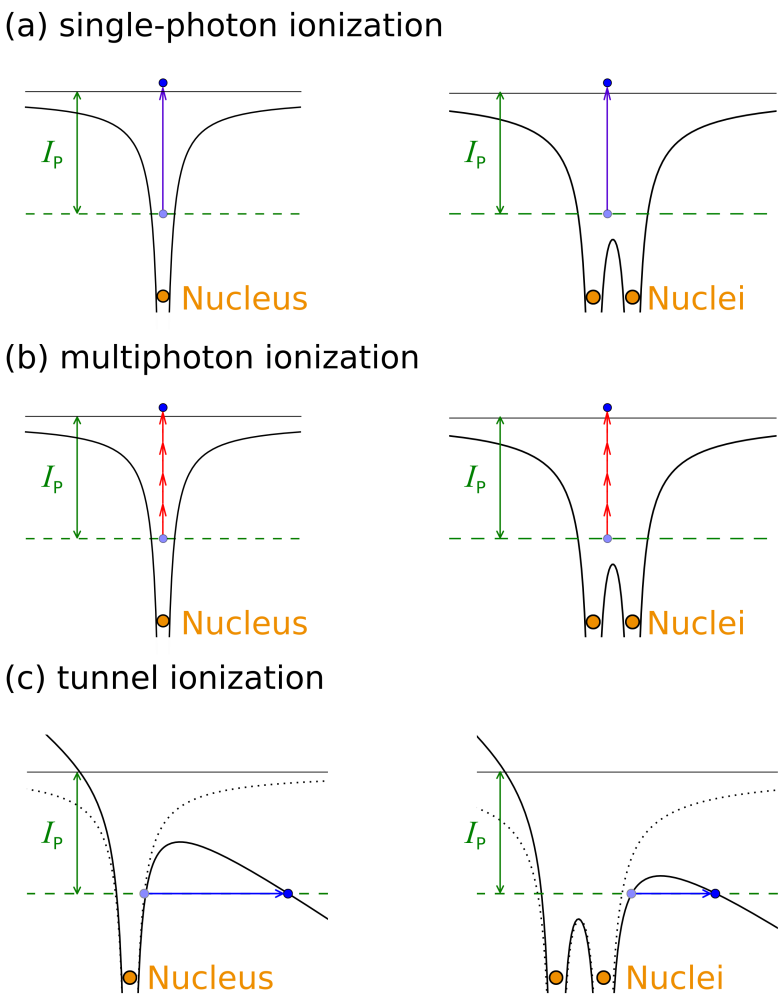

Figure 1.6: Illustration of the possible single-ionization processes
Sketches for the ionization cases in atoms (left) and molecules (right). **(a)** The special single-photon case. For it to occur, interaction with a photon with energy $\hbar\omega > I_P$ is required (purple arrow). **(b)** Multiphoton ionization. To overcome the ionization potential barrier, many photons with low energies are absorbed (red arrows). **(c)** Tunnel ionization, where the strong laser field lowers the potential and an electron can tunnel outside the binding region of the potential (blue arrow).

Multiphoton Ionization

If however higher terms in the perturbation series expansion for the ionization amplitude are considered, the ongoing processes are easily interpreted in terms of multiphoton transitions. Such transitions play an important role, when single-photon ionization is forbidden due to low photon energies.

Tunnel Ionization

The second ionization mechanism, which can occur, when single-photon ionization cannot take place, is tunnel ionization. This time, however, it cannot be treated in the perturbation

approach, since tunneling occurs only if the interacting laser field is of strengths comparable to the binding potential strengths, such that atomic and molecular potentials are strongly distorted, as illustrated in Fig. 1.6 (c). Tunneling ionization is treated in the ADK-theory approach, named after M. V. Ammosov, N. B. Delone and V. P. Krainov, who historically first introduced it for ionization of atoms [21]. It was later extended by C. D. Lin, so that ADK-theory could be applied also to laser-molecular interactions.

Whether perturbation theory or ADK-theory is more appropriate for the theoretical description of a particular problem, can be settled, calculating the corresponding Keldysh parameter [22]. This is an adiabaticity parameter, with the help of which the two ionization regimes can be separated. It depends on the ionized target species, the laser intensity and the carrier frequency:

$$\gamma = \omega_0 \sqrt{\frac{2I_\mathrm{P}}{I}}, \tag{1.14}$$

where I_P is the ionization potential of the target system, ω_0 the photon energy in atomic units and I the laser intensity. For $\gamma \ll 1$ the ionization is best described by tunneling, whereas for $\gamma \gg 1$, or frequently even $\gamma \tilde{>} 1$, multiphoton interaction should be considered.

The Keldysh parameter is frequently expressed in terms of the ponderomotive potential, given by

$$U_\mathrm{P} = \frac{I}{4\omega_0^2}, \tag{1.15}$$

which is defined as the averaged kinetic energy of an electron in a periodic laser field. With this,

$$\gamma = \sqrt{\frac{I_\mathrm{P}}{2U_\mathrm{P}}}. \tag{1.16}$$

Just calculating γ, the appropriate theoretical approach can be adopted. In reality however, the laser parameters are mostly such that $\gamma \approx 1$, so that no clear classification is possible. Nevertheless, as a general rule of thumb one should recall:

- $\gamma \ll 1$, when the laser intensity becomes very large and the photon energy very small, so that the light field can be described classically in the limit of infinitely many photons. A special case of tunneling ionization is the over-the-barrier ionization, when the intensity of the laser field is so high, that the Coulomb barrier is completely suppressed and the electron is set free in the laser field.

- $\gamma \gg 1$ is the case for relatively low intensities (compared to the tunneling case) and small photon energies, compared to the ionization potential I_P.

A schematic overview of all here presented single-ionization processes is given in Fig. 1.6, where the atomic and molecular picture are compared.

1.3.2 Double-Ionization Processes

Apart for single-ionization, multiple ionization of atoms and molecules can also happen as a result of light-matter interaction. Since only atoms and molecules with two electrons are considered in this work, double ionization is addressed rather than multiple ionization. Here, it should be noted that multiple ionization in general provides the possibility to study correlations between electrons. The basic idea is that in the absence of correlations, the second (and eventually further) ionization would happen independently of the first ionization, which gives rise to a sequential double (or multiple) ionization. If on the other hand correlations are present, the ionization of a single electron could possibly lead to further ionization of the ion. The two electrons are then liberated at the same time. This process is called non-sequential double ionization.

1.3.3 Autoionization

Another ionization process, arising due to correlation effects between electrons, is the process of autoionization. It occurs in excited states of atoms and molecules, found above the first ionization threshold. Such states are energetically degenerate with the continuum. Since in He and H_2, all doubly excited states are located above the first ionization threshold, doubly excited states can be thought of as of a synonym for autoionizing states. For autoionization to take place, one of the electrons of the doubly excited autoionizing state can radiationlessly move to an energetically lower lying electronic shell. The released energy is then transferred to the other electron, which will thus have energy high enough to ionize spontaneously without any laser interaction.

Autoionization can of course also occur during laser interaction. It taking place only depends on the requirement of previous population of autoionizing states. Since the product of autoionization is an ion and a free electron, which is basically also the result of a regular ionization process, as those discussed in Section 1.3.1, this spontaneous process leads to quantum interference effects of different ionization pathways.

In the case of helium, there are two possibilities:

$$\mathrm{He} + \gamma \rightarrow \begin{cases} \mathrm{He}^+ + e^- & \text{single ionization} \\ \mathrm{He}^{**} \rightarrow \mathrm{He}^+ + e^- & \text{autoionization} \end{cases} \tag{1.17}$$

In the here chosen notation He^{**} denotes a doubly excited state. The quantum mechanical interference of the two ionization channels in helium is very well studied in the context of the Fano formalism of configuration interaction [1, 2, 3, 4].

Autoionization of doubly excited states of H_2 has been also a subject of thorough investigations, mostly theoretically but also experimentally. The competing processes in this case however are not only two, since at least neutral molecular dissociation also comes into play. Thus considering the H_2 molecule to absorb energy higher than the first ionization potential,

the following processes occur:

$$\mathrm{H_2} + \gamma \rightarrow \begin{cases} \mathrm{H_2^+} + e^- & \text{single ionization} \\ \mathrm{H_2^{**}} \rightarrow \begin{cases} \mathrm{H_2^+} + e^- & \text{autoionization} \\ \mathrm{H} + \mathrm{H} & \text{neutral dissociation} \\ \ldots & \text{other processes.} \end{cases} \end{cases} \tag{1.18}$$

The $\mathrm{H_2^{**}}$ states are frequently referred as superexcited molecular states. Restricting ourselves to electronic states, in the notation of section 1.1.2, the superexcited states are the doubly excited Q_n resonances. The most important feature in their dynamics is the competition between the autoionization and neutral dissociation, and on top of this the interference with the direct single-ionization process. Distinguishing the autoionization pathway from the entirety of all other possible ionization pathways, was the driving motivation of the investigations in molecular hydrogen, presented in Chapter 4.

1.4 The Principles of High-Order Harmonic Generation and Carrier-Envelope Phase Stabilization

Before dedicating ourselves to the carried out experimental and theoretical work in this thesis, the working principle of two experimental techniques, high-order harmonic generation (HHG) and stabilization of the carrier-envelope phase (CEP) of ultrashort laser pulses, are discussed. Both of them are crucial for the atomic and molecular studies, presented in Chapter 3 and 4.

1.4.1 High-Order Harmonic Generation and Production of Attosecond Pulses

As it was revealed in Section 1.2.2, one of the laser pulses, implemented in the pump–probe or excitation–interaction scheme for detection of transient absorption signals, is usually in the extreme ultraviolet (XUV) spectral region. This is required for accessing the electronic dynamics in excited electronic states of atoms and molecules. Furthermore, the XUV radiation should be short enough to resolve the electronic motion on its natural attosecond timescale. Such an XUV pulse could be generated by the process of high-order harmonic generation in, for example, nobel gas targets[1]. A short overview of the HHG process is given in this section, following the outline of chapter 7 in [25]. Figures 1.7 and 1.8 serve hereby as an illustration.

The generation of high harmonics of intense NIR pulses typically begins with some tens of fs long laser pulses centered at around 800 nm wavelength (as those produced by the laser

[1] nobel gases: He, Ne, Ar, Kr, Xe

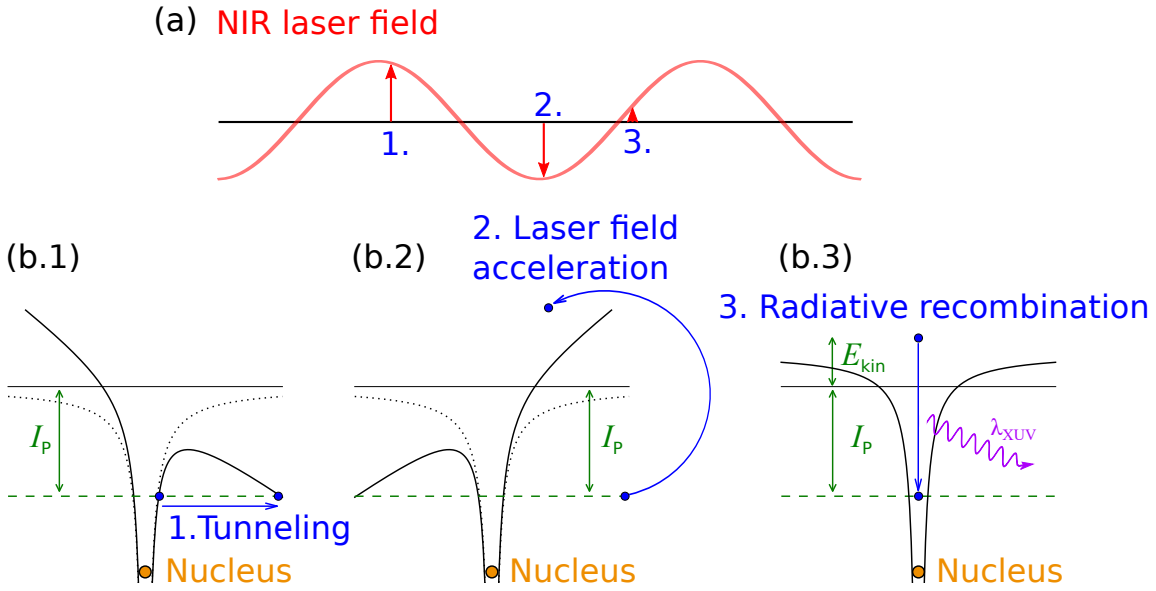

Figure 1.7: The three-step model of high-order harmonics generation.
Sketch of the 3-step model, showing the main steps in the process of high-order harmonics generation: tunneling, acceleration and radiative recombination, as described by [23, 24]. The points in time during the oscillation of the NIR laser field (red curve), where the three steps take place are depicted. Note that the whole process repeats every half cycle, so that bursts of XUV radiation appear periodically once in an NIR laser cycle.

system described in the chapter about the laser system, Cha. 2.1) focused into a gas medium at intensities of at least 10^{14} W/cm^2. The peak field strength of such laser pulses approaches the order of magnitude of the binding potential in the target, thus being able to considerably deform the atomic potential, allowing a part of the valence-electron wave function to tunnel into the continuum, which in a semi-classical description can be understood as if a bound electron is pulled out of an atom by lowering the potential barrier to the continuum. The free electron is then accelerated away from the atom core, gaining energy in the strong laser electric field. When the laser field direction reverses, the electron is being decelerated and afterwards driven back towards the atom. The returning electron, with energy higher than its initial energy after the tunneling, can radiatively recombine with the atom, releasing energy equal to the gained kinetic energy plus the reversed ionization potential, i.e.

$$\hbar\omega_{\mathrm{HHG}} = E_{\mathrm{kin}} + I_{\mathrm{P}}, \tag{1.19}$$

where I_{P} of the noble gases is given in Table 1.3. It should be mentioned that E_{kin} reaches a maximum, depending on the laser field strength, so that a cut-off in the frequency spectrum of the XUV radiation field appears:

$$\hbar\omega_{\text{cut-off}} = 3.17U_{\mathrm{P}} + I_{\mathrm{P}}, \tag{1.20}$$

Species	Ionization potential, I_p	
	(eV)	(a.u.)
helium	24.59	0.9036
neon	21.56	0.7925
argon	15.76	0.5792
krypton	14.00	0.5145
xenon	12.13	0.4458

Table 1.3: Ionization potential I_p for neutral rare gas atoms.
The I_p of all noble gases, except for radon, are listed in the table. The values in eV and a.u. are calculated according to the data in [10].

with U_P being the ponderomotive potential, defined in Section 1.3.

In the process of high-order harmonics generation, the first tunneling step takes place usually at around the maximum of the laser field, followed by the quasi-free propagation in the next three-quarters of a cycle until the recombination at nearly zero electric field strength. Those three steps of the HHG process were first described by P. Corkum [23] and are known as the tree-step model of HHG, which is sketched in Figure 1.7. The three steps repeat every half a cycle, so that the HHG process occurs twice per cycle but since the sign of the electric field strength flips between successive radiation bursts, the harmonics spectrum consist of only the odd harmonics of the fundamental laser frequency. With a long incident pulse with many cycles, the emitted radiation appears as a comb of intense isolated harmonics of the driving laser, corresponding to an attosecond pulse train. To generate single attosecond XUV pulses few-cycle incident NIR pulses (only a few fs long) should be used. The generation of such short and intense laser pulses is illustrated in Fig. 1.8.

1.4.2 Carrier-Envelope Phase of NIR Pulses

The previous section already touched upon the fact that the HHG process is sensitive to the driving NIR field and therefore also to the CEP of the NIR laser pulse . Adjusting the right CEP of the NIR field is crucial for obtaining isolated attosecond pulses in the XUV spectral range. Therefore, the fundamental principles of CEP-stabilization, with emphasis on their implementation in our experimental setup, are discussed here. Prior to this, however, we shortly turn our attention towards the description of short pulses, coming out of mode-locked oscillators, illustrated in Figure 1.9. The output of such an oscillator is a train of short pulses, separated by the cavity round-trip time. Each pulse in the pulse train can be thought of as of a carrier oscillation under a pulse envelope. The phase, accumulated by the carrier wave between its own and the envelope's maximum, is known as the carrier-envelope phase, ϕ_{CEP}. In the frequency domain, a pulse train corresponds to a frequency comb, consisting of frequencies, spaced exactly by the

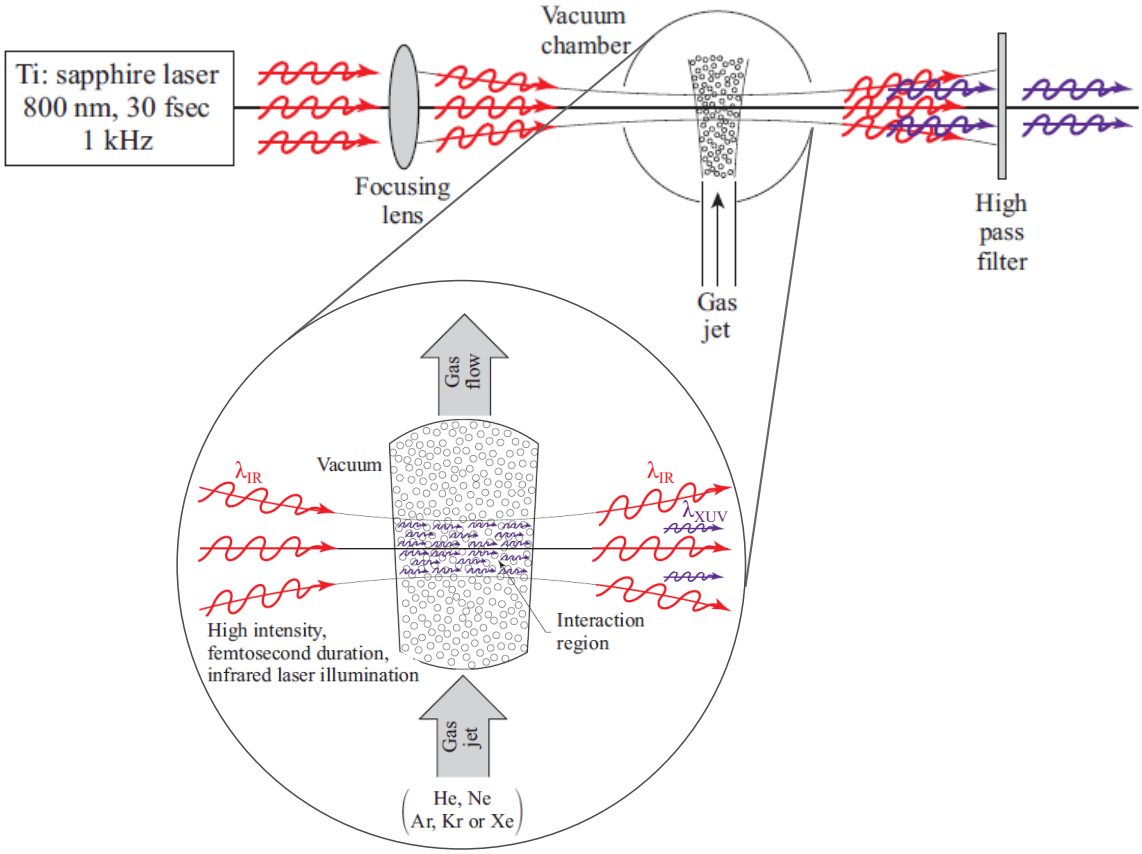

Figure 1.8: Schematic overview of high-order harmonic generation
The sketch illustrates the principle experimental technique for creating attosecond pulses through generation of high harmonics of an intense NIR field, focused to intensity on the order of $10^{14} - 10^{15}$ W/cm^2 onto a gas jet of noble atoms. The single atom response from the individual atoms coherently adds up under the right phase-matching conditions and an XUV pulse train is generated, as shown in the enlarged section. Filtering out the incident laser light and letting only the higher energy photons from the XUV region pass through a high pass filter, usually a metal filter out of Al or Zr, a train of attosecond pulses is generated. If the incoming NIR pulse is short, of the order of $4 - 7$ fs, and has the right CEP, an isolated attosecond pulse can be created. Figure adapted from [25].

cavity-length dependent repetition rate. The optical frequency of each comb line is given by

$$f_n = n f_{\text{rep}} + f_{\text{CEO}}, n \in \mathbb{N}, \tag{1.21}$$

where f_{CEO} is known as the carrier-envelope offset (CEO) frequency, defined as in Fig. 1.9. The change of the CEP from one pulse to the next is linked to f_{CEO} and f_{rep} via

$$\Delta\phi_{\text{CEP}} = 2\pi \frac{f_{\text{CEO}}}{f_{\text{rep}}}. \tag{1.22}$$

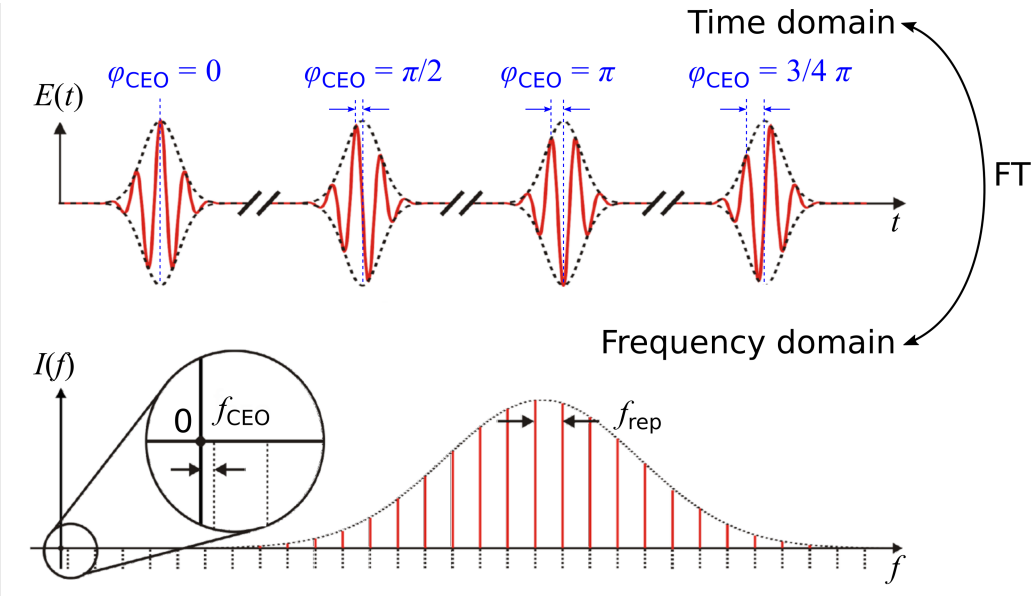

Figure 1.9: Time and frequency domain picture of the output of a mode-locked laser Example of a CEP stabelized pulse train, where $f_{\mathrm{CEO}} = f_{\mathrm{rep}}/4$, so that every fourth pulse is identical, adapted from [26].

Letting a mode-locked oscillator run, without any stabilization, f_{CEO} jitters arbitrarily as a function of time, taking values between zero and f_{rep}. According to eq. (1.22), the CEP then also changes randomly from shot to shot. Setting

$$f_{\mathrm{CEO}} = f_{\mathrm{rep}}/N \tag{1.23}$$

yields a pulse train where every N-th pulse has identical CEP. Picking out only one of those pulses for amplification, only pulses of equal CEP enter in the laser amplifier. Setting alternatively f_{CEO} to be zero, yields a pulse train, where each and every pulse has the same CEP and therefore all of those are identical. This scenario is implemented in the laser system, used for the experiments in this thesis, Fig. 2.1.

Measuring Changes in CEP

To be able to stabilize the CEP, as required for the experiments in chapter 4, a technique to measure the momentary carrier-envelope phase is required. An indirect possibility for this is given through a direct determination of the frequency offset f_{CEO}. The methods of choice here are based on nonlinearly mixing frequencies of an octave-spanning frequency comb, either by second harmonic generation (SHG) or by difference frequency generation (DFG), for example. The basic idea, independently of the preferred approach, is that frequency components from one end of the spectrum are projected onto the other one, where interference with the fundamental frequency is observed. The beating in time, resulting from the interference process, has a beating frequency f_{CEO}. The described measuring scheme is called self-referencing and is

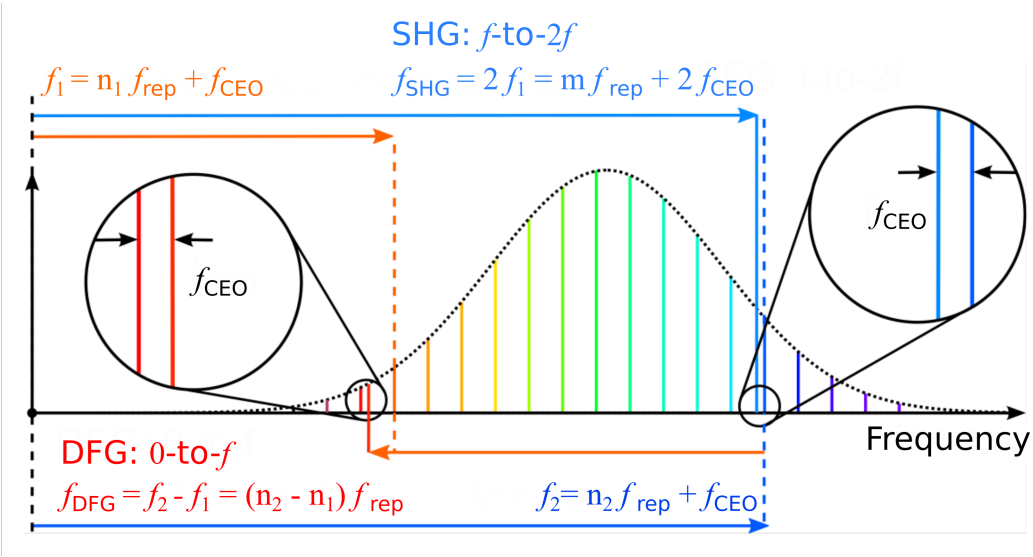

Figure 1.10: Self-referencing schemes for measuring changes in CEP
Using two lines of the fundamental comb (f_1 and f_2), separated by more than an octave, the CEO frequency can be determined by both the SHG (upper part) and DFG scheme (lower part) In the former case, the interference takes place on the high-frequency edge of the spectrum, whereas in the latter, the overlap happens on the low-frequency edge. Figure adapted from [26].

commonly realized in an f-to-$2f$ or in an f-to-$0f$ interferometer [26, 27]. A sketch of both referred measuring techniques is shown in Fig. 1.10. In the CEP4-module, installed after the oscillator in our laser system, the CEO frequency is detected using a modified scheme, based on difference frequency generation [26]. An f-to-$2f$ interferometer is installed after the laser amplifier.

Feed-Forward CEP Stabilization

Measuring the CEO frequency and therefore gaining information about the carrier-envelope phase of the laser pulses, is only one side of the coin, when aiming to stabilize the CEP. The other side is actual CEP pulse stabilization. Usually, commercially available CEP-stable light sources are based on the feed-back stabilization, relying on a phase-locked loop to lock the CEO to a fixed value, as depicted in eq. (1.23). The feed-back stabilization however has some drawbacks, [26, 28]. Two examples are: First, the feed-back stabilization requires $f_{CEO} \neq 0$, making it impossible to achieve a train of identical laser pulses. Second, failure of the lock electronics is problematic for experiments where long integration times without a change in the wave form of the driving pulse is needed. To overcome the disadvantages of the regular feed-back stabilization, in our laser system a feed-forward CEP stabilization scheme is implemented. The technique was first suggested by the group of Günter Steinmeyer and later patented by Femtolasers [29]. The traditional feed-back stabilization relies on manipulating the oscillator, to change the waveform by effects in the time domain, thus influencing all comb lines at once.

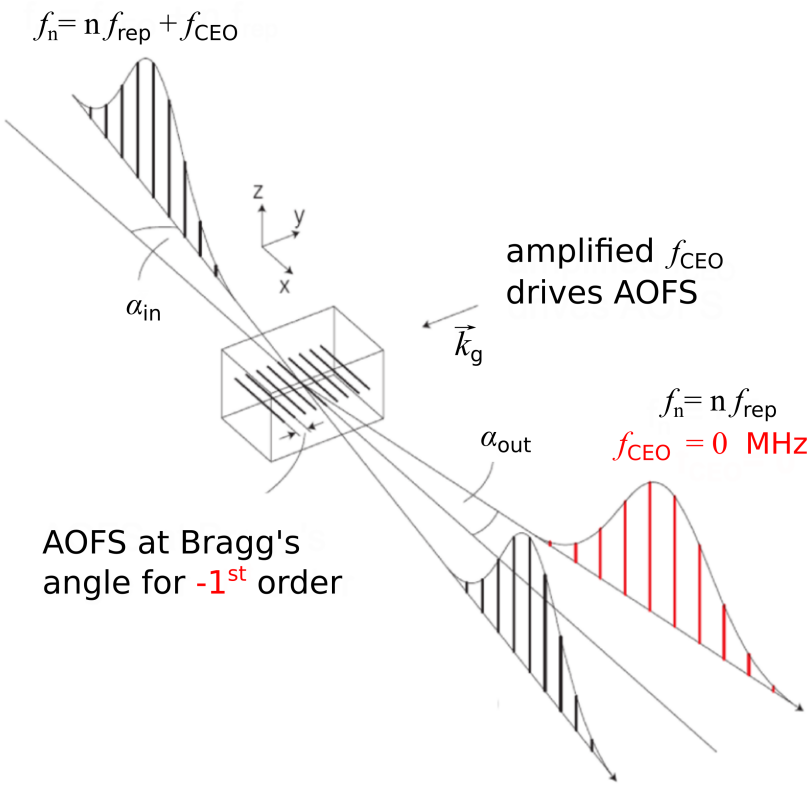

Figure 1.11: The feed-forward referencing scheme
The oscillator output passes through an AOFS, where the amplified CEO frequency is used as a driving signal. All lines of the output spectrum are reduced in frequency by the common offset f_{CEO}. The -1^{st} order diffracted beam therefore has $f_{CEO} = 0$ MHz, which is equivalent to a pulse train with constant CEP. Figure adapted from [26].

Instead of doing this however, one could also reduce the frequency of every comb line by the offset f_{CEO}, thus yielding $f_{CEO} = 0$ MHz as a result, which then allows for having a pulse train of identical pulses. In the feed-forward scheme, the shift of all comb lines is achieved by interaction with an acoustic wave within an acousto-optical frequency shifter (AOFS), as shown in Fig. 1.11. This is the working principle of the CEP-stabilization in our laser setup: measuring the CEO and then subtracting f_{CEO} from every single comb line in an AOFS crystal.

Overall CEP Stability of the Laser Setup

After the oscillator and the AOFS stabilization, the laser pulses enter an amplifier stage. After the amplification, longterm changes of the CEP are detected in an f-to-$2f$-interferometer, stabilizing the output pulses actively. For this, a computer-based control loop evaluates the CEP and generates a control signal to the AOFS to adjust the carrier-envelope phase. All in all, the output pulses are stabilized on the order of 300 to 400 mrad, which for 800 nm wave length resembles temporal CEP stability around 0.13 fs over the 2.67 fs cycle length. This corresponds to approximately 5% CEP stability of the NIR pulse, which is sufficient enough to generate relatively stable isolated attosecond pulses in the process of high-harmonics generation, described

in the previous section.

Chapter 2

Experimental Setup

The experimental setup used to carry out the experiments discussed in Chapter 3 and 4 of this thesis consists of two major parts: a femtosecond laser[1] system and a vacuum beamline for the spectroscopic pump–probe studies. A brief overview of the main components of both parts is given in the two sections of this chapter.

2.1 Generation and Characterization of Broadband NIR Pulses

Being already familiar with the quantum systems we want to study, He and H_2, and especially knowing that XUV radiation is needed to populate any excited states in these targets, a source which provides XUV radiation is necessary to look at linear absorption signals in helium and molecular hydrogen. There are different possibilities for obtaining the relevant photon energies [25], such as synchrotron light sources, free-electron lasers (FEL) or producing XUV pulses from NIR laser light with femtosecond pulse duration, as described in Sec. 1.4.1. However, when working at synchrotron and FEL facilities, only limited amount of beamtime is assigned to research groups, which proves impractical for regular needs, especially when exploring the technical limitations of an experimental setup. Therefore, the table-top high-harmonic generation technique is preferred for studies where low XUV pulse intensities are sufficient.

2.1.1 The Femtosecond Laser System

As an NIR light source for the generation of XUV light, we use a commercially available laser system, Femtopower^{TM} HR/HE CEP by Femtolasers GmbH, delivering CEP stabilized sub-20 fs laser pulses with energies up to 3 mJ at 3 kHz repetition rate. Note that this laser setup replaced a previously installed one with slightly different characteristics but with essentially the same working principle. The main parameters of both laser systems are compared

[1] Light Amplification by Stimulated Emission of Radiation

		old laser setup Femtopower Compact Pro CEP by Femtolasers GmbH		**new laser setup** Femtopower^{TM} HR/HE CEP by Femtolasers GmbH	
		before compression	after compression	before compression	after compression
Parameters	Repetition rate	4 kHz	4 kHz	3 kHz	3 kHz
	Pulse energy	0.7 mJ	0.3 mJ	3 mJ	1 mJ
	Pulse duration	sub-30 fs	6-7 fs	sub-20 fs	4-5 fs
	Central wavelength	790 nm	750 nm	786 nm	760 nm
	Spectrum bandwidth	50 nm	330-380 nm	68 nm	350-400 nm

Table 2.1: Laser setup parameters

The **old laser setup**, Femtopower Compact Pro CEP is the one used for recording the experimental data from Cha. 3. The experiments presented in Cha. 4 have been carried out using the **new laser setup**, Femtopower^{TM} HR/HE CEP.

in Table 2.1. The old laser setup, Femtopower Compact Pro CEP, was used to conduct the motivating experiments for the theoretical studies in Chapter 3, whereas the new laser system, the Femtopower^{TM} HR/HE CEP, was utilized for the experiments, discussed in Chapter 4. In the following, only the current laser setup, the Femtopower^{TM} HR/HE CEP, is presented. A description of the old one is found in [2, 30, 9, 31, 32].

A sketch of the laser components is shown in Fig. 2.1. An oscillator system delivers already CEP-stabilized lasers pulses shorter than 10 fs at 75 MHz repetition rates, with pulse energies around 1 nJ. These pulses are amplified in a chirped pulse amplification (CPA) stage in the multipass configuration. In the CPA, the pulses from the oscillator are stretched in time up to several picoseconds and are then propagated 10 times trough an amplifying gain medium, which is pumped using a high power Q-switched pump laser (DM-50, Photonics Industries). At the end, the amplified and chirped pulses are recompressed, which results in pulses with energy up to 3 mJ and duration below 20 fs but at the expense of a decreased repetition rate of 3 kHz. The gain medium in both the oscillator and the amplifier is a titanium-doped sapphire crystal (Ti:Al_2O_3 or Ti:Sa), able to amplify almost octave broad light, centred around 800 nm so that the output of the CPA system is also centred at $780 - 790$ nm. The output pulses are slightly longer than the input because of gain narrowing effects in the amplifier. The overall CEP stability[2] after the CPA process is on the order of 300 to 400 mrad, or approximately 5% CEP stability of the NIR pulse.

To broaden the spectrum further and at the end arrive at pulses only a few cycles long, a part of the laser beam (66 % of the intensity) is focused into a 1 m long hollow-core glass fibre with a core diameter almost 350 μm. It is filled with helium from the one side with a pressure of around 3 bar and differentially pumped on the entrance side down to $\approx$ 10 mbar. In the process of self-phase modulation (SFM), the laser spectrum is broadened coherently on both sides of

[2]For the CEP stabilization principles and their implementation in the laser setup, see Sec. 1.4.2.

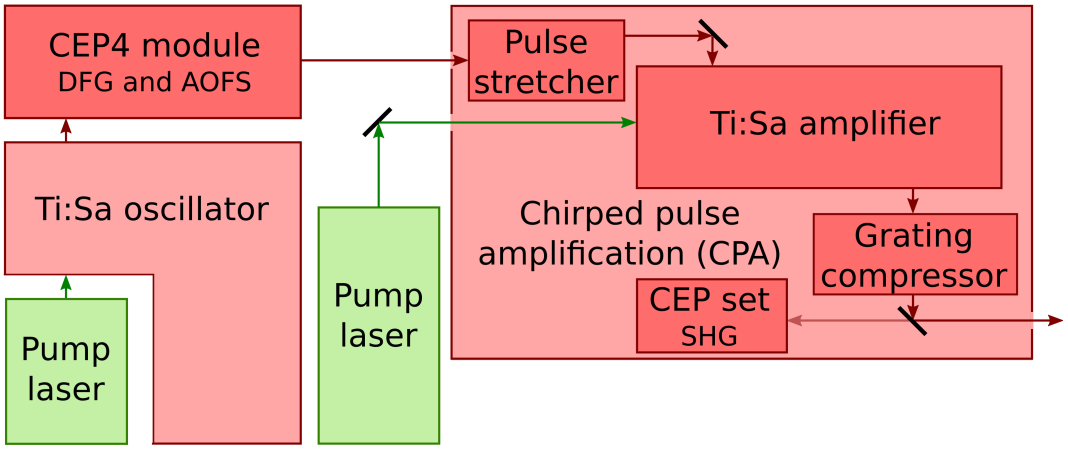

Figure 2.1: Block diagram of the femtosecond laser system
After the initial pulse production in the Ti:Sa oscillator, the pulses are CEP stabilized and subsequently amplified, using the CPA method. Both oscillator and amplifier are externally pumped (pump lasers).

the input pulse spectrum. Subsequently, the pulses are compressed again by a set of chirped mirrors, specially designed to reflect broad spectra (PC 70, UltraFast Inovations) [31]. With a five-pair set of chirped mirrors the pulse chirp is overcompensated. To finally obtain pulses with a duration of less than 5 fs, having pulse energies around 1 mJ, the correct dispersion compensation is achieved using a pair of movable glass wedges (fused silica with anti-reflective coating for wavelengths between 450 and 950 nm, 4° apex angle by Lens Optics). A sketch of the whole pulse compression procedure is found in Fig. 2.2.

2.1.2 Dispersion Scan

Before using the NIR pulses for experiments, they are characterized by means of the dispersion scan (D-Scan) technique implemented in our laser setup [31]. The D-Scan pulse characterization method allows for a complete reconstruction of the laser pulses (except for the CEP). Typical pulses used for the experiments in molecular hydrogen, Cha. 4, are characterized and shown in figure 4.17. Making use of the pair of glass wedges for dispersion fine-tuning, by recording a nonlinear spectral signature while changing the amount of glass in the beam path (and respectively changing the phase the glass adds to the pulses), an iterative algorithm extracts the spectral phase from the measured data. Recording in addition the fundamental spectrum, the temporal shape of the pulses is found via a Fourier transformation.

2.2 Experimental Beamline

The well characterized NIR laser pulses can now be sent into the attosecond spectroscopy beamline, which is shown as a 3D model in Fig. 2.3 (a) and as a schematic illustration in Fig.

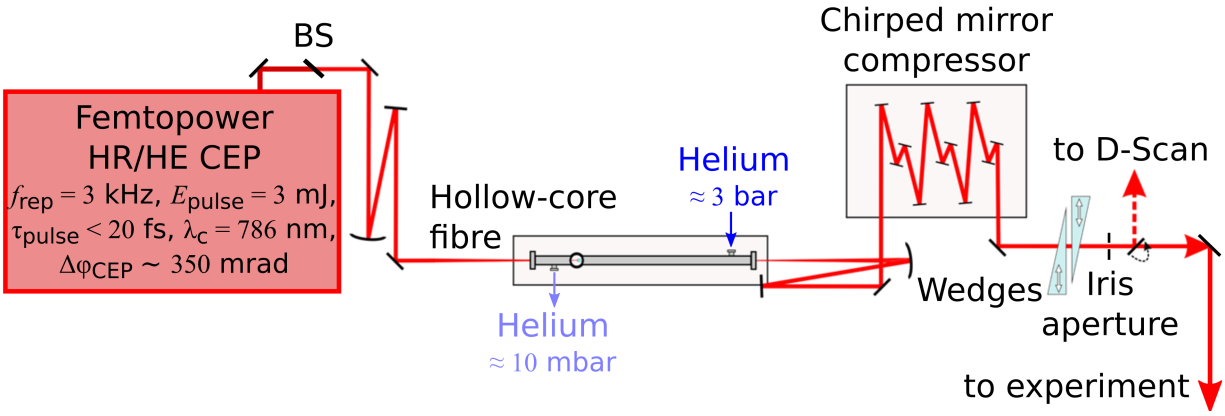

Figure 2.2: Setup for pulse compression down to pulse lengths < 5 fs
The laser light in the NIR spectral region, coming out of the Femtopower HR/HE CEP laser system, is attenuated with a beam splitter (BS), and is then focused into a hollow-core fibre, filled with differentially pumped helium. The spectrally broadened light is further compressed in a chirped mirror setup. A pair of wedges fine-tunes the right dispersion of the laser pulse. An iris aperture is added in the beam path to spatially filter the laser beam mode. The laser pulses are diagnosed in a dispersion scan (D-Scan) setup, before they are coupled into the experimental setup. Figure adapted and reprinted with permission (M. Hartmann, personal communication, 6 November 2017).

2.3 (b). For a more detailed description of the beamline, please refer to [33, 2, 3, 30, 9, 32] since only the major parts are addressed in the following.

2.2.1 Generation of Attosecond Pulses

At the beamline entrance, the laser pulse energy reaches approximately 500 µJ. With the beam focused (f = 50 cm) down to ~ 60 µm spot size inside the first vacuum chamber, (a.1) in Fig. 2.3, peak intensities around 10^{14} – 10^{15} W/cm^2 are reached. A 2 mm inner diameter stainless-steel tube with machine-drilled 150 µm diameter holes for the laser beam to pass through, is placed in the focus of the NIR beam. The cell is filled with a noble gas, argon for the experiments presented in this thesis. Finely scanning the cell position along the propagation axis of the laser light, which will be referred as the z-axis, and tuning the wedges in front of the beamline for maximum conversion efficiency, XUV light bursts emerge out of the HHG generation region. For efficient generation of XUV light in argon, a backing pressure of around 70 mbar is applied to the gas cell, hereafter called HHG cell. For higher efficiency of the HHG process, even higher pressure could be used, which was unfortunately not possible in our setup because of technical limitations regarding the pumping of the HHG vacuum chamber to maintain the overall necessary pressure of 10^{-3} mbar. A typical spectrum of the XUV radiation in the region of interest for the experiments in H_2, between 28 and 50 eV, is depicted in Fig. 4.2 (b) in Cha. 4.

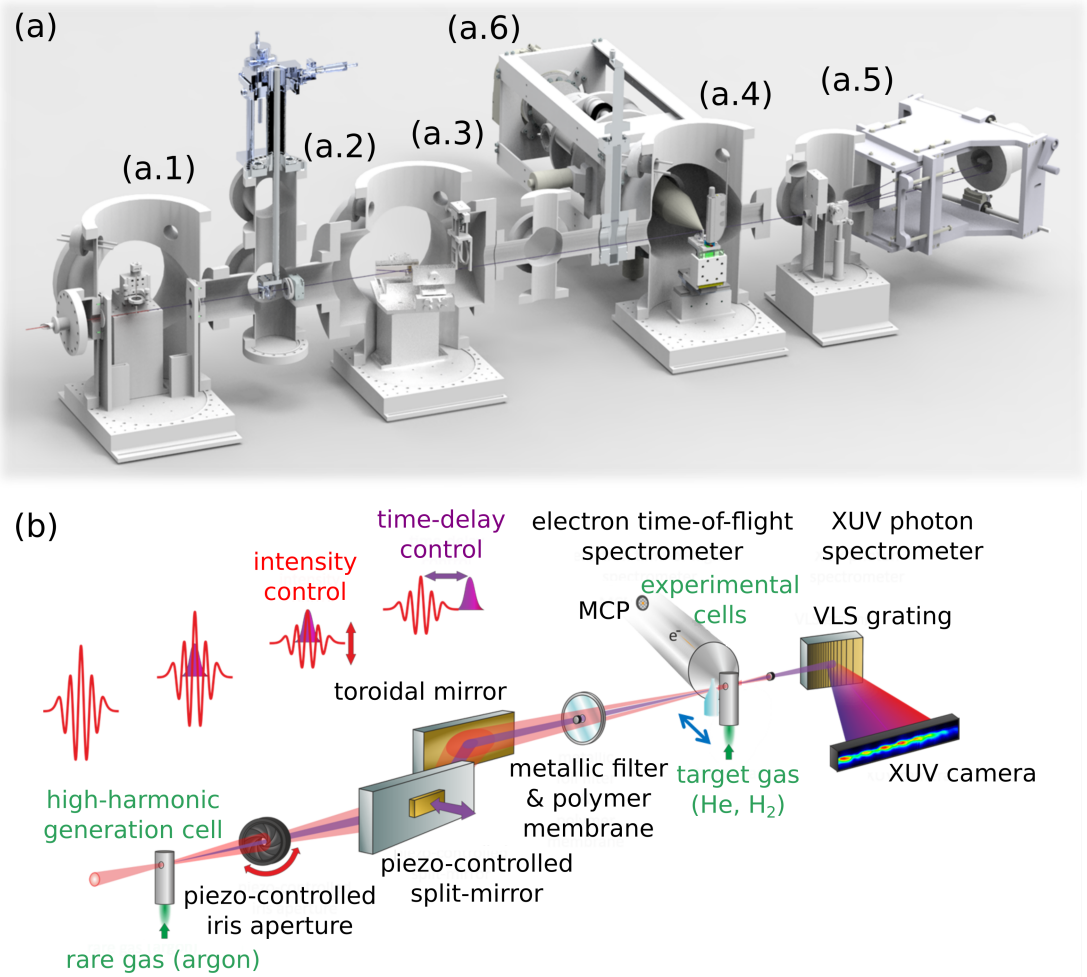

Figure 2.3: The experimental beamline for attosecond spectroscopy
(a) Overview of the experimental beamline, including the HHG **(a.1)**, iris **(a.2)**, mirror **(a.3)** and target chamber **(a.4)**. Light spectra are recorded by means of an XUV photon spectrometer **(a.5)**. Additionally, electrons can be detected in an electron time-of-flight spectrometer **(a.6)** [9, 31]. **(b)** Schematic illustration of the experimental setup, where all beamline parts, together with their function, are depicted. On the upper part of the sketch also the laser pulse configuration along the beampath is illustrated. The NIR intensity control is possible due to the piezo-controlled iris aperture, whereas the time-delay adjustment is controlled by the split-mirror setup. **(b)** Adapted and reprinted with permission (M. Hartmann, personal communication, 6 November 2017).

2.2.2 NIR-Intensity Control

After the generation of the the attosecond pulses in the HHG cell, both the NIR and XUV pulses travel spatially and temporally overlapped along the beamline. Before being separated, they pass through a motorized zero-aperture iris, concentrically placed in the combined beam path in vacuum chamber (a.2) of Fig. 2.3. The opening of the iris can be altered, which allows for intensity control of the NIR pulse without affecting the considerably less divergent XUV light beam. An absolute calibration of the NIR intensity in the spectroscopy target as a function

of the iris opening is challenging. It was previously done for the old laser setup [2, 3, 34] and is a subject of an ongoing master's thesis work [35].

2.2.3 Spatial and Temporal Separation of the XUV and NIR Pulses

In the next, mirror chamber, Fig. 2.3 (a.3), both the NIR and XUV pulses reach the split and delay unit, which is a fancy name for the interferometric mirror setup, consisting of two grazing-incidence mirrors: a pair of flat mirrors to separate the XUV and NIR light pulses in both position and time, and a toroidal mirror to subsequently refocus both spectral parts in the experimental target. The basic idea of the flat mirrors, where a smaller gold-coated mirror is located in the centre of a silver mirror [2], is that the XUV light has smaller divergence than the NIR beam, so that most of the XUV beam is reflected by the inner mirror, whereas the NIR light is reflected by both mirrors. Moving the inner mirror in or out in the plane perpendicular to the reflecting surface of the outer mirror, a time delay is introduced between the pulses, reflected by the inner mirror and the part of the NIR pulse, reflected mainly by the outer mirror. The delay stability of the split and delay unit is experimentally determined via analyzing the intensity-modulation of a HeNe laser, reflected by the split-mirror arrangement, as performed for the results presented in [2]. This characterization was newly done, after exchange of the inner gold-coated mirror, since its reflectivity has dropped down after years of operation. The determined stability value of 17 as, is close to the theoretical estimate for the typical 1 nm accuracy of the piezo-movement stage, which translates into 2 as stability under the grazing angle $\theta = 15°$ ([2] and references therein). Parallel to the stability determination, the temporal delay was also calibrated, so that

$$1\ \mu\text{m} \cong 1,701\ \text{fs} \tag{2.1}$$

was found.

To fully separate the attosecond XUV pulse from the femtosecond NIR laser field, the propagation path of both of them passes through a set of spectral filters. A new filter-unit assembly was designed in the scope of another master's thesis [35]. In the new design a 7.5 µm thin Kapton foil, transparent for visible light, but strongly absorbing XUV radiation, and a co-axially arranged 200 nm thin metalic (Al) filter, opaque for visible light but transmitting a considerable amount of the XUV light, were installed. A transmittance curve of the metalic filter is plotted in Fig. 2.4. Note, that this arrangement was used for the experiments, presented in Chapter 4, while the motivating experiment of Cha. 3 made use of a older filter with 2 µm-thin nitrocellulose membrane, details of which are presented in [3]. Both filter units, the new and the old one, introduce a group delay of the transmitted NIR light of a few fs and only a minor dispersion [2, 35].

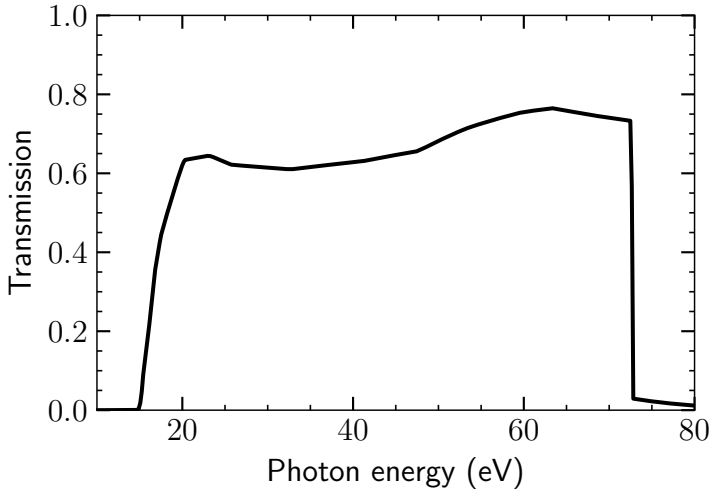

Figure 2.4: Transmission of a 200 nm thin metal filter of aluminium (Al)
Transmission of Al in the photon energy region between 10 and 80 eV. For energies smaller than 15 eV no light is transmitted. At around 72 eV a sharp cut-off in the transmission is present. Data taken from [36].

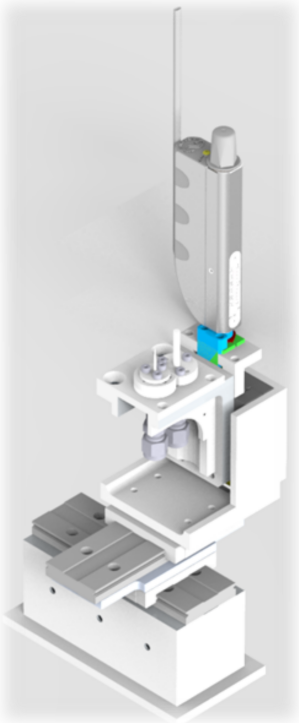

Figure 2.5: Design of the new target-cell stage system
The new design allows for fast movement of the cell in all three dimensions and its precise positioning in the overlapping focus of both the NIR and XUV beams.

2.2.4 Target Cell Positioning System

As it was previously mentioned, both the NIR laser and the XUV pulses are focused into the interaction region containing the target gas. For the experiments in this thesis, He and H_2

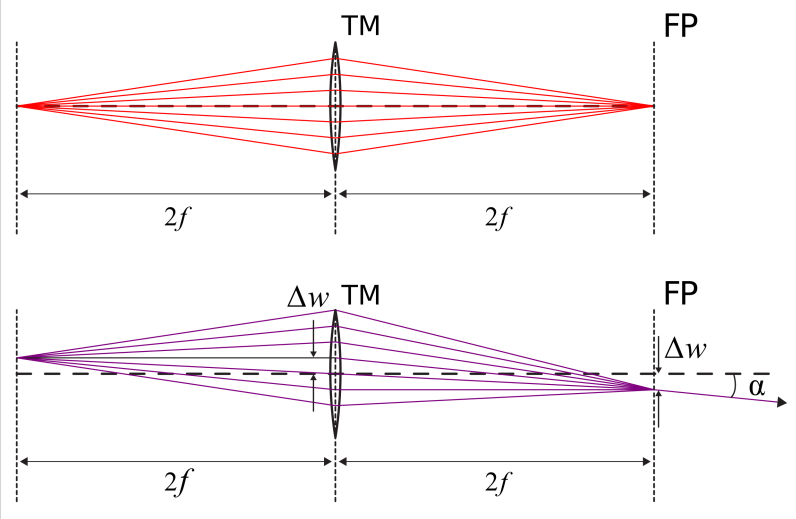

Figure 2.6: Walk-off induced by the grazing-incidence split-mirror setup
The toroidal mirror (TM) is illustrated as a lens with 1:1 imaging geometry. A parallel shift Δw is induced on the XUV light beam by the movement of the inner mirror, which corresponds to a displacement on the focal plane. The wave front is also tilted by the angle $\alpha = \arctan(\Delta w / f)$ with respect to no displacement, which corresponds to the NIR beam path (upper panel). f is the focal length, FP the focal plane. Figure adapted from [2].

flow under pressure inside a target cell, located in the target chamber, Fig. 2.3 (a.4). The target cell can be positioned precisely in the overlapping foci of the XUV and NIR beams in vacuum operation. The design of a new stage system, allowing for *in situ* adjustment of the cell, was developed in the scope of this thesis, Fig. 2.5. It closely follows the design of the stage systems installed in both the HHG and target chambers of another experiment of our research group [37, 38]. The advantage of the new design lies in the possibility to scan all tree dimensions, and therefore allowing to move the target cell in and out of the focus region to take reference spectra, since no simultaneous measurement of absorption and reference data is possible in the current experimental design. The possibility to move the target cell perpendicular to the laser beam propagation allowed to include a small movement of the cell in x-direction in the experimental procedure, called hereafter tracking of the target cell with respect to the time-delay piezo movement. The tracking is only a minor correction of the position of the target cell, as shown in the graph in Fig. 4.7. It is necessary because of a slight walk-off of the XUV focus with respect to the NIR focus. The walk-off arises when moving the piezo stage for the time delay and limits the accessible time-delay range to 50 fs because for large displacements the two foci will be spatially separated. The displacement of the XUV focus position is related to the mirror movement d in the following way:

$$\Delta w = d \frac{\sin(2\theta)}{\sin(\theta)}, \tag{2.2}$$

where $\theta = 15°$ is the grazing angle of incidence. Changing the time delay by $\Delta\tau = 1$ fs implies a transverse displacement $\Delta w = 1.13$ µm and a wave-front tilt $\alpha = 3.22$ µrad of the XUV beam with respect to the NIR beam, Fig. 2.6. This displacement corresponds to the correction, introduced by the cell position tracking where for $\Delta\tau = 1$ fs the cell position is changed by $\Delta w_{\text{cell}} = (1.0 \pm 0.1)$ µm. Therefore, it allows for keeping XUV light flux through the target cell on the approximately same value for the whole accessible time-delay range. For more details on the cell tracking operation mode and especially the determination of the tracking-shift value, see Sec. 4.2.4.

2.2.5 Flat-Field XUV Spectrometer

After interacting with the target gas, the XUV light is spectrally resolved in a flat-field spectrograph, also operated under grazing incidence. The most important parts of this device, shown in Fig. 2.3 (a.5), are the reflection grating with variable line spacing (VLS) and a CCD camera, recording the spectrally resolved measurement signal on the flat spectral plane of the camera chip. The position of the CCD camera can be adjusted along the imaging plane so that a wide XUV spectral range is resolved. Looking at the grating equation, which is approximately applicable to a curved grating geometry,

$$m\lambda = d\left(\sin\alpha - \frac{1}{\sqrt{\left(\frac{x}{a}\right)^2 + 1}}\right) \tag{2.3}$$

with m being the diffraction order, λ the wavelength of the light, d the grating constant and all other quantities as shown in Fig. 2.7, it is evident that at one and the same position of the imaging plane not only first order, but also second or even third order light of wavelength $\lambda/2$ und $\lambda/3$, respectively, can be recorded simultaneously. This feature is extensively used in both experiments presented in this thesis.

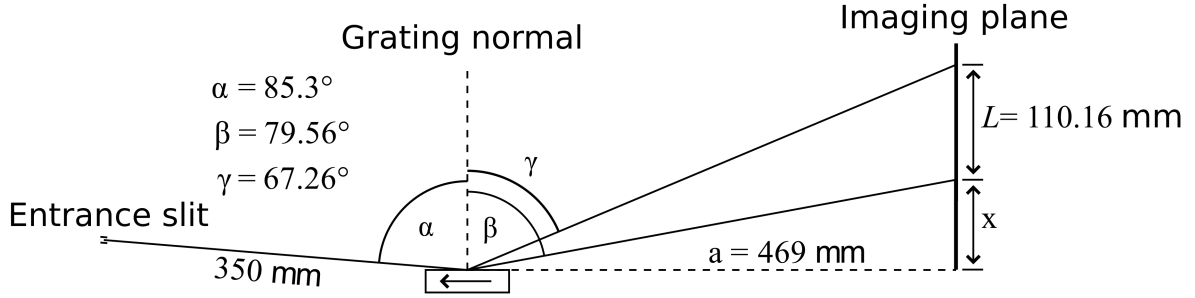

Figure 2.7: Imaging geometry of the VLS grating

The VLS grating spectrally disperses the light, coming through the entrance slit onto the flat imaging plane across the distance L. The angles α, β, γ denote the angle of incidence, the maximal and the minimal angle of diffraction in the first order, respectively. Figure adapted from [2].

Chapter 3

Laser-Intensity Dependent Ionization Processes in the Helium Atom

An exemplary system to study multi-electron effects in their great complexity is the helium atom being the smallest atomic system with more than one electrons ant therefore exhibiting electron correlation effects. The ionization dynamics of helium is considered in the first part of this master's thesis. In Section 3.1, an experiment exploring the onset of two-electron effects in strong-field ionization of singly and doubly excited states, SES and DES, is discussed. The observed difference in the ionization dynamics of the considered atomic states motivated a detailed theoretical study of the occurring ionization mechanisms in the helium atom, for which a one-dimensional two-electron model of the helium atom, Section 3.2, was employed. The simulation results, presented in Section 3.3, aim to explain the experimental observations.

3.1 Motivating Experiment

The method of attosecond transient absorption spectroscopy, as described in Section 1.2.2 with the experimental implementation presented in Chapter 2, was employed to measure the perturbed polarization decay of gas-phase helium. For the sake of clarity, a brief sketch of the experiment is presented in Fig. 3.1. First, a broadband XUV pulse coherently populates bound states with one and two excited electrons simultaneously at a time, defined as the zero position time. After a time delay τ the system's evolution is perturbed by a few-femtosecond NIR laser pulse with tunable intensity. Adjusting the time delay between the pulses as well as the intensity of the NIR pulse, it is possible to alter the perturbation of the system, induced by the NIR pulse, from the weak to the strong coupling regime and observe strong field ionization effects for the highest intensities.

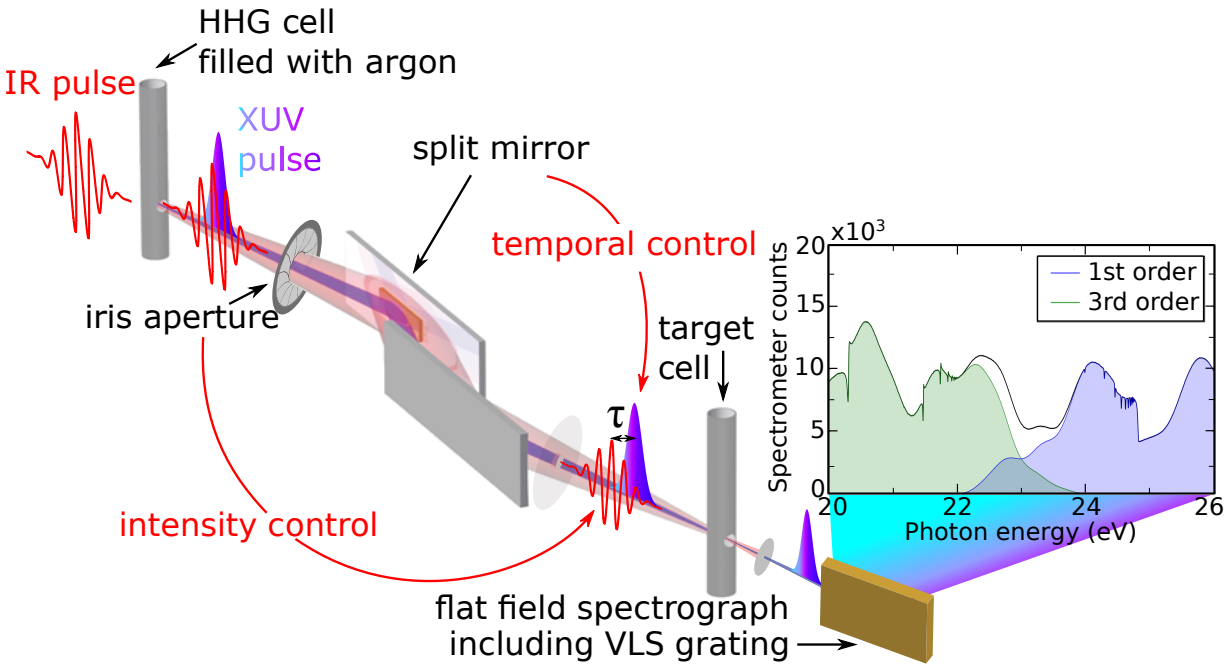

Figure 3.1: Experimental scheme

Illustration of the experimental setup for simultaneous spectroscopic measurement of the 1snp and $sp_{2,n+}$ series in Helium. In the shown spectrum for zero NIR intensity the different colors indicate the spectrometer diffraction order. The first order XUV spectrum (blue) shows the singly excited 1snp series, whereas the third order light contains the doubly excited states of the $sp_{2,n+}$ series.

3.1.1 Measurement

In the experiment discussed here, it is of key importance to directly compare the response of the considered SES and DES. This is the reason why the dynamics of the states should be recorded perfectly simultaneously. To manage simultaneous detection, we make use of the different diffraction orders of the spectrometer grating and are therefore able to take a single spectroscopic image with both the absorption lines of the singly excited and doubly excited states of helium. In the aforementioned way we overcome the challenge to record absorption spectra with high resolution over the relevant spectral range from 21 eV to 65 eV, where the entire $sp_{2,n+}$ series as well as the 1snp series with $n > 2$ are excited. Population of the 1s2p-state is avoided, so that no resonant coupling effects between the doubly excited states and the 1snp resonances with $n > 2$ could occur. In Fig. 3.1 the 1snp series up to the ionization threshold at 24 eV and the $sp_{2,n+}$ series of the doubly exited states starting at 60.5 eV in third-order diffraction, which translates to a first-order energy of around 20 eV, are shown in the unperturbed case. It should be noted that in the current experimental setup there is no other way, apart from simultaneous detection as shown in Fig. 3.1, to ensure that the results for both sets of states were obtained under the exact same conditions. This is especially important for the NIR intensity, which is the main scanning parameter in the presented experiment, and since the *in-situ* measurement of the NIR laser field is not possible in the existent setup.

3.1.2 Experimental Results

With the presented measurement scheme, scans of the time-delay τ between XUV and NIR pulse were recorded for an intensity range between 0.1 and 9.8 TW/cm^2. Figure 3.2 (a) shows the intensity scan of the time-average over one laser cycle, centered at a time-delay $\tau = 5$ fs, so that the XUV pulse comes first and the NIR second. Lineouts of this scan at NIR intensities $0.1, 4.0, 7.0$ and 9.5 TW/cm^2 are presented in Fig. 3.2 (b.1) to (b.4) respectively. The effects observed at lower intensities, like the Autler-Townes splitting of the 2s2p-state and the modifications of the line shape, caused by a change of the Fano q-parameter due to the strong NIR pulse, have been studied in previous work of this group [2, 3, 39, 34, 4]. Looking, however, at the highest NIR intensity data, it appears that the behaviour of the doubly excited states differs from the behaviour of the bound states with only one excited electron. For intensities above 9.0 TW/cm^2 all DES fully ionize, which is encoded in the vanishing of the spectral lines. The resonance lines of the singly excited states, on the other hand, are still clearly visible.

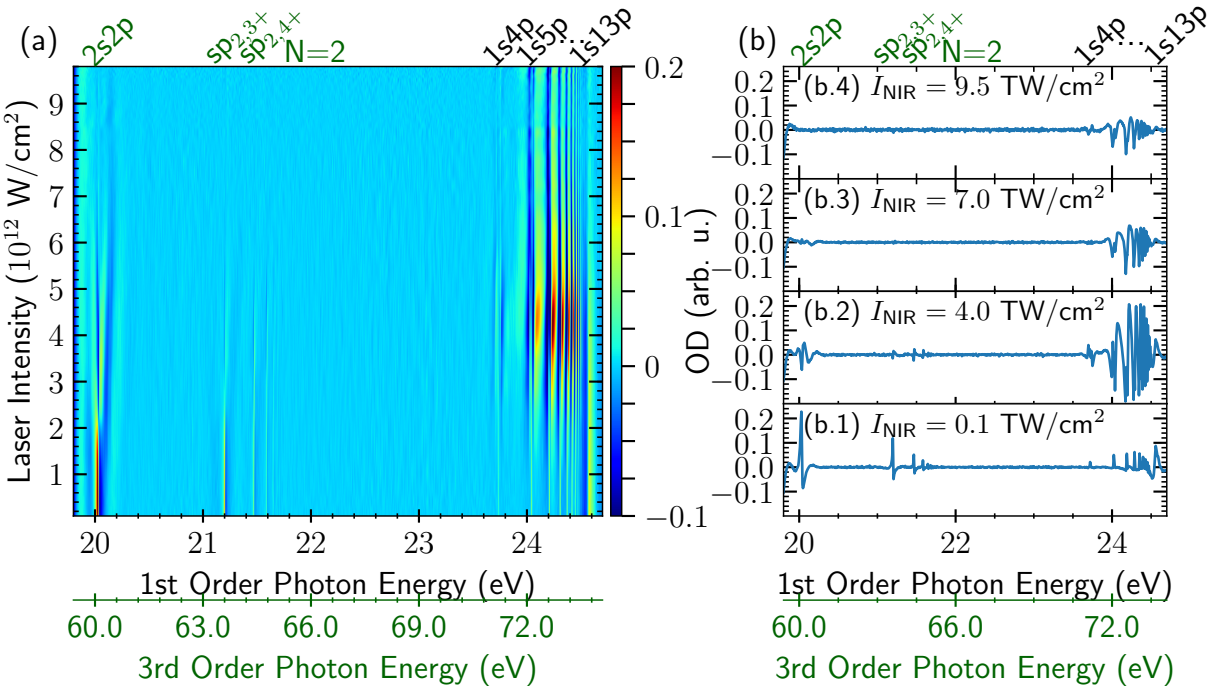

Figure 3.2: Experimental data

(a) Cycle-averaged NIR-intensity scan for intensities between 0.1 and 9.8 TW/cm^2, centred around time-delay $\tau = 5$ fs. On the x-axis, two photon energy scales are shown, corresponding to the 1st (black) and 3rd order photon energy of the spectrometer. The colour code at every energy-intensity point shows the measured optical density OD. On the left side of the plot (green headings and energy scale) the absorption lines of the $sp_{2,n+}$ series of doubly excited states is shown, whereas on the right side (black headings and energy scale) the 1snp series is plotted. **(b.1)** to **(b.4)** Lineouts of the intensity scan at NIR intensities $0.1, 4.0, 7.0$ and 9.5 TW/cm^2 respectively. The lines of the doubly excited states vanish for the highest intensities, whereas the singly excited states are still present.

3.2 Modelling the Helium System

In order to find the cause for the difference in the ionization behaviour of SES and DES in the helium atom, a complete numerical study of the relevant ionization processes was conducted. Using an *ab-initio* time-dependent Schrödinger-equation simulation, single and double ionization rates are calculated. An enhancement of the double ionization in the case of doubly excited states explains the experimentally observed enhanced ionization in the presence of two active electrons. The numerical-simulation approach is presented in the following.

3.2.1 A Two-Electron Model System

The herein employed two-electron model system for the simulation of singly and doubly excited helium, was first suggested by Eberly in the early 90's, [40, 41], and was already discussed in detail in [42] and [43]. A brief summary of the simulation model is given in this chapter.

The numerical implementation of the helium atom as a two-electron system is based on the following assumptions:

- The atom is built out of two pointlike, negatively charged electrons and one pointlike nucleus with a double positive charge.
- Both electrons are indistinguishable.
- The Born-Oppenheimer approximation is employed to separate the motion of electrons and nucleus. The latter is not further taken into account.
- The motion of each of the electrons is restricted to a one-dimensional discrete grid.
- The acting electromagnetic forces in the atom are approximated by the Coulomb force, including the interaction between the electrons. Each of the Coulomb potentials is modified by a soft-core parameter, a for the electron-nucleus attraction and b for the electron-electron repulsion. This form of the softened Coulomb potential is known as the Rochester one-dimensional potential [44, 45] and is used to avoid numerical divergence. The Hamiltonian of the free system is then given by

$$\mathscr{H}_{free}(x_1, x_2, p_1, p_2) = \frac{1}{2}\sum_{i=1}^{2} p_i^2 - \sum_{i=1}^{2} \frac{2}{\sqrt{x_i^2 + a^2}} + \frac{1}{\sqrt{(x_1 - x_2)^2 + b^2}}, \tag{3.1}$$

  where the choice $a = b = 1$ was made for the subsequent calculations. The soft-core parameters change slightly the energies of the bound states in the model atom. They could, however, be varied so that energies obtained in the model are close to those in real 3d-helium. Nonetheless, the discussed model is only one-dimensional and furthermore there are infinitely many bound states in real 3d-helium. For the adjustment of the energies of

all those states the same amount of tuning parameters should be employed to obtain the real energies. Therefore, no special attention was paid in the choice of a and b.

- An external laser field acts simultaneously on both electrons with its polarization component parallel to the direction of the electrons' motion. Since the electrons have no access to the direction perpendicular to the direction of their movement, no magnetic field interaction is taken into account. However, the electric field changes the effective potential of the system, which in the length gauge of the dipole approximation is given by

$$V_{int} = (x_1 + x_2)E(x_0, t). \tag{3.2}$$

Here $E(x_0, t)$ stands for the time-varying electric field, which is constant for the whole extent of the model atom, denoted by x_0. The complete Hamiltonian for the numerical description of the electrons in helium can thus be written as

$$\mathscr{H}(x_1, x_2, p_1, p_2; t) = \frac{1}{2}\sum_{i=1}^{2} p_i^2 - \sum_{i=1}^{2} \frac{2}{\sqrt{x_i^2 + a^2}} + \frac{1}{\sqrt{(x_1 - x_2)^2 + b^2}} + (x_1 + x_2)E(x_0, t). \tag{3.3}$$

- The laser field is approximated by an oscillating cosine wave under a Gaussian envelope in the form

$$E(x_0, t) \equiv E(t) = E_0 \cos(\omega t + \phi) \mathrm{e}^{-\left(\frac{t-t_0}{\tau_\mathrm{G}}\right)^2}. \tag{3.4}$$

E_0 is the maximum of the electric field strength, ϕ is a phase factor which could control the carrier envelope phase and τ_G is a factor associated with the duration of the laser pulse τ_P, defined as the full width at half maximum (FWHM) of $|E(t)|^2$. The connection between τ_G and τ_P is written as $\tau_\mathrm{P} = \sqrt{2\ln 2}\tau_\mathrm{G}$.

After making all those assumptions, the Schrödinger equation to solve the electron motion takes the form

$$i\frac{\partial}{\partial t}|\psi(x_1, x_2; t)\rangle = \mathscr{H}(x_1, x_2, p_1, p_2; t)|\psi(x_1, x_2; t)\rangle, \tag{3.5}$$

where $|\psi(x_1, x_2; t)\rangle$ denotes a time-dependent state vector of the model system. The solution of the equation gives the time evolution of this state. For the purposes of this work, the Schrödinger equation is solved via a split-step algorithm method with second order accuracy, as shown in [46]. For this, $\mathscr{H}(x_1, x_2, p_1, p_2; t)$ is separated into a spatial and momentum part. The time-evolution split-step operator is then

$$U(t + \Delta t, t) = e^{-i\left(\mathscr{H}_p(t) + \mathscr{H}_x(t)\right)\cdot\Delta t} = e^{-\frac{i}{2}\mathscr{H}_x\Delta t} e^{-i\mathscr{H}_p\Delta t} e^{-\frac{i}{2}\mathscr{H}_x\Delta t} + \mathcal{O}(\Delta t^3). \tag{3.6}$$

With this, the propagation of the wave function for one time-step Δt becomes

$$|\psi(t + \Delta t)\rangle = e^{-\frac{i}{2}\mathscr{H}_x\Delta t}\,\mathrm{FT}^{-1}\, e^{-i\mathscr{H}_p\Delta t}\,\mathrm{FT}\, e^{-\frac{i}{2}\mathscr{H}_x\Delta t}|\psi(t)\rangle, \tag{3.7}$$

where FT and FT^{-1} identify as the Fourier transform and its inverse, connecting position and momentum space.

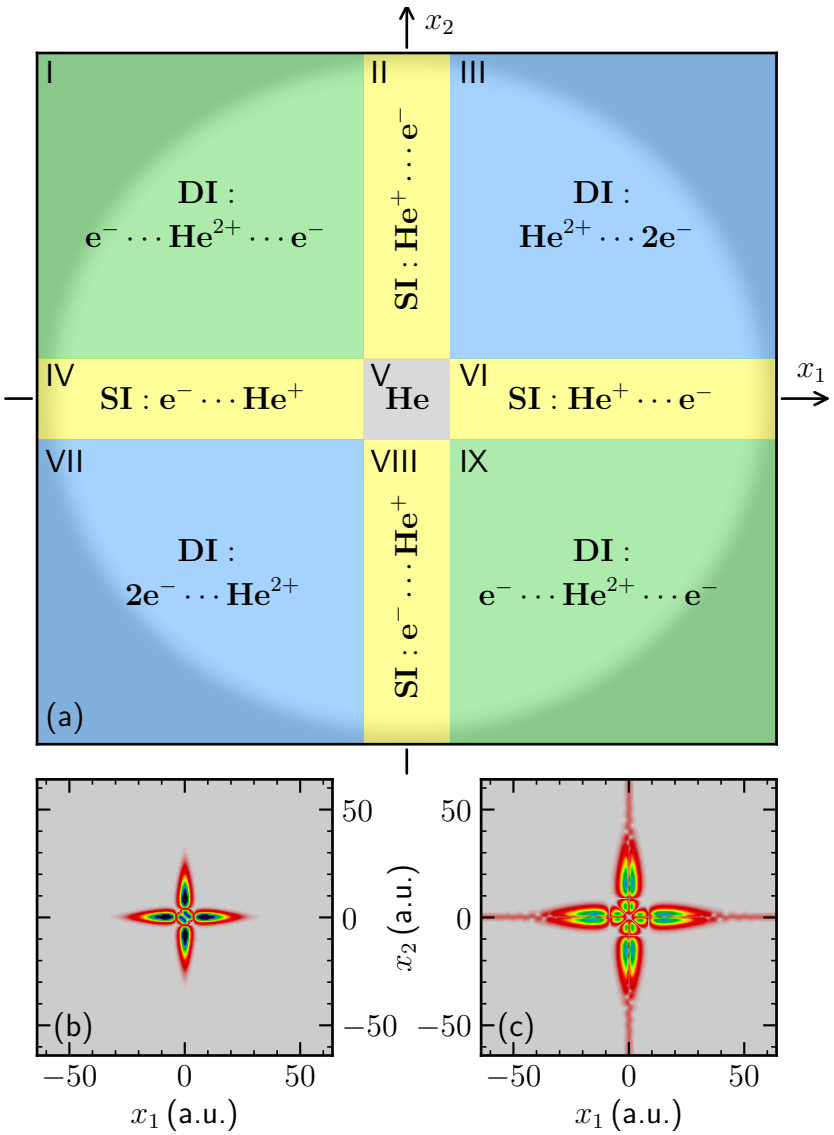

Figure 3.3: Wave function partition scheme

(a) Partition scheme of the two-dimensional wave function grid. Section V (grey) specifies the extension of the atom, including at least 99% of the unperturbed electronic density of each considered excited state. Population of sections II, IV, VI, VIII (yellow) means single ionization (SI) of the atom, whereas population of sections I, III, VII and IX means double ionization (DI), in which process both electrons could escape in the opposite (sections I and IX in green) or in the same (sections III and VII in blue) direction. The shadowed region displays an absorbing boundary of thickness of 100 a.u. with a cosine-squared profile. **(b)** and **(c)** Wave function of the considered singly and doubly excited states, respectively. Both states have the same symmetry and similar ionization potential of around 0.1 a.u..

3.2.2 Numerical Implementation and Simulation Techniques

Having the Hamiltonian of the model system, eq. (3.3), and the time-propagation of a state, eq. (3.7), at hand, the last key ingredient to make the numerical implementation of a one-dimensional helium atom complete, is a way to represent wave functions numerically. To this end, a two-dimensional discrete 4096×4096 grid field with complex number entries at each field point $\boldsymbol{x}$, the square value of which appear to be the electron occupation probability density, is used, where $\boldsymbol{x} \in \mathscr{X} = [-1023.5\text{ a.u.}; -1023\text{ a.u.}, \ldots, 1024\text{ a.u.}] \times [-1023.5\text{ a.u.}; -1023\text{ a.u.}, \ldots, 1024\text{ a.u.}] \cong [1, 2, \ldots, 4096] \times [1, 2, \ldots, 4096]$. To avoid population of the border area to numerically tunnel from one side of the wave function to the other side, and to later on account for ionization, a spherically symmetric imaginary potential, acting as an absorbing boundary, was employed to damp the electron occupation probability density at the borders. The potential used here can be written as:

$$\mathrm{Im}(\mathscr{V}) = \begin{cases} \cos^2\left(\frac{\pi}{2}\frac{r}{(R_{max}-R_{min})}\right) & \text{for } r \in [925\text{ a.u.}, 1024\text{ a.u.}] \\ 0 & \text{for } r < R_{\min} = 925\text{ a.u.} \\ 1 & \text{for } r > R_{\max} = 1024\text{ a.u.} \end{cases} . \tag{3.8}$$

The absorbing boundary in this form is shown as a grey shadow in Fig. 3.3. The described grid is partitioned into different sections, as shown also in Fig. 3.3.

This partition technique has already been successfully implemented in theoretical studies of the ionization of small atoms and molecules [47, 48, 49, 50, 51, 52]. Changes in the electronic density in each of the grid segments account for dynamical effects during the interaction with an external laser field. The partitioning of the wave function is done in such a way that section V defines the size of the atom, meaning that only 1% of the unperturbed wave function of the considered singly and doubly excited states, shown in Fig. 3.3 (b) and (c), is not included in this segment. Observing increasing electronic density in sections II, IV, VI and VIII, means, that one of the electrons is predominantly located near the coordinate system origin, whereas the other electron moves away from it, as in the process of single ionization (SI), where one of the electrons leaves its bound state. Those four sections are thought of as the SI sections. If the second electron also tends to occupy regions away from the origin, then sections I, III, VII and IX are populated and the situation is associated with double ionization (DI), so these regions are called the DI sections. Double ionization could occur right after single ionization, for which vertical or horizontal movement of the electrons away from the SI sections is observed. Non-sequential double ionization has also been recognized in the simulation results by movement of the electrons along the diagonals. How the described ionization processes take on in time, is described in section 3.3. Here, it should be pointed out, that for all calculations, the results of which are discussed in the next section, only the interaction between a pair of a singly and doubly excited state and an NIR pulse with energy spectrum, centred at 1.74 eV $\cong$ 712 nm has

been simulated. This interaction is in fact the second step of the discussed experiment. The first step, excitation of the ground state by an XUV laser pulse, is omitted, but taken into account by setting the maximum of the NIR field 5 fs after the start of the calculations. Furthermore, the excitation of the ground state has been accounted for by preparing excited bound states with the methods discussed in detail in [43]. The considered SES and DES are chosen according to their ionization potential I_P, which for both states is around 0.1 a.u..

3.3 Simulation Results

In this section all simulation results obtained are presented and discussed. The aim of all calculations is to study qualitatively the occurring ionization processes in both singly and doubly excited states.

Studying ionization, the first quantity to look at intuitively appears to be the state probability density $P_\Psi(t) = \langle\Psi(t)|\Psi(t)\rangle$, evolving in time. As mentioned in the description of Fig. 3.3, only the central grid part, section V, is the one containing the unperturbed state. The evolution of $P_\Psi(t)$ for this grid area is calculated and shown in Figure 3.4 (a.2) and (b.2) for the SES and DES, respectively. The remaining probability density $1 - P_\Psi(t)$, being less than one percent for zero field strength, is distributed among all other grid sections and is defined as the ionization probability $P_I = 1 - P_\Psi(t)$. Fig. 3.4 (a.1) and (b.1) show P_I as a function of NIR intensity right after the end of the laser pulse for the considered SES and two different DES, respectively. For both singly and doubly excited cases the ionization probability increases with increasing intensity. It is, however, noticeable that the ionization probability of both doubly excited states reaches 50%, meaning that it is highly probable to ionize at least one electron of the bound state. Such P_I values are observed for intensities comparable to the highest reached in the experiment, where the doubly excited states are completely ionized. In the SES case, on the other hand, the highest reached P_I values do not exceed 45%, which occurs for intensities considerably higher than those achieved in the experiment. This result confirms the expectation that singly excited states can also be ionized by strong field multi-photon ionization, which was so far not observed experimentally. Nevertheless, the threshold for this still remains higher than the one for doubly excited states.

To find out whether the increasing P_I is only due to single ionization rather than double ionization we make use of the partition technique and calculate the single and double ionization yield (SIY and DIY) for both considered states. The results are shown in Fig. 3.5. Fig. 3.5 (a.1) and (a.2) show the time evolution of the integrated wave function in the SI and DI sections for the singly excited state depending on the maximum field strength of the NIR pulse. The same plots for the doubly excited state are shown in Fig. 3.5 (b.1) and (b.2). It stands out that for both states the single ionization arises at earlier times compared to the double ionization, setting around the maximum of the laser field. This points towards the possibility, that the observed ionization is a result of a sequential process. Furthermore, one could not help but notice that

the double ionization yield of the doubly excited state is increased by four orders of magnitude during the interaction with the NIR laser field. The increase of occupation probability in the four DI sections only for the doubly excited state suggests an ionization mechanism involving both electrons, which causes the experimentally observed early ionization of the 2s*n*p states. According to those results it seems likely that the early ionization is due to a two-electron process, where one of the bound electrons has been pulled out by the NIR field, and during this

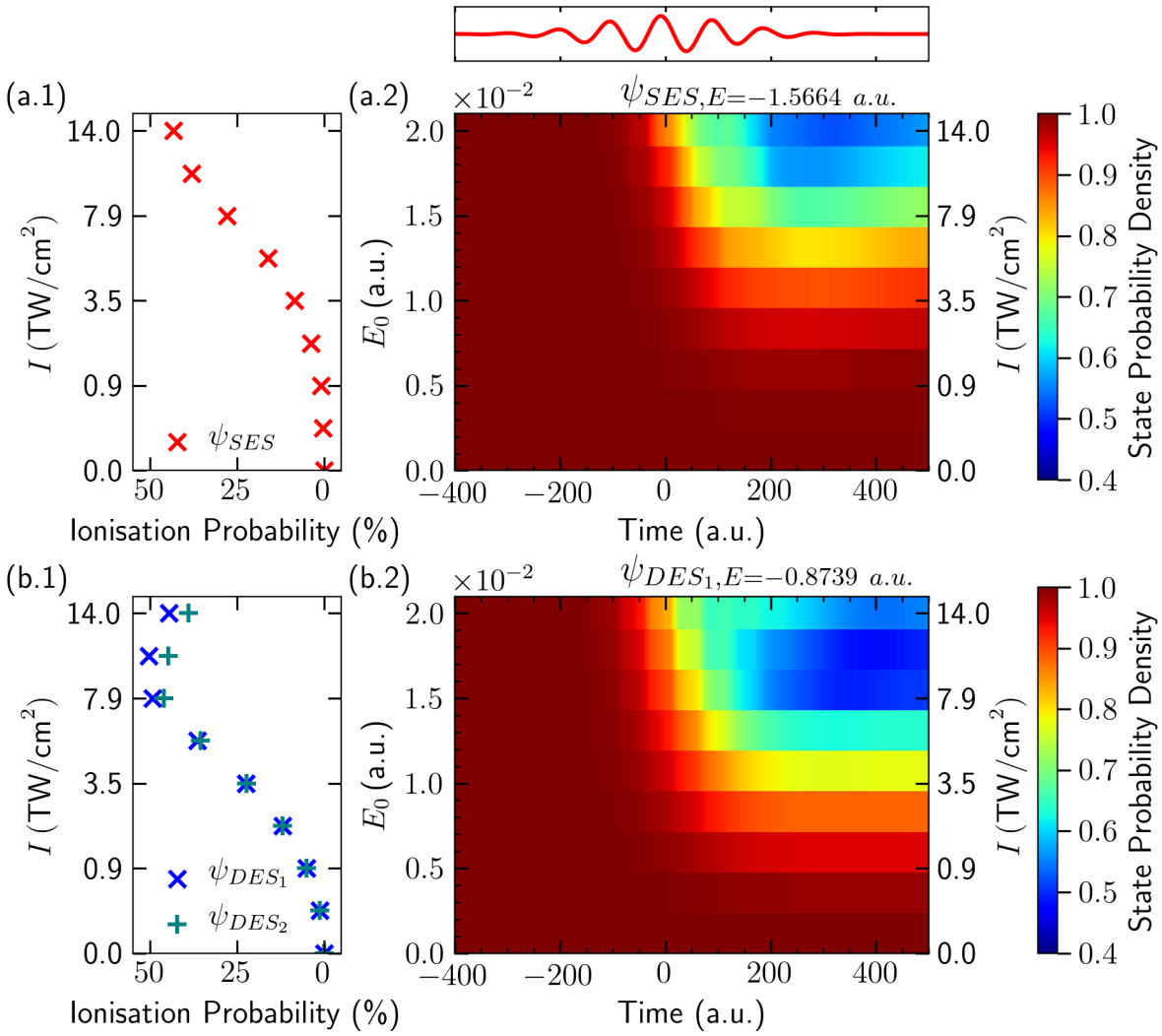

Figure 3.4: Dynamics of the state probability density

(a.1) and **(a.2)** Ionization probability P_I after interaction with an NIR field for different laser field strengths and evolution of the state probability density $P_\Psi(t) = \langle\Psi(t)|\Psi(t)\rangle$ of a singly excited state ψ_{SES}, respectively. **(b.1)** and **(b.2)** Ionization probability P_I and state probability density $P_\Psi(t) = \langle\Psi(t)|\Psi(t)\rangle$ for two doubly excited states ψ_{DES_1} and ψ_{DES_2}. In both cases $P_\Psi(t)$ is calculated only for region V in Fig. 3.3, where the electronic density in all other sections and the parts absorbed by the damping potential define the ionization probability P_I for each state. The higher E_0, the bigger P_I, approaching 50% for NIR intensities comparable to the highest achieved in the experiment. The ionization threshold of the singly excited state appears to be at higher NIR intensity than for doubly excited states.

process also extracts the other electron.

Trying to confirm such an ionization mechanism, the wave function in all sections, except for IV, V and VI, is projected to the x_1-axis, making the observation of its spread along one of the electron dimensions possible. This way the behaviour of the closer bound electron is easily accessible. Fig. 3.6 gives an illustration of the procedure, where the projected region is marked in light gray and the remaining in dark grey. The projection in the illustration, figure 3.6 (a.2) and (b.2), is for the unperturbed states.

Considering moderate to low NIR intensities, as in Fig. 3.7 (a.1) and (b.1), showing the

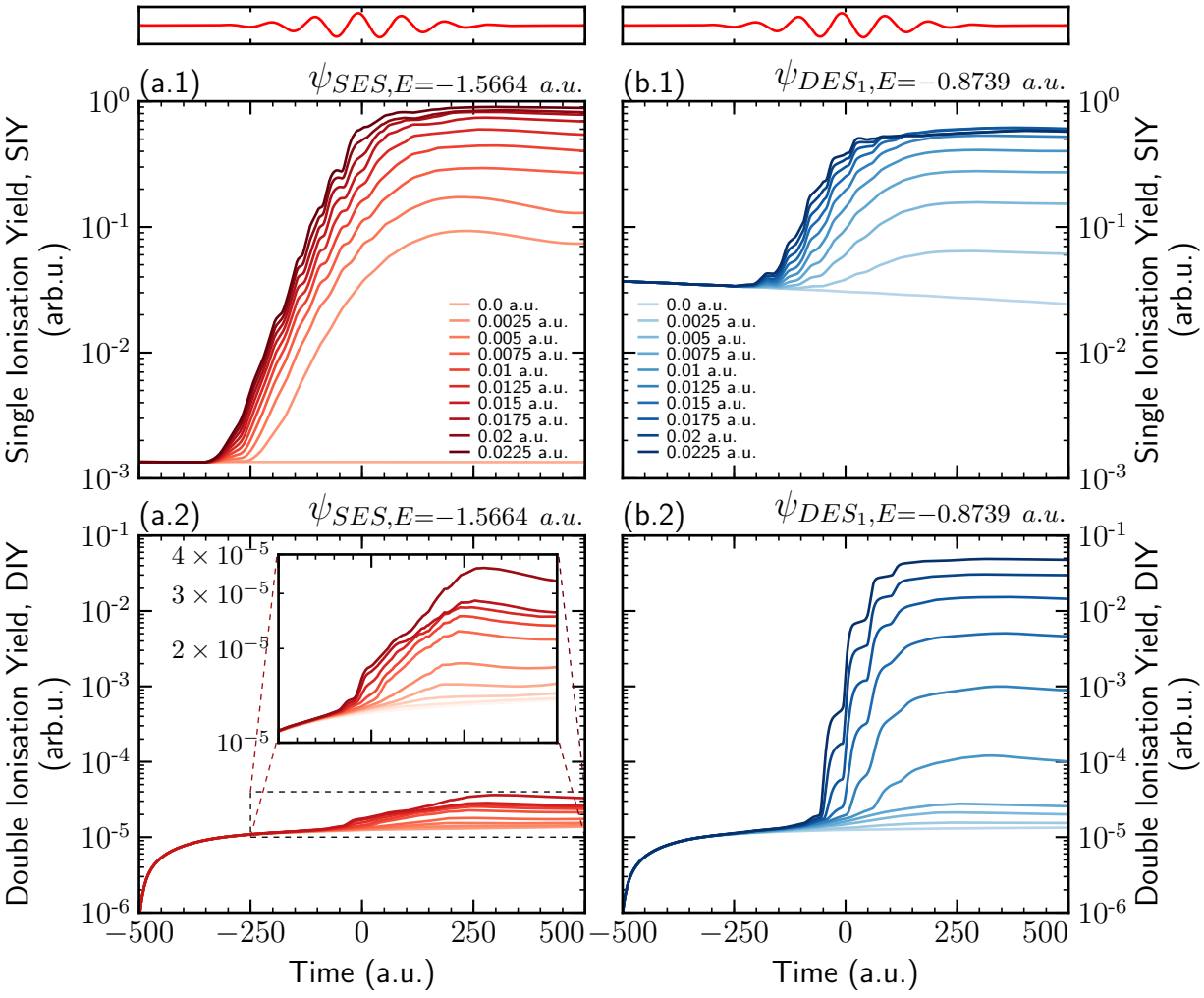

Figure 3.5: Single and double ionizetion yield

(a.1) and **(a.2)** Time evolution of the integrated wave function in the SI and DI sections, single and double ionization yield respectively, of Figure 3.3 for the singly excited state ψ_{SES} depending on the maximal field strength of the NIR pulse.
(b.1) and **(b.2)** Single and double ionization yield for the doubly excited state ψ_{DES_1} as a function of the field strength of the NIR pulse.
The single ionization yield, SIY, of both states rises continuously after the beginning of the NIR pulse, whereas the double ionization yield, DIY, increases after the maximum of the laser pulse and is 4 orders of magnitude higher for the DES than in the case of SES.

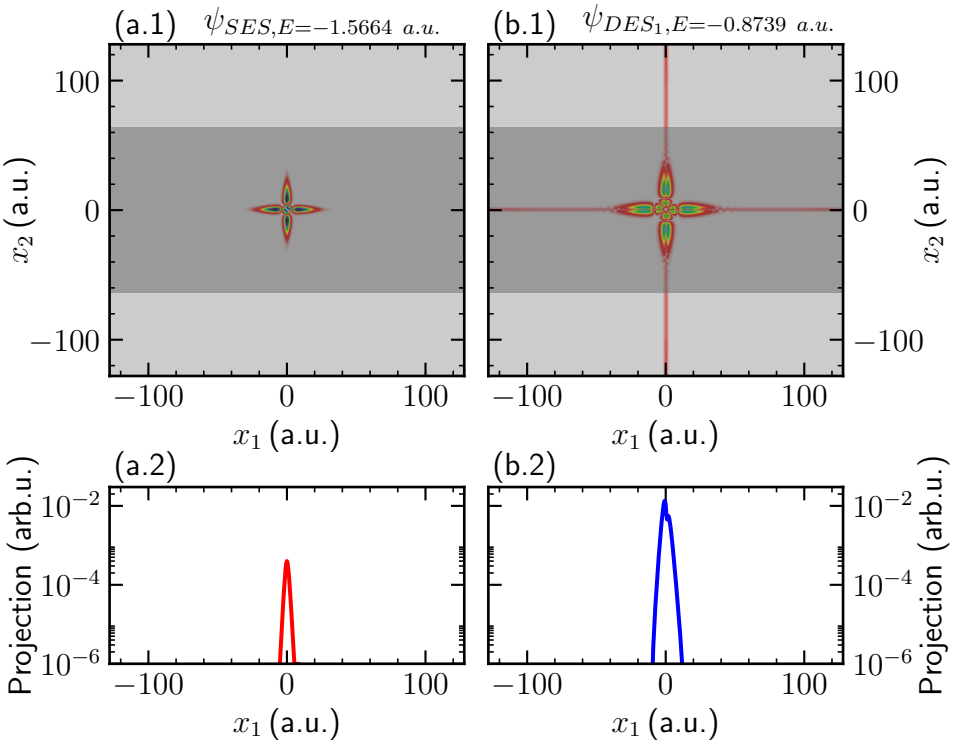

Figure 3.6: Wave function projection to obtain wave function spread
(a.1) and **(b.1)** Wave function projection procedure illustrated for the singly and doubly excited state, respectively. All of the wave function but the part in dark grey is projected onto the x_1-axes. **(a.2)** and **(b.2)** Projection of the unperturbed SES and DES onto the x_1-axes.

wave function spread for $E_0 = 0.005$ a.u. NIR field, no significant difference between the singly and doubly excited state can be observed. For higher intensities, however, in the case displayed in Fig. 3.7 (c.1) and (d.1), at field strength $E_0 = 0.02$ a.u., the plotted time evolution of the doubly excited states is broadened along the initially closely bound direction. The broadening sets on around the maximum of the electric field, just as the double ionization yield discussed above. Taking a closer look, this is right after the central part of the projection around $x_0 = 0$ a.u. becomes more intense, or after the single ionization yield reaches 5 to 10%. After the initial increase of the broadening, it becomes wider for later times.

To examine how exactly the wave function evolution changes in time and this broadening occurs, Fig. 3.8 and Fig. 3.9 show the spatial wave function for both the singly and doubly excited state for 16 points in time during the interaction with an NIR field of maximal field strength $E = 0.02$ a.u.. Here, no population of the DI sections can be observed for the SES, whereas the DES spreads noticeably in the DI sections, after previously populating the SI regions (vertical and horizontal movement indicated by arrows in Fig. 3.9 (6) and (7)), but also non-sequentially, suggested by the diagonal structures in Fig. 3.9 (6), (8). This plot once again suggests that double ionization is more probable for doubly excited states and that it occurs in

the first place sequentially, after single ionization, but also non-sequentially.

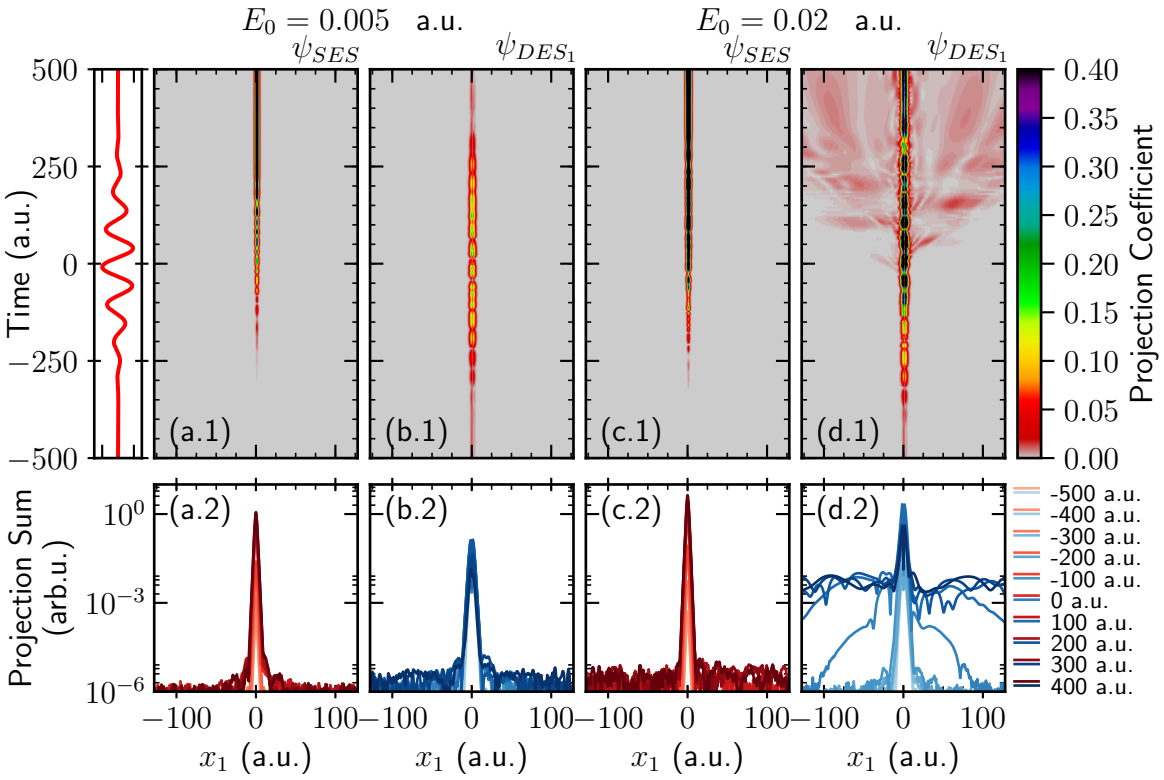

Figure 3.7: Wave function spread

The time evolution of the wave function spread, found by the procedure, described in Fig. 3.6, is shown for low laser field strength, E_0 = 0.005 a.u., in **(a.1)** and **(b.1)** for ψ_{SES} and ψ_{DES_1} respectively, and also for high laser intensity with E_0 = 0.02 a.u. in **(c.1)** and **(d.1)** for ψ_{SES} and ψ_{DES_1} respectively. Lineouts of the respective projection evolution for every 100 a.u. time propagation are shown in **(a.2)** to **(d.2)**. For low NIR-field strengths no considerable difference is observed except for the fact that population in the projected regions of the DES is present from the beginning of the laser interaction, because the DES is an autoionizing state. This is the reason why the SIY of the doubly excited state in Fig. 3.5 (b.1) is one order of magnitude higher than the SIY of the singly excited state. For high enough intensities, after the laser field maximum, the DES wave function spreads even out of the SI region. This spread is not observed for the SES wave function.

3.4 Summary and Conclusions

To briefly summarize this section, the method of attosecond transient absorption spectroscopy was employed in the perturbative and strong field regime to study the different ionization behaviour of atomic states in the helium atom, involving one or two excited electrons. The different ionization thresholds of both detected atomic line series, 1snp and $\mathrm{sp}_{2,n+}$, were made plausible by a theoretical study of a model helium atom in two dimensions, one for each

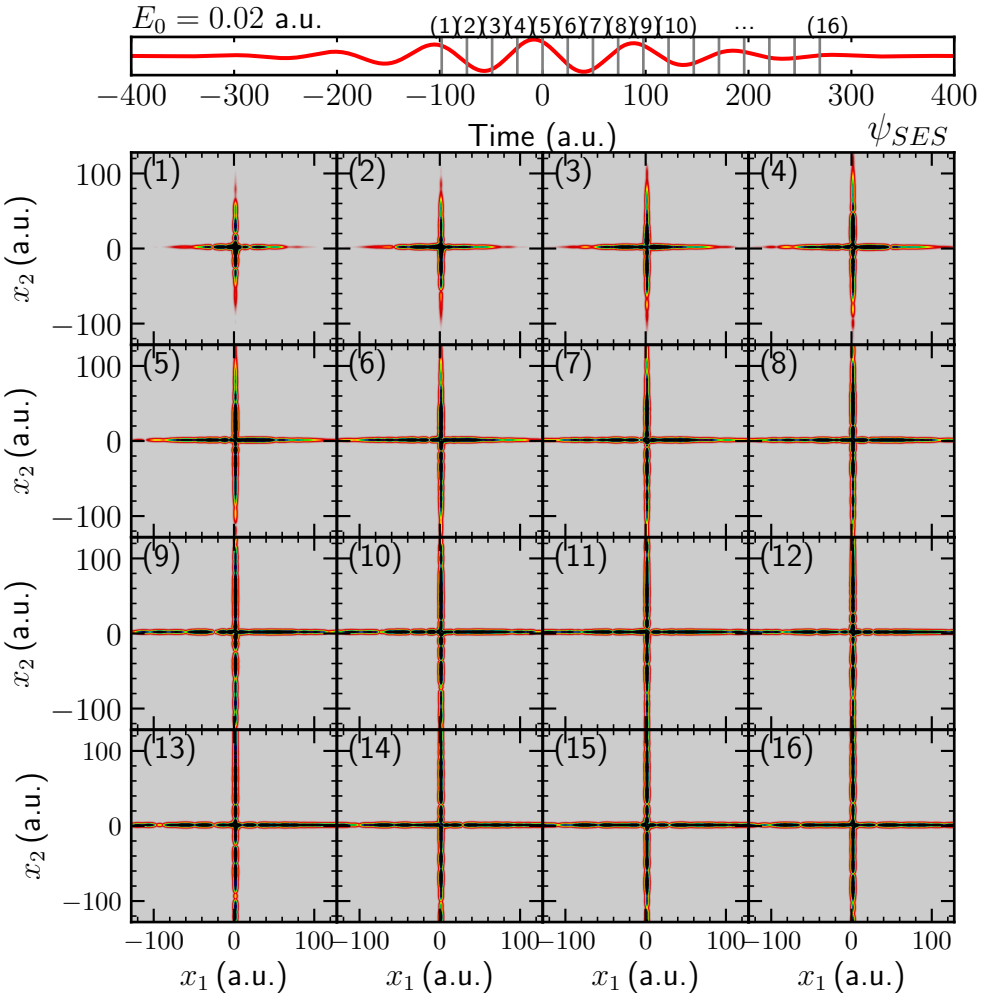

Figure 3.8: Evolution of the SES wave function, ψ_{SES}, for an NIR field of $E_0 = 0.02$ a.u. Time evolution of the spatial wave function of the singly excited state ψ_{SES} at 16 different times during the interaction of an NIR field of $E_0 = 0.02$ a.u.. The chosen time instances **(1)** to **(16)** are shown over the E-field illustration in the figure. The considered time range begins one cycle before the maximum of the laser field envelope and ends three cycles later. The time points are set so that in each laser cycle at least four points are sampled. In the SES wave function no significant spread outside the SI region is observed.

electron, interacting with an NIR field. The simulation results show increased ionization probability for the considered lowest doubly excited state in comparison with the singly excited state with the same symmetry and similar ionization potential of 0.1 a.u.. While the single ionization yield of both states is of the same order of magnitude, the doubly excited state exhibits four orders of magnitude higher double ionization yield, Figure 3.5. At the same time Figure 3.7 shows that the stronger bound electron becomes more loosely bound after the maximum of the laser field envelope, at which point the double ionization is enhanced. With respect to these results, the following ionization mechanism is suggested: the NIR-laser interaction ionizes the initially stronger bound electron of the doubly excited states and through this also removes the other electron with the help of the electron-electron interaction. Such a mechanism is in agree-

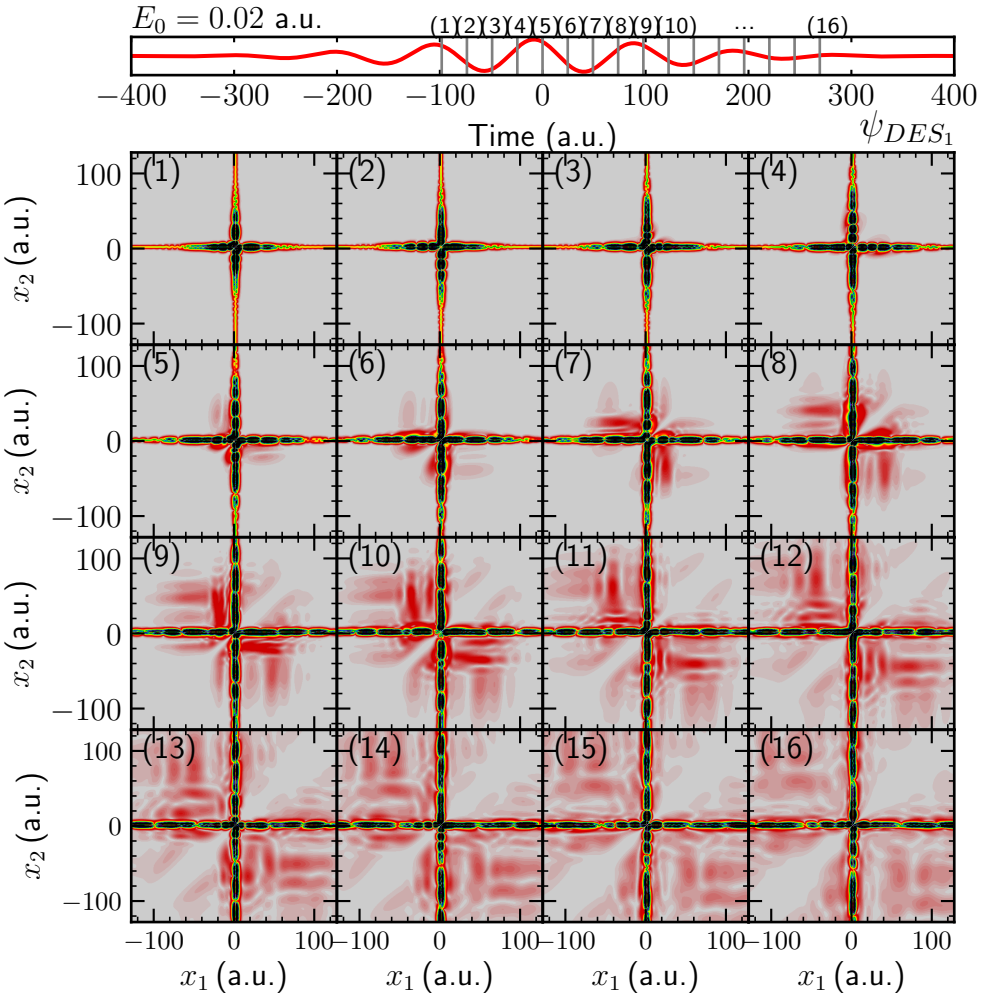

Figure 3.9: Evolution of the DES wave function, ψ_{DES_1}, for an NIR field of $E_0 = 0.02$ a.u. Time evolution of the spatial wave function of the doubly excited state ψ_{DES_1} during the interaction of an NIR field of $E_0 = 0.02$ a.u.. The considered time range is the same as in Fig. 3.8. In the DES wave function evolution there is a significant spread outside the SI region after the maximum of the laser field, for example at times (4) and (5).

ment with the experimental observation, shown in Figure 3.2, where all doubly excited states with a 2s electron ionize at the same NIR intensity.

Chapter 4

Transient Absorption Studies of the Q_n Resonances of Molecular Hydrogen

The hydrogen molecule, together with helium, is the simplest neutrally charged system, exhibiting full electron correlation dynamics. The two electrons in H_2 can both be excited to superexcited states, as discussed in Cha. 1.3.3. Such states in H_2 are frequently referred to as Q_n resonances, which have been a subject of both theoretical and experimental studies [53, 19]. Reflecting the fact that a two-electron and two-nuclei system is manageable to implement in numerical models, especially in the Born-Oppenheimer approximation to separate the electronic and nuclear degrees of freedom and even though, or perhaps because the equations of motion for the entire quantum system cannot be solved analytically, there has been huge theoretical interest in the hydrogen molecule [6, 54]. In the last years even full-dimensional $ab-initio$ simulations of the hydrogen molecule have become available [19, 6]. Parallel to the attempts to solve the equations of motion without any approximations and even going beyond the Born-Oppenheimer approximation, simple models of the molecule have been developed to study specific processes such as ionization or molecular dissociation [51, 55, 56, 50]. Naturally, when talking about (auto-)ionization and dissociation at the same time, we come back to the Q_n resonances in H_2 as states exhibiting all of those effects. The previously pointed out theoretical approaches have successfully been implemented to study the real-time dynamics of the doubly excited states in H_2 and have even gone ahead of experiments, confirming some, but not all theoretical predictions. For example, photoabsorption studies of time-dependent dynamics of doubly excited states in the hydrogen molecule have been hardly conducted experimentally, because of the difficulties, connected to measuring absorption changes, embedded in the ionization continuum of hydrogen. On the other hand, a number of experimental studies have reported on photoionization electrons [7, 57, 15] and some even focused on DES dynamics [7]. A recent theoretical paper, making predictions for the autoionization dynamics of Q_n resonances, imprinted in the photoionization electrons, have been published with a title raising a question that one might ask oneself when being used to atomic autoionization dynamics: "Autoionization of Molecular Hydrogen: Where do the Fano Lineshapes Go?" [5]. This and subsequent theoretical works of

the authors have motivated the studies of autoionizing Q_n states in molecular hydrogen by employing the attosecond transient absorption spectroscopy technique and the transient coupling scheme, as presented in this thesis. This chapter gives a detailed overview on the current status of the absorption studies of autoionization dynamics in DESs in molecular hydrogen, developped entirely in the scope of this thesis. Section 4.1 summarizes the measurement procedure and data evaluation techniques. Together with the experimental preparations, presented in Sec. 4.2, the first two sections of this chapter sum up the background theoretical and experimental knowledge for the data evaluation shown in Cha. 4.3, especially considering the experimental limitations and systematical effects arising from the nature of the experimental setup. After discussing the experimental results in Sec. 4.3.3, a simple model implementation of the hydrogen molecule, which can be used to simulate the measured data and confirm the interpretation of the experimental results, has been developed, Sec. 4.4. At the end, a brief section summary, Sec. 4.5, is given.

4.1 Experiments in Hydrogen

Before going in detail into the experimental preparation and data analysis, we come back to the simple question: What do we want to measure? It has already been answered in the introduction of this chapter: (auto-)ionization dynamics of the Q_n resonant states in molecular hydrogen. The experimental method of choice for this is the attosecond transient absorption spectroscopy technique together with the transient-coupling scheme, Sec. 1.2.2, manifesting themselves when measuring absorption signals at negative (NIR first) and positive (XUV first) time delays between the pulses, respectively. Autoionzation lifetimes of some Q_n resonances have been theoretically and experimentally estimated [7]. Within the autoionization lifetime of the DESs a change in the absorption signal should be evident in time-dependent absorption studies. However, in the transient-coupling scheme autoionization would be only detectable for the small coherent time-period of the Franck-Condon-overlap region. Since the Q_n resonances dissociate on a time scale of only a few femtoseconds, for some states it takes even less than one femtosecond for the dissociating nuclear wave packet to leave the Franck-Condon region, short NIR pulses and isolated attosecond XUV light pulses are required, otherwise one would not be able to see much of an effect in the absorption signal that is associated to these states. Additionaly to this difficulty, according to literature about absorption cross sections of hydrogen, Q_n resonances would manifest themselves as a broad signatures (around 10 eV), which is embedded in the overall absorption continuum cross section in H_2, which will make time-dependent absorption changes difficult to detect.

4.1.1 Measurement Procedure

To measure transient absorption signals in the hydrogen molecule, the following measurement procedures were employed:

- detection of OD signals as in Eq. (1.13), measuring references $I_0(\omega)$ being XUV spectra without hydrogen target gas:
  For measuring OD signals, spectra when moving the target cell in and out of the laser interaction region has been measured, where the latter serve as reference spectra. This requires movement of the target cell after each recorded spectrum at a distance of around 5 mm, which proved impracticle for measurements where a lot of statistics is needed, as here, where sensitivity on the order of a few mOD units is required. Furthermore, in this measurement procedure it is difficult to correct for all systematic effects arising from the changing geometry between absorption and reference spectra.

- detection of ΔOD signals

$$\Delta\mathrm{OD}_\tau(\omega) = -\log_{10}\left(\frac{I_\tau(\omega)}{I_{\tau=\tau_{REF}}(\omega)}\right) = \frac{\Delta\sigma(\omega)}{\ln 10}\cdot\rho_\mathrm{N}\cdot l, \tag{4.1}$$

  which is proportional to changes in the absorption cross section when all other parameters in Eq. (4.1) are kept constant in an experiment: To obtain $\Delta\mathrm{OD}_\tau(\omega)$ (hereafter denoted as ΔOD) data, the target cell was initially positioned and kept constant in the region of the overlapping foci of both the XUV and NIR pulses. In the measurement sequence, an absorption spectrum at a time delay τ was referenced always at a negative time delay, τ_neg, the same for all absorption spectrum at a time delay τ. Since time delays are always adjusted via moving a piezo stage in space (the one the inner mirror is mounted on), the data acquisition series was similar to piezo set values s (in µm): s_0,s_0,s_0+Δs,s_0, s_0+2Δs ,s_0,..., s_0+nΔs, s_0 or in time delay notation: τ_neg, τ_neg, τ_1, τ_neg, τ_2, τ_neg, ... , τ_n, τ_neg, for a scan where signals at $n+1$ TD points were measured. The time delay scans always started at negative time delays and ended at positive time delays.

For both measurement routines, at the beginning or the end of a TD-Scan for some iris set value background spectra were recorded in all three cases

- HHG gas on, target gas off
- HHG gas off, target gas on
- HHG gas off, target gas off

with the target cell being in or out of the interaction region with the laser pulses.

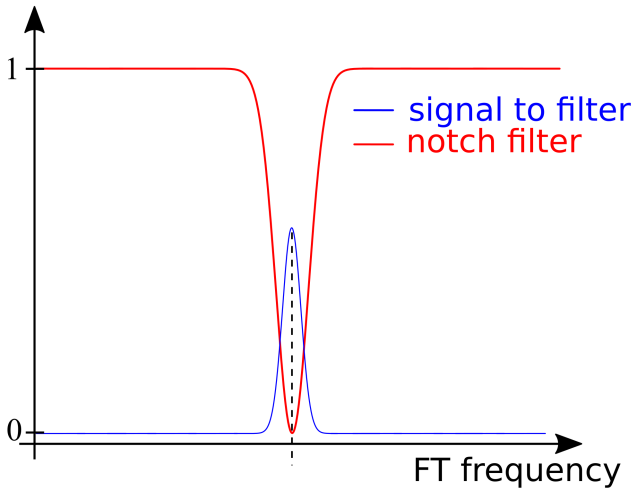

Figure 4.1: Notch filter
A notch filter (red curve) with a Gaussian profile is applied to attenuate a range of frequencies in the Fourier-transform signal of a function (blue curve).

4.1.2 Data Evaluation

The measured data is directly evaluated by calculating OD or ΔOD signals from the recorded spectra after subtracting the corresponding background data. For a ΔOD measurement from the spectral data the background with HHG gas off and target gas on for the respective TD position was subtracted from the spectra. The obtained TD-Scans are shown in Sec. 4.3 as raw data. Further data analysis included removing the remaining harmonics modulation in the the ΔOD data by applying a notch filter, which attenuates the Fourier space frequencies of a ΔOD spectrum arising from the harmonics modulation (≈ 6 cycles in the considered energy region). Figure 4.1 shows a sketch of the principle of the notch filter, successfully applied in other absorption studies [58].

4.2 Experimental Preparation

To be able to detect such time- and energy-dependent minimal changes in the XUV absorption of hydrogen, as discussed in the previous section, thorough preparation is needed. Therefore, all experimental methods employed to reach the required detection sensitivity are presented in the following. Part of the experimental approach was considered beforehand, knowing details about the studied molecular system, as the potential energy curves of H_2, Sec. 1.1.2, estimates of the life-time of the doubly excited states as in ref. [57] or the measured energy-resolved cross section data at synchrotrons, Sec. 1.2.3. Other effects, however, were encountered after having already measured absorption data of H_2 as a target gas. For the interpretation of most of the initially detected signals, certain pitfalls of the experimental setup needed to be carefully taken into consideration. Geometrical changes of the XUV beam path, hardly taken into account for previous studies of the group, and negligible when looking at

sharp resonances of atoms or molecules [34, 8, 2, 3, 4], now turned out to have a major contribution when aiming at the detection of signal changes of the order of less than 10^{-2} OD units. Including all these corrections, which will be discussed in this section, satisfactory detection sensitivity can be reached, allowing for a first interpretation of the recorded experimental data in molecular hydrogen and giving a hint on the electron dynamics of the Q_n resonances.

4.2.1 Laser Parameters for the Experiments

The lifetime of some Q_n DESs in H_2 is estimated to be less than a femtosecond, e.g. for the lowest DES $Q_1\,\Sigma_u^+$ a lifetime of 400 as to 1 fs was measured [7]. Therefore, as short as possible NIR pulses should be employed in the pump-probe experimental scheme. Additionally, proper CEP stability of the NIR pulses is needed to generate isolated attosecond light pulses in the process of HHG, as discussed in Sec. 1.4.1.

Typical NIR Light Spectra

To start with, the NIR light pulses used in the experiments are characterized by means of the D-Scan technique, as briefly introduced in Sec. 2.1.2. A typical, less than 5 fs short NIR pulse is shown in Fig. 4.2 (a.1) and (a.2), intensity envelope in the time-domain and spectrum in the frequency domain, respectively. Those pulses, however, are characterized before they are coupled into the experimental beamline. When they hit the H_2 target, the spectral and temporal characteristics of the NIR light are slightly modified, mainly due to its previous use of driving the HHG process (photon absorption to drive HHG, e.g. plasma dispersion and self phase modulation) and subsequently passing through the iris aperture. This modification of the spatial NIR beam profile is most prominent at rather small iris settings for measurements at relatively low NIR intnesities. Furthermore, only part of the NIR light propagates towards the interaction region with the target, after being reflected off the split-mirror setup and after going through the filter unit. For a hint on the temporal duration of the NIR pulses in the target chamber, experimental studies in helium have been carried out for the old laser setup [2, 9]. Moreover, measurements in helium were also used for an intensity calibration, after comparing the experimental results to *ab-initio* or few-level simulations, as documented in [2, 3, 30]. A corresponding iris-opening-to-intensity mapping study for the new laser setup is currently a major part of [35]. Another ongoing project will deal with the *in-situ* spectral characterization of the NIR light inside the target chamber. Both mentioned approaches will help characterizing the NIR light pulses that are interacting with the target gases.

Characterization of the XUV Radiation

In any case, the NIR pulses, generating the XUV light in the process of high-order harmonics generation, are well known after a D-Scan measurement. Considerable effort was undertaken

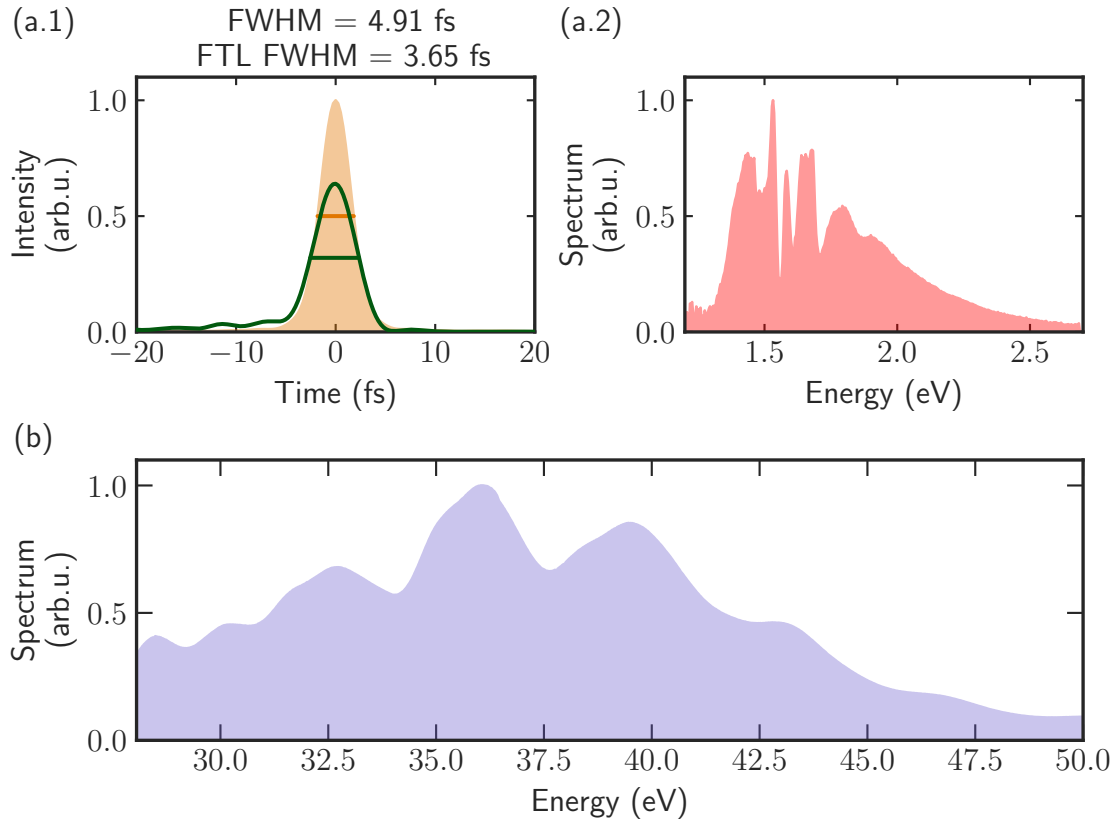

Figure 4.2: Typical NIR and XUV laser spectra

(a.1) and **(a.2)** Typical intensity profile in the time domain and energy spectrum of the NIR light pulses, respectively, as measured in a D-Scan run before coupling in the beamline for experiments. The duration of the NIR pulses is less than 5 fs. A weak pre-pulse is typically measured. The energy spectrum spans between 1.3 and 2.5 eV, and has a maximum between 1.5 and 1.7 eV, corresponding to roughly 775 nm. **(b)** HHG spectrum generated in argon, measured in the energy region between 28 and 50 eV, which is the region used for the experiments in this chapter. The XUV spectrum around 30 eV exhibit shorter peak-to-peak distance, since in this region, light from the second grating order is detected on top of the light from the first diffraction order. The contribution of the second order should be minor, since the effectivity of the VLS grating drops drastically for light with energy higher than 55 eV.

to adjust the right phase-matching conditions for the HHG process in argon and obtain nearly isolated attosecond XUV light pulses. A typical XUV spectrum in the relevant energy region between 28 and 50 eV can be found in Fig. 4.2 (b). Since distinct harmonic orders can be identified as broad structures in the argon HHG spectra, it can be assumed that a closte-to-isolated XUV pulse is produced to later interact with the target molecules, with only a small contribution of satellite pulses evidenced by a small residual harmonic modulation. For a quantitative characterization of the light emerging out of the HHG region, the well established streaking technique [59] utilizing the electron time-of-flight spectrometer would be the method of choice. This was, however, not included in the scope of this thesis and here we only rely on the measured XUV spectra as a characterization tool of the XUV radiation.

4.2.2 Energy-Axis Calibration

Apart for characterizing the laser radiation of both the XUV and NIR pulses, precisely knowing the energy range of the detected absorption signals is important for spectroscopic studies. For the XUV energy-axis calibration, we looked at absorption signals of He and Ar, which have resonances in the experimentally relevant XUV region between 25 and 65 eV, where DESs in H_2 can be populated with a one-photon transition from the ground state of the molecule. In the calibration procedure, all 1340 CCD camera pixels are mapped to an energy value via fitting the position of known lines (in the case of helium, the first four DES resonances) with the grating equation (2.3), when knowing parameters such as the position of the camera chip relative to the VLS grating and the grating order of the detected light. It is important to mention in this context that the He resonances of doubly excited states, as listed in Tab. 1.1, were detected in the second grating order. The energy calibration in helium and argon is shown in Fig. 4.3 (a) and Fig. 4.4 (a.1), respectively, where the natural line shapes, as resolved in the spectrometer setup, is detected for the considered most negative time delays. The literature energy value for the lines in the argon spectra are listed in Tab. 4.1. Those are lines of the $3s3p^6np$ resonance series, known as window resonances.

4.2.3 Time-Zero Calibration

A crucial point for the time-dependent absorption studies presented in the next section is the time-zero calibration. The spectral lines of both helium and argon, detected for calibration of the energy axis, can also be used for finding the zero time delay between the NIR and XUV pulses. An alternative method would be streaking with the electronic time-of-flight spectrometer [9, 31]. In this thesis, however, the calibration method of choice was the *in-situ* measurement of the well-studied He and Ar, and especially looking at autoionizing states in both species.

Series	State configuration	Energy (eV)	Decay rate (meV)
Window resonances in argon	$n = 4$	26.606	76
	$n = 5$	27.993	25
	$n = 6$	28.506	16
	$n = 7$	28.757	9
	$n = 8$	28.898	10

Table 4.1: Energies and decay rates of considered resonances in argon

Resonant excitations in argon, belonging to the $3s^23p^6np$ seris. Data taken from Sorensen et al Phys Rev A 50 (1994).

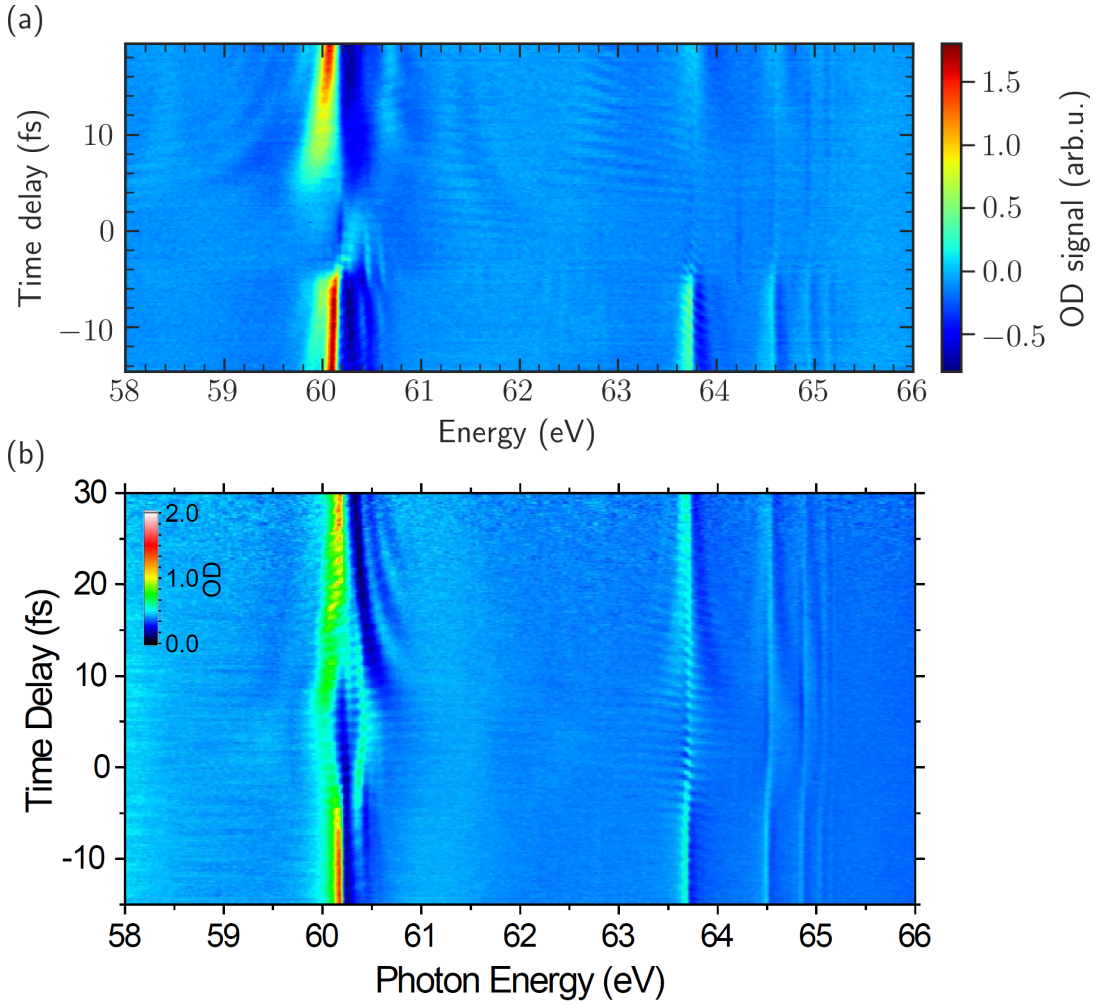

Figure 4.3: OD signal spectra as a function of time delay for an iris set value of 55 (opened apperature)

(a) and **(b)** Measured OD signal for an opened iris aperture with NIR light pulses from the new and the old laser setups, respectively. In both cases the spectra are obtained from measured absorption signals and *in-situ* reconstructed references by means of a Fourier-transform method, as described in [2]. The zero time delay postion in **(a)** is found by a comparison with the data in **(b)**, taken from [2].

Calibration in Helium

Helium is doubtlessly the most studied atomic system in our research group. Intensity- and time-dependent effects on the doubly excited resonances in helium have been thoroughly investigated in previous experimental and theoretical works [2, 3, 4]. Measured time-dependent effects on the DES resonances, known as Fano lines [1], can be easily compared to simple few-level calculations, as done in [2] or even to full-dimensional *ab-initio* calculations [4, 8]. Making such a comparison between simulated and measured time-delay scan (TD-Scan) data, where the simulation laser parameters are adjusted to reflect the experimental laser parameters, such as NIR intensity and pulse length, the time-zero position relative to the movement of the piezo stage of the inner mirror in the split and delay unit can be determined with an accuracy

of around 1 μm, corresponding to a time accuracy of around 1.7 fs. What exactly is compared between experiment and theory is the time-delay region, where the autoionizing states are depleted, i.e. the absorbance in the region is weaker, and therefore the resonance lines distorted. Knowing the adjusted time-delay parameters in a corresponding simulation, the zero position of the time delay τ_0 can be extracted from measured TD-Scans. A comparison between helium data measured for the calibration purposses of this thesis, Fig. 4.3, and previously measured data, which was calibrated in time after conducting simulations with laser paramteres as in the experiment (for the old laser setup) [2], yielded

$$\tau_0 \equiv (103.6 \pm 1.0)\ \mu\text{m}. \tag{4.2}$$

More thorough calibration with data measured particularly for time-zero and energy-calibration purposes is compared to calculated TD-Scans with parameters adjusted to the new laser setup, independently determined $\tau_0 \equiv (102.5 \pm 0.5)$ μm. For more details on the data evaluation in this case, please refer to [35].

Calibration in Argon

During the autoionization time of the window resonances of argon, similarly as for the doubly excited resonances of helium, which can also autoionize, the absorption lines of argon vanish, so that the autoionzation time of the excited states, associated to the resonant absorption lines, is imprinted onto the time transmitted XUV spectra of argon, as reported in [60]. In a TD-Scan in argon the absorption signal is asymmetrically weakened with respect to the delay, which according to [60] can be fit by a cross-correlation of an exponential function with the autoionization state lifetimes and a Gaussian laser pulse. From the fit function, assuming the literature value for the autoionization state lifetimes, a hint on the NIR laser pulse duration can be gained. Here, however, no detailed analyses of the argon data shown in Fig. 4.4 (b) is performed, so that we only make use of the fact that $\tau_0 \widehat{=} (103.6 \pm 1.0)$ μm, determined from the helium data, is inside the absorption-weakening region, to independently confirm the time-delay zero position.

4.2.4 Experimental Limitations

While all experimental preparations discussed so far are part of the standard procedure for getting ready to conduct a spectroscopic experiment, the setup limitations addressed in this section appear to be of importance only for certain studies and can otherwise be neglected for having only a minor influence on the measured data. Those effects are related to the nature of the chosen experimental TAS technique and the used apparatus and became apparent only after performing first experiments.

Section 2.2 already includes a brief summary on the experimental setup, focusing mainly

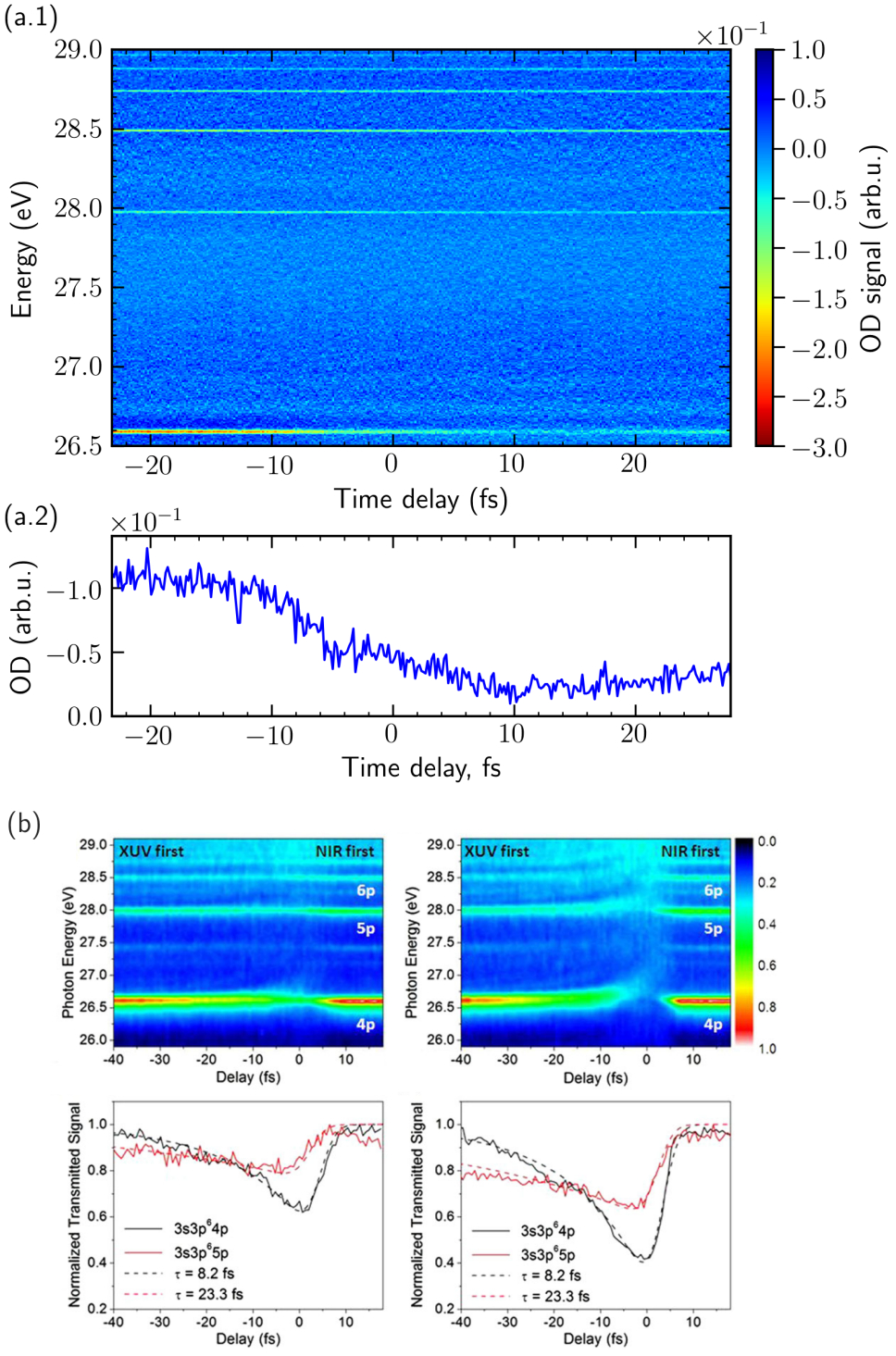

Figure 4.4: Absorption spectra of argon in a strong NIR laser field

(a.1) Measured absorption signal in argon for a TD range between −24 and 26 fs, where positive and negative time delays are defined according to 1.3. **(a.2)** Time-delay lineout for the $n = 4$ window resonance at energy around 26 eV. **(b)** Transmitted attosecond XUV spectra of argon, as measured in [60], figure taken from there. Note, that the convention for the TD axis in reference [60] is reversed compared to the convention in this thesis, Sec. 1.2.2.

on the working principles of the different beamline parts. Here, the key features of the interferometric setup for transient absorption studies are discussed again, with emphasis especially on the setup constraints within the context of a spectroscopic study of broad continua signatures, embedded in the ionization continuum and only slightly changing with time delay.

Spectrometer Constraints:

The adequate resolution of the home-built spectrometer apparatus (≈ 40 meV [2]), perfectly suitable for detection of narrow absorption lines as those in helium and argon, turns out to be of minor importance for the studies of the dynamics of the Q_n resonances in hydrogen. It was mainly made use of for calibration purposes. Constructed with the intention to resolve even a few millielectronvolts broad lines, and therefore being able to detect only a few electronvolt broad spectral ranges on a single spectroscopic image, the spectrometer setup turns out to be a bit of a constraint on the experiments in H_2. This is because the Q_n resonances manifest as ≈ 10 eV broad structures according to cross section studies, as already discussed in Sec. 1.2.3 and Sec. 4.1. Ordinarily, one would rather use a spectrometer, with a spectral range at least twice as broad as the width of a spectral signature, whereas for the experiments presented in the next section this was not the case: the spectral range, recorded simultaneously was just about as broad as the detected structures themselves. To enlarge the accessible spectroscopic region, one could possibly bring the CCD camera chip closer to the VLS grating at the cost of spectral resolution. Such a substantial modification of the experimental setup was however omitted, since other experiments were planned to be carried out in between runs of the studies that are presented here.

NIR Intensity Limitations:

The reliable NIR intensity control using the piezo-controlled iris aperture, Sec. 2.2.1, is an essential part of the experimental setup. Unfortunately, for the highest intensities, i.e. a widely open iris, XUV radiation from HHG processes in the target medium H_2 itself was encountered for adjusted overall backing pressure around 100 mbar in the target cell. To exclude such nonlinear effects, one could have used less pressure, which was considered of a disadvantage when detecting small changes in absorption signals. Therefore, we ended up being limited in the NIR intensity, so that at the end small iris openings, thus letting moderate NIR intensities on the order of 1 to 10 TW/cm^2 were employed in the transient absorption studies of the DES dynamics in hydrogen. To this point, no conversion between iris opening set value is done for the new laser setup, which is why in the following the NIR intensity is referenced with the iris set value, where 71 is the one for close aperture, i.e. no NIR light, and 0 the value for the widest iris opening. The region, where no HHG light in H_2 was detected and where the experiments in H_2 were carried out is between iris set values from 61 to 68. How the produced high-order harmonics of the NIR laser pulse in H_2 in the target cell look like for different iris openings is

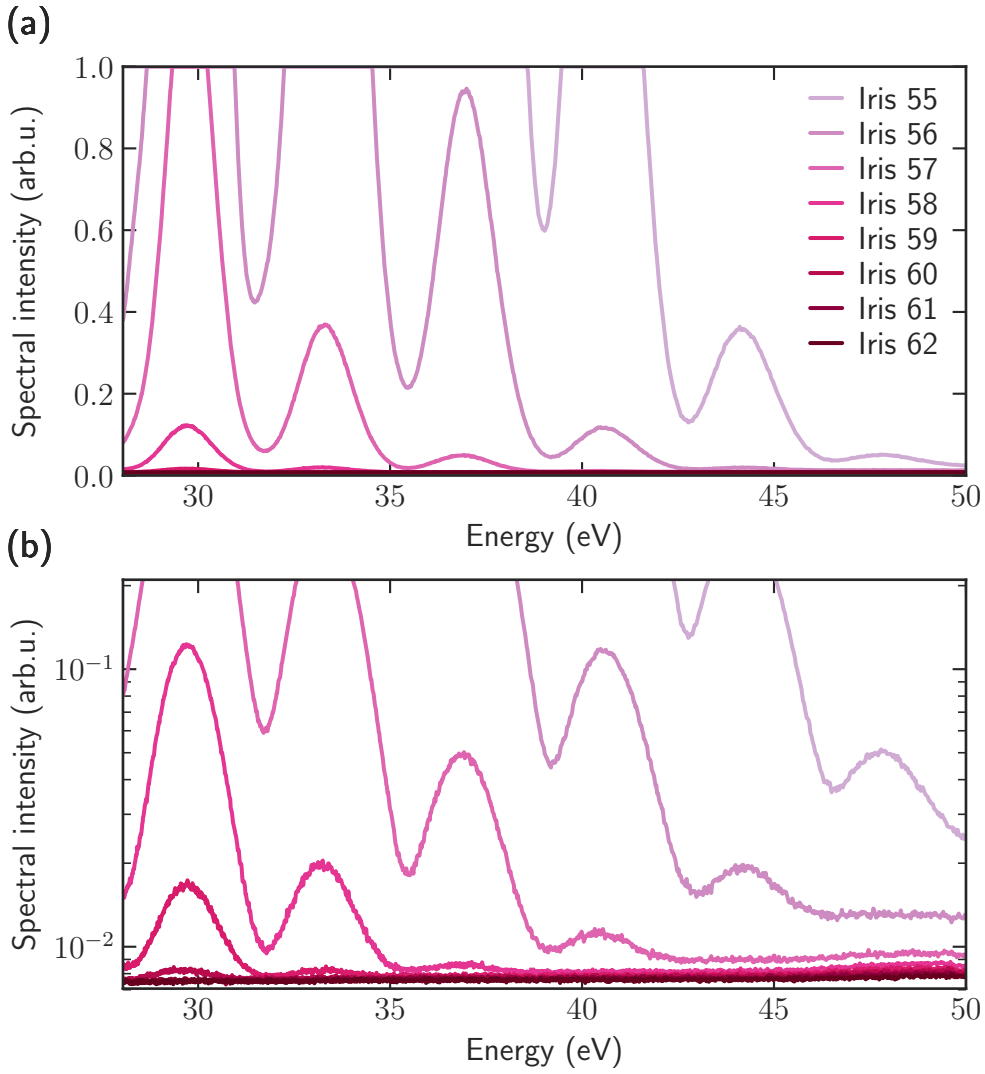

Figure 4.5: XUV radiation generated in an HHG process in the target cell, filled with H_2 **(a)** and **(b)** show XUV spectra of light generated in the target cell (NIR driving pulse and H_2 as HHG conversion medium) on a linear and logarithmic scale, respectively. The iris set values 62 to 55 (legend in **(a)**, applying also to the data in **(b)**) correspond to increasing NIR pulse intensities, as discussed in Sec. 4.2.4. The conditions for recording the data shown in the figure and the experimental data in Sec. 4.3 are similar: NIR pulse length less than 5 fs, H_2 target pressure $\approx$ 100 mbar, target cell in the focus of the NIR beam, energy range between 28 and 50 eV, 1000 ms exposure time. Spectra are recorded for NIR only in the target cell, without any XUV light generated in argon upstream. The data is normalized according to the maximal count value from the recorded raw data spectra. XUV spectra for iris set values smaller than 57 already oversaturate the CCD detector for the set exposure time.

shown in Fig. 4.5. Knowing that the experiments in H_2 are carried out at NIR intensities just under the HHG threshold in the molecule, meaning that considerable non-linear ionization in H_2 is present, will become important later, when discussing the experimental results, giving an insight into different ionization channels.

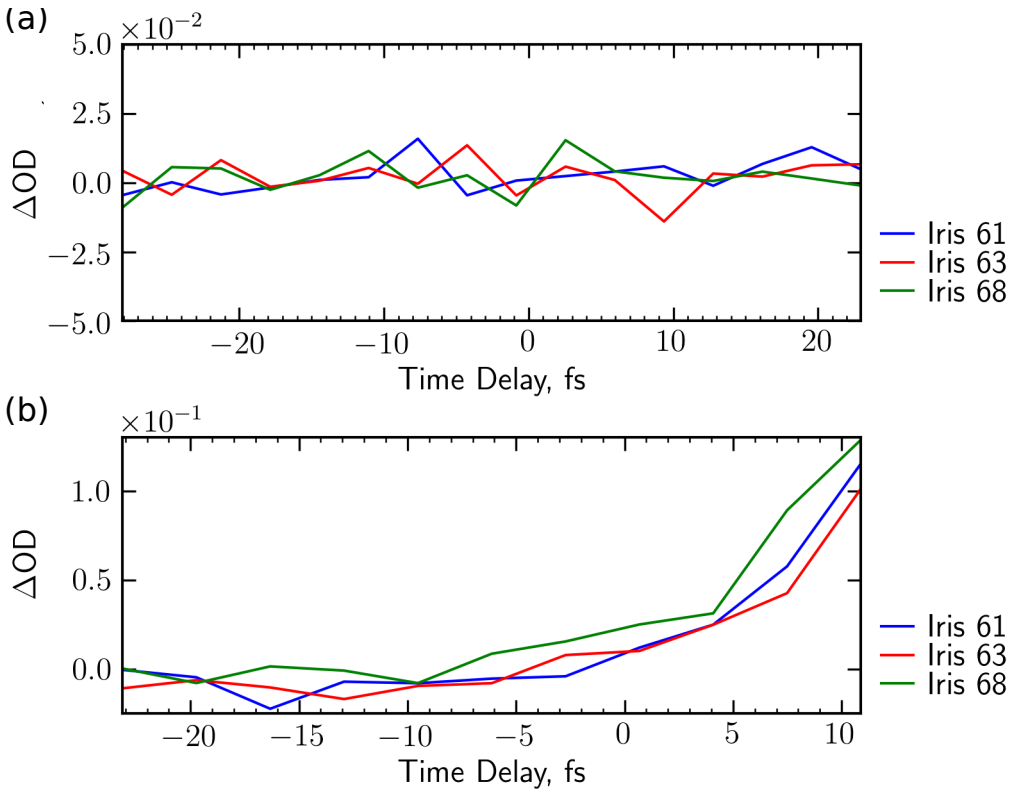

Figure 4.6: HHG Background measurement to account for geometrical effects from the target cell

(a) and **(b)** Measurement of the XUV-signal change without target gas in two cases: without and with a target cell in the focus position of the target chamber. Three iris openings – 61, 63 and 65 – are considered in both cases. Since the measured background value is the same for all three iris openings, no clipping on the iris aperture is present.

Sensitivity of the Experimental Apparatus

In Cha. 2.2 we already discussed briefly the influence of the walk-off effect, arising in the split and delay mirror setup. It was pointed out that for a time delay range of ≈ 50 fs the foci of both the NIR and XUV pulses still overlap, making the walk-off effect not particularly important, when looking at sharp resonances. In the studies of superexcited Q_n states in the hydrogen molecule the time-dependent absorption is influenced by the walk-off, and this effect turned out to be significant compared to the measured time-dependent changes in H_2.

Cell Tracking: To correct for the the walk-off effect, a so-called cell-tracking procedure was introduced after the first time-dependent ΔOD-measurements in the range between 30 and 50 eV. There, in a TD lineout, changes in the absorption signal, over the whole considered energy range, were encountered, with an almost linear effect with an oscillation of ΔOD on the order of 10^{-1} OD units around the zero ΔOD offset. To check whether the measured signature was a real time-dependent change in the absorption, the same measurement was done without a target gas, thus only detecting the XUV-signal change in two cases: with and without a target

cell in the focus position of the target chamber, Fig. 4.6 (a) and (b), respectively. In the first case, Fig. 4.6 (a), where the XUV signal is detected scanning the time-delay between the NIR and XUV pulses, basically the stability of the XUV light was measured. The result of this measurement is a flat curve around $\Delta OD = 0$ for all three considered iris openings. In other words, a background value for the XUV fluctuations due to changes in the CEP of the NIR pulse, pressure instabilities of the conversion medium in the HHG generation region and other possible effects was measured. On the other hand, when the XUV beam enters the target cell, as shown in Fig. 4.6 (b), an increase in the measured signal with increasing time-delay was observed. The overall ΔOD signal change is less than 10^{-1} OD units, but still significant for the time-dependent signals we aimed to detect in H_2, which would, according to synchrotron cross section data, change on a scale at least an order of magnitude smaller, Sec. 1.2.3. To correct for this geometrical effect, possibly arising because of a slight clipping of XUV stray light (shadow effect) on the target cell opening, the cell tracking procedure was brought in. It corrects the transversal position of the target cell with respect to the beam path, thus letting the whole XUV light beam pass through the middle of the cell opening without clipping, in similar stray-light geometry on the opening edges for each time delay adjustment. To map a time delay value, i.e. the piezo position of the inner mirror, to the transversal position of the cell stage, the following procedure was employed directly before a measurement and the resulting tracking curve was used in the measurement routine. The algorithm to obtain the cell-tracking curve includes:

- Deciding on the time delay range to scan for an experiment: usually between piezo values 85 and 115 µm, i.e. time delays in the range from −30 to 20 fs.

- For both positive and negative transverse directions, finding the cell position values, where at a fixed time delay position only 10% of the XUV light is still detected in the spectrometer.

- Calculating the mean transversal position values for all fixed time delay positions of the previous point.

- Fitting a linear curve to the data.

The fitted linear curve allows then to adjust the transversal cell position for every piezo value of the inner mirror movement. From the slope value of the fitted to the data curves in Fig. 4.7, slope for each data set given in the legend, the correction value for time delay change $\Delta\tau = 1$ fs corresponding to cell position change by $\Delta w_{\text{cell}} = (1.0 \pm 0.1)$ µm is calculated. This value agrees with the theoretically calculated walk-off value, where for $\Delta\tau = 1$ fs a transverse beam displacement $\Delta w = 1.13$ µm is encountered, Sec. 2.2.4. The cell-tracking procedure, included in a measurement routine, then allows for keeping the XUV light flux through the target cell on the approximately same value for the whole accessible time-delay range.

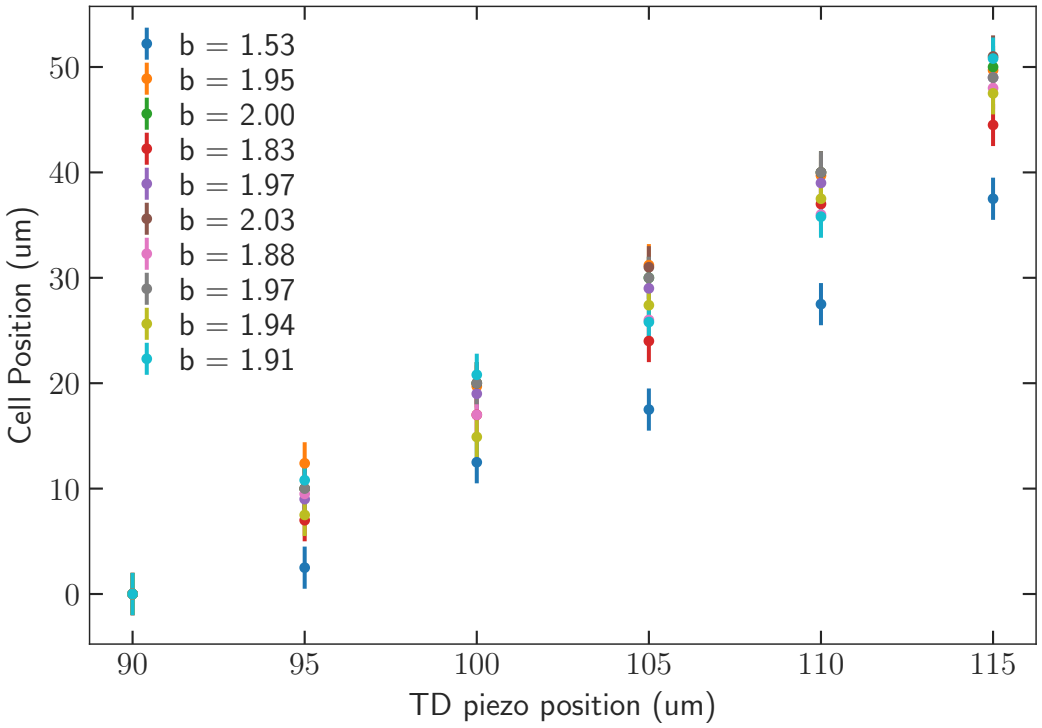

Figure 4.7: Mapping of the TD-piezo position to a target cell position
Data obtained according to the described procedure for obtaining the cell-tracking curve. To the data of each experimental run (denoted by the different colors), a linear curve $bx + a$ was fit. Fit values for the slope parameter b is shown in the legend. um stands for µm.

Energy Shift: Another effect to consider, arising again because of the XUV beam walk-off, is an energy shift of measured spectral data with change in time delay. This shift is approximately linear, taking into account the linear walk-off (≈ 1 µm) and the rotation of the XUV light beam with respect to the grating normal by (≈ 3 µrad) for a TD change $\Delta\tau = 1$ fs. This is a known effect, corrected for also in previous studies of sharp resonances. Looking at broad spectral features, however, one could think that this effect would hardly be of importance, which turned out not to be true, when aiming at sensitivity less than 10^{-2} OD units. To illustrate this effect and demonstrate that it could be rather easily corrected for, Fig. 4.8 is shown. There, two cosine functions, differing only in a phase shift of around 50 mrad are plotted. The ratio between offset and peak-to-peak amplitude of the cosine modulation is set according to typical harmonic modulations of the XUV reference spectra. Calculating the $\Delta\mathrm{OD} = -\log(\frac{S(\phi=2\pi/100)}{S(\phi=0)})$ yields a value on the order of $\Delta\mathrm{OD} \sim 0.5\,10^{-2}$ and modulating with energy. To correct for such a ΔOD signature, which is not due to a change in a cross section neither to a change in the target density, the energy axis for the cosine curve with phase offset $\phi = 2\pi/100$ is shifted back to the reference curve with $\phi = 0$, transparent green line in Fig. 4.8 (a). The calculated value for the ΔOD from the curve shifted back to the reference curve is, as expected, zero for all energies, Fig. 4.8 (b).

To find out how much the harmonics signatures of the XUV spectrum should be shifted in energy, when scanning the TD, the sharp resonant lines of DESs in helium were evaluated and

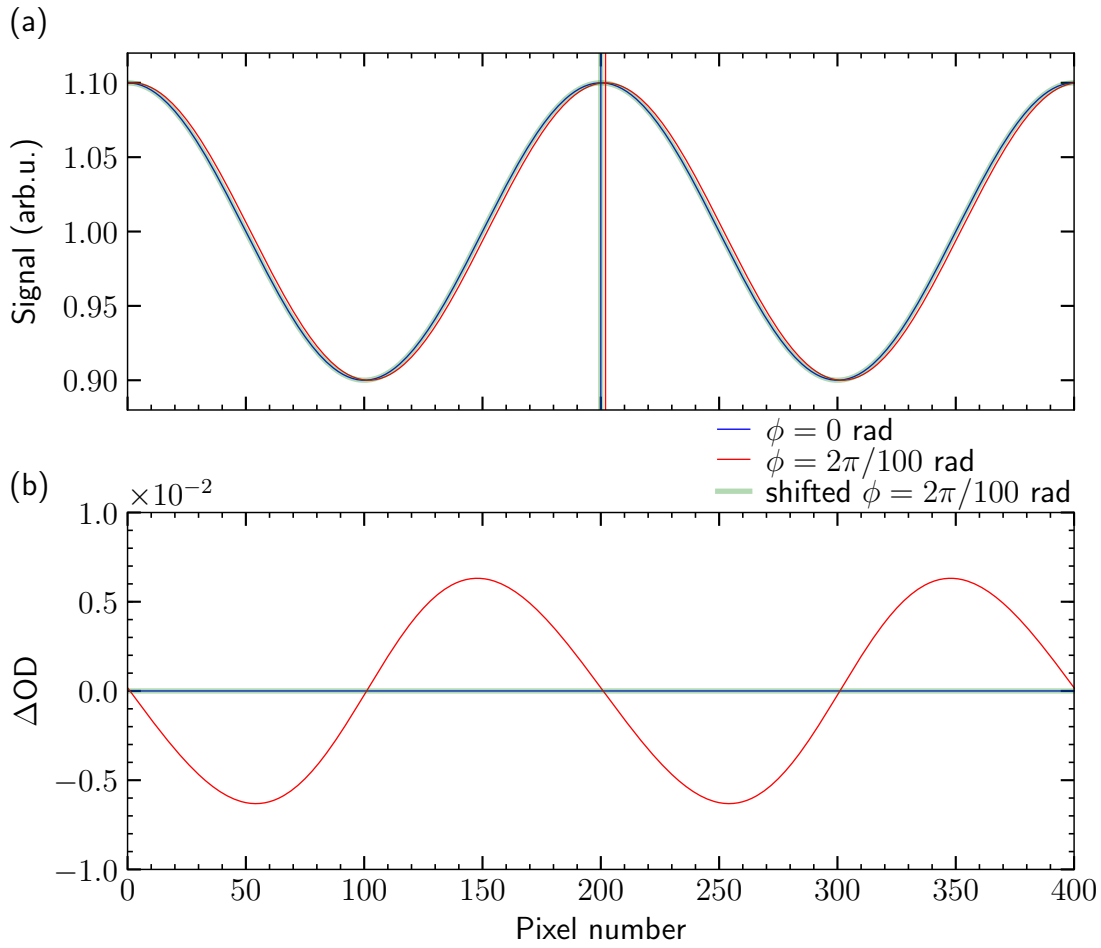

Figure 4.8: Effect of the energy shift on the calculation of ΔOD
(a) Two cosine functions with a phase shift against each other of $2\pi/100$ rad. The vertical lines in the plot mark the position of a maximum value of both curves. The ratio between offset and peak-to-peak amplitude of the cosine modulation is set according to the one in the XUV reference spectra. Note the magnified vertical scale, excluding zero signal strength. The curve with phase different than zero is shifted back to the reference curve, green line. **(b)** ΔOD value at each pixel position for three case, where the signal of the cosine wave with $\phi = 0$ (blue line), the signal of the cosine with $\phi = 2\pi/100$ (red line) and the signal of the back-shifted red line to the blue one is always referenced to the blue line for the ΔOD calculation.

shifted linearly in such a way that the resonances remain at the same energy for all TD values in the TD-Scan. The required shift is 0.3 μeV for a change in TD $\Delta\tau = 1$ fs, or 13 meV for a change in TD $\Delta\tau = 42.8$ fs. The back-shifting of the resonant helium lines is shown in Fig. 4.9.

Overall Sensitivity

Taking all relevant corrections listed above, a TD-ΔOD-Scan without a target gas and with proper statistics – to be able to measure changes in ΔOD on the order of less than 10^{-2} OD units – was carried out to quantify the instrumental sensitivity. The data for two iris set values, almost maximal and minimal opening accessible in the context of the NIR-intensity limitations,

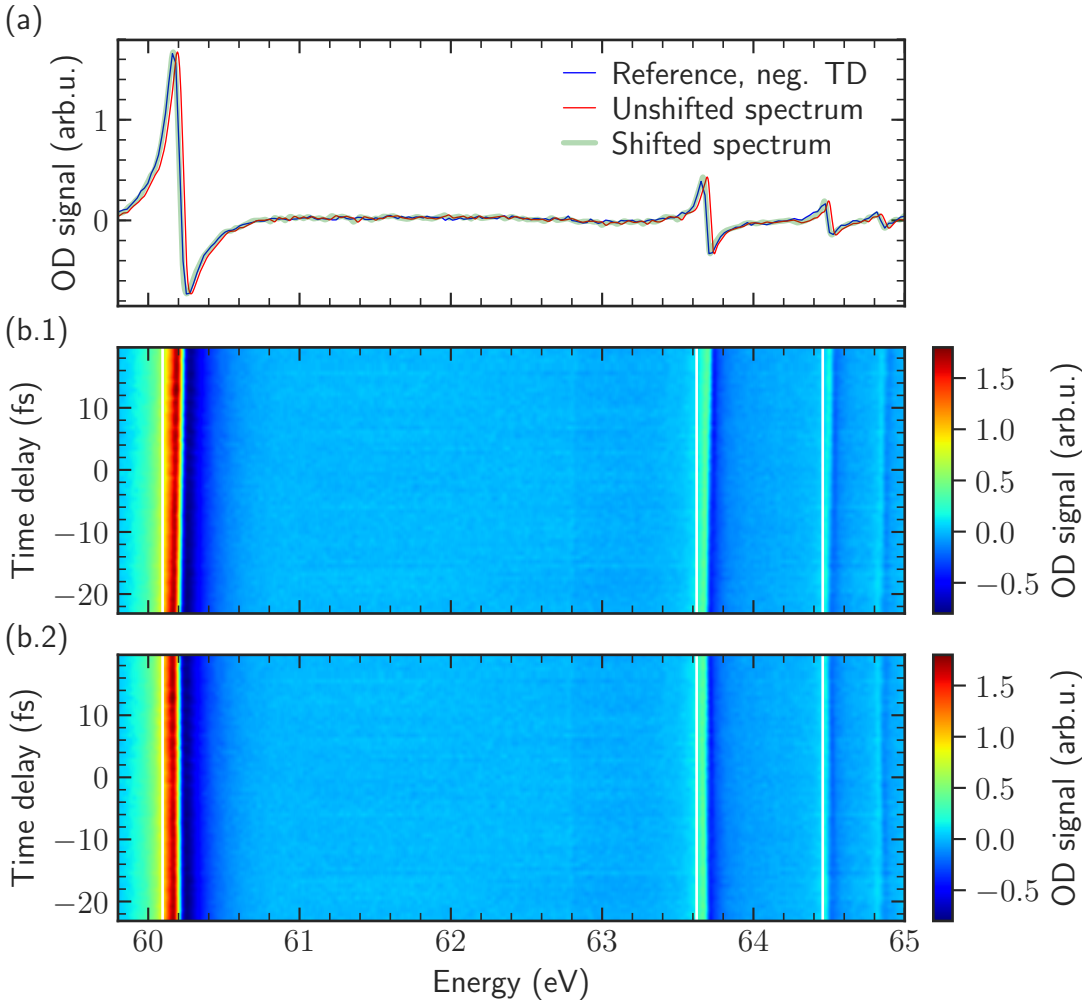

Figure 4.9: Procedure of energy shifting for walk-off correction, applied to helium data Absorption spectra of the DES resonances in helium were evaluated by the Fourier-transform method, as described in [2], and shifted linearly in such a way that the resonances remain at the same energy for all TD values in the TD-Scan. The blue curve in **(a)** is the OD signal recorded for the most negative time delay in **(b.1)**, and the red curve is the one for the most positive delay value in the considered TD range in **(b.1)**. The green line is the red line shifted back in energy so that the resonances remain at the same energy for both time-delays. All three white vertical lines around the first three resonances in **(b.1)** and **(b.2)** should serve as a guide to the eye to notice the difference between the TD-Scan without correction for the energy shift, **(b.1)**, and with correction, **(b.2)**. In the latter case the resonant lines remain at the same energy position for all time delays. Data recorded with NIR light being absent.

addressed above, evaluated without and with the energy-shift correction, is shown in Fig. 4.10 and Fig. 4.11 for the iris values 63 and 68, respectively. In both Figs, (a) shows the raw data, as directly measured, (b) the ΔOD-Scans after correcting for the spectrometer energy shift and (c) the data evaluated with a notch filter (NF), removing the remaining harmonics modulation in (b). Comparing (a) and (b) in both Figs 4.10 and 4.11 it becomes apparent that the remaining harmonics modulation cannot be corrected for entirely by means of the energy backshifting

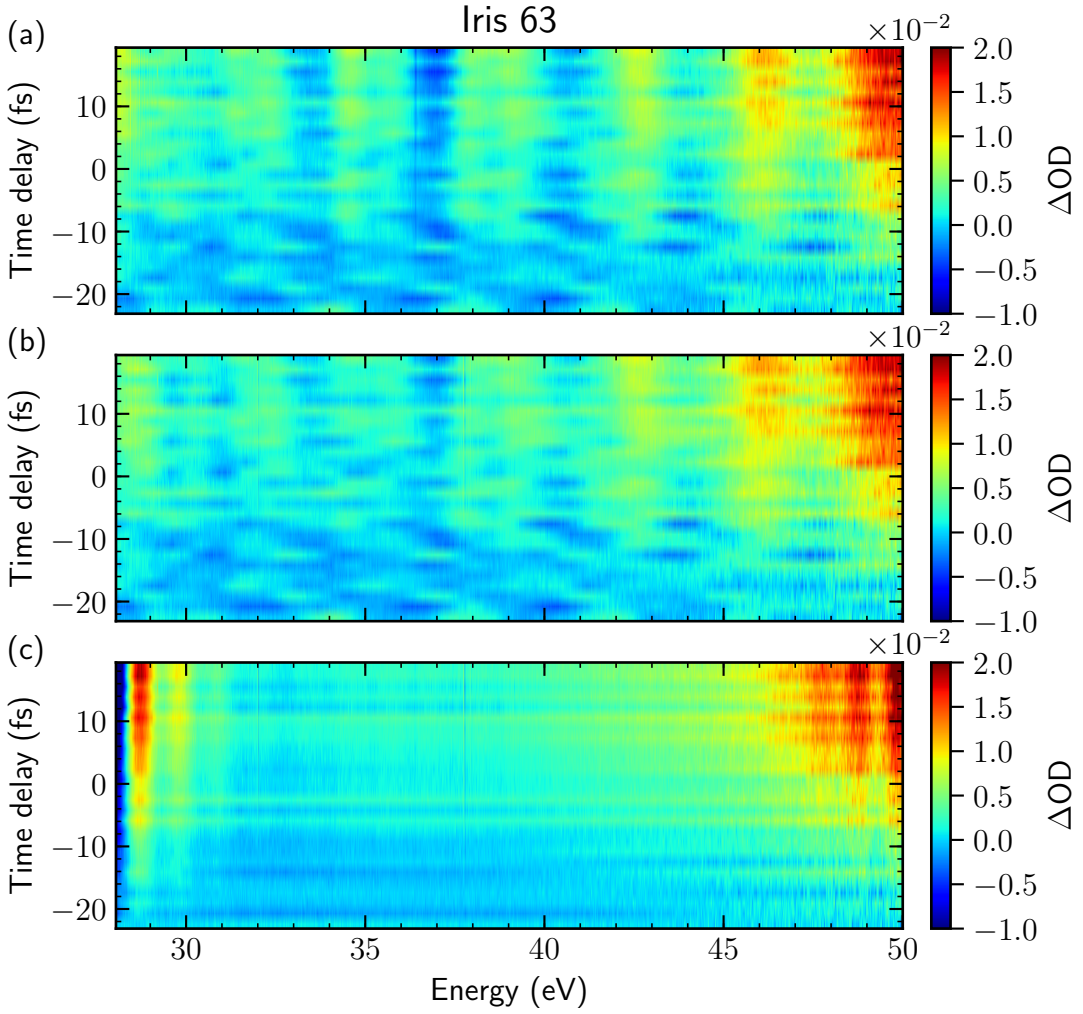

Figure 4.10: Measurement of the background sensitivity, without any H_2 target gas, for ΔOD-TD-Scans at iris set value 63

(a) TD-Scan for iris 63, where the ΔOD values are obtained for the raw experimental data, corrected only for the walk-off effect by the cell-tracking routine, directly included in the experimental sequence. The line around 36.4 eV is aluminium filter absorption cutoff in the second order. Correcting for the slight energy shift with time delay, **(b)**, the aluminium absorption edge is not seen any more, since it attenuated the XUV light by the same amount and therefore should not be seen in correctly evaluated ΔOD data. The line around 37 eV in **(b)** and **(c)** is due to dead camera pixels, since it is at the same pixel value for all TDs before correcting for the energy shift. **(c)** shows the data from **(b)** evaluated with a notch filter to remove the remaining harmonics modulation and making the overall change of the ΔOD signal with time delay more clearly visible.

routine, unfortunately. Therefore, there should be also another effect, not considered in the data evaluation so far, leading to the increase in measured ΔOD background signal with time delay, which is seen even in the raw data, Figs 4.10 and 4.11 (a). Taking a lineout over the whole energy region, see Fig. 4.12, an overall linear increase in the extracted ΔOD values is encountered, when evaluating the data from Figs 4.10 and 4.11 (b) and (c), corrected for the

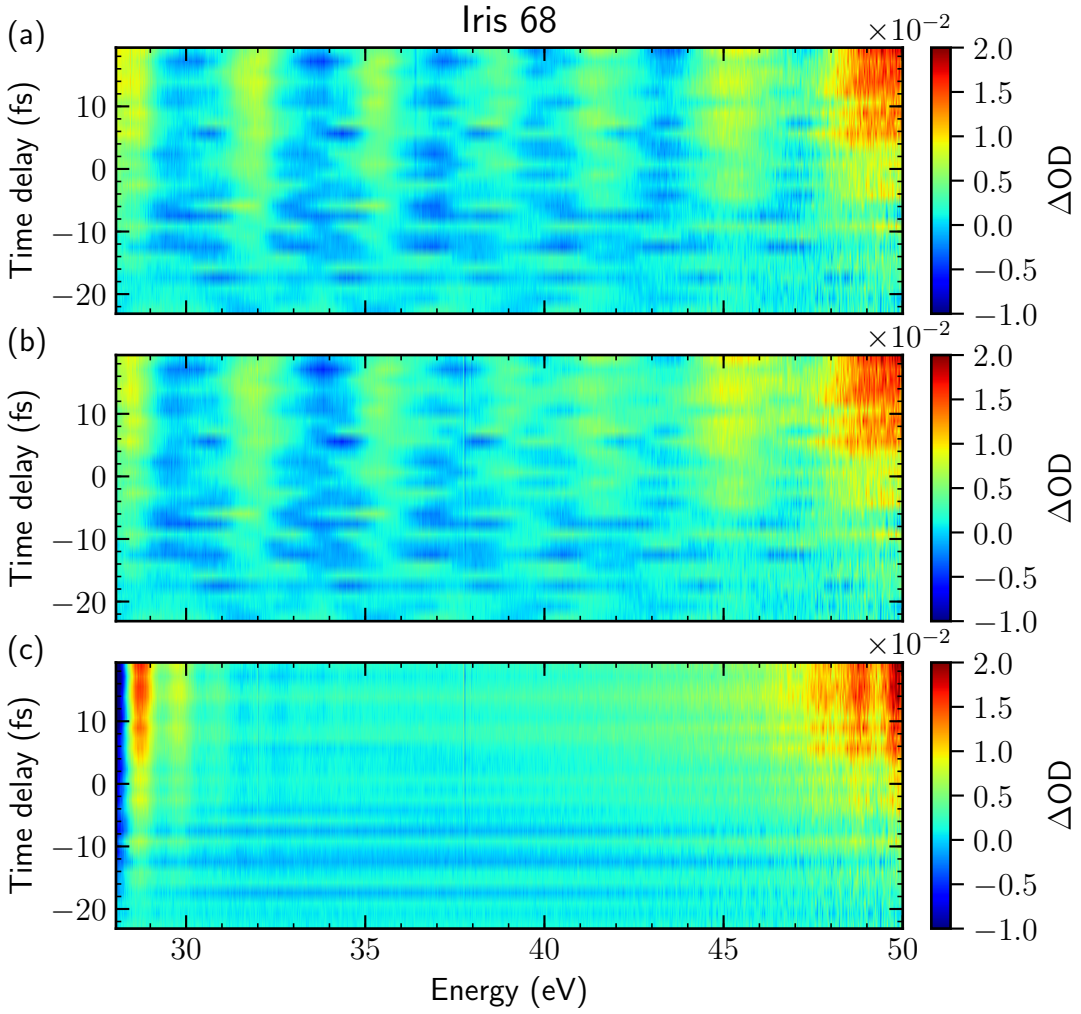

Figure 4.11: Measurement of the background sensitivity, without any H_2 target gas, for ΔOD-TD-Scans at iris set value 68

Background sensitivity for a measurement for iris 68. **(a)**, **(b)** and **(c)**, same as Fig. 4.10 show a ΔOD-TD-Scan obtained for the raw experimental data, after correcting for the slight energy shift with time delay and the notch-filtered data from Scan **(b)**, respectively.

energy shift and for the remaining harmonics modulation by using a notch filter, respectively. The linearly increasing signature, which perfectly should have been a constant zero for all time delays, shows that there are still other setup problems limiting the sensitivity to a noise level around 5×10^{-3} OD units. What is also apparent from the measured data is that such an increase with time delay is not the same for all energies, Figs 4.10 and 4.11. It is of a relatively high value for high photon energies but not as strong for photon energies smaller than 40 eV. Furthermore, the region, where the biggest changes are observed is the one, where the XUV light signal is of the lowest intensity, Fig. 4.2 (b), so that a small change in the spectra could mean a bigger change in the ΔOD value. On the other hand, the regions where the energy shifting procedure can compensate for the remaining harmonics modulation almost entirely is the one where the energy calibration lines have been detected, located below 36 eV in the first spectrometer order.

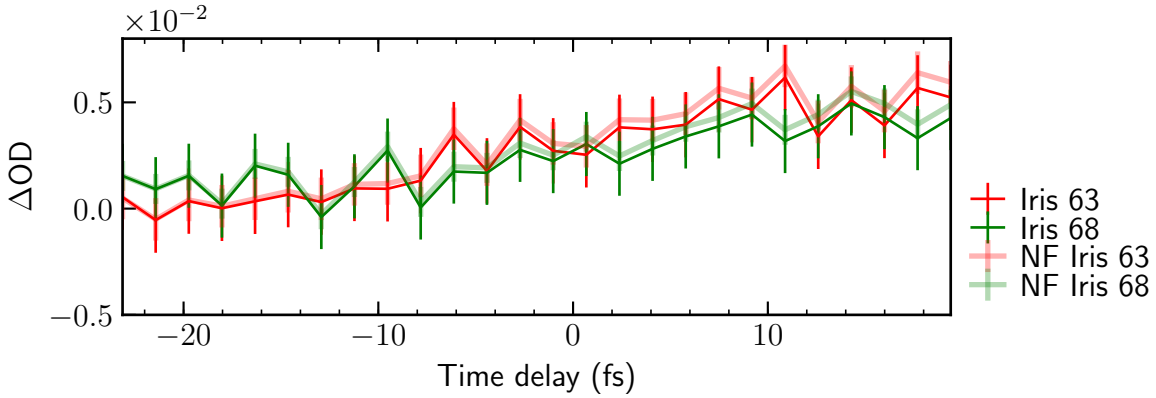

Figure 4.12: Time-delay lineouts from measuring the background sensitivity, without any H_2 target gas, at iris set values 63 and 68

The ΔOD signal in almost the whole detected energy range, between 29 and 49.5 eV for each TD value is summed up and normalized to the length of the energy range to obtain a lineout of the spectra in Figs 4.10 and 4.11 (b) and (c). The obtained curves show the same linear change with time delay, within the error bars. For obtaining the TD lineouts over the whole energy range it seems to does not make a difference whether the data before or after using a notch filter (NF) is used. The linear increase in measured signal points towards another systematic effect in the measurement or evaluation procedure, which is so far not accounted for.

This brings us back to the issue, which always arises when calibrating spectra with known values only in one part of the spectra, giving rise to errors in the energy calibration routine. Nonetheless, with a sensitivity like the one demonstrated, changes in absorption signals of comparable or larger value can be detected so that the required sensitivity for detection of time-dependent absorption changes of the Q_n resonances in molecular hydrogen is achieved.

4.3 Measurements and Results

In this section all main results of the measurements in molecular hydrogen as a target gas are presented. After carefully considering all effects discussed in the previous section, and especially becoming sensible to the magnitude of the corrections in the process of data evaluation, the results of the experiments, aiming to detect absorption changes in the ionization continuum of H_2 during the autoionization lifetime of the doubly excited Q_n resonances, are summarized. First, static absorption spectra are shown, to demonstrate that an absorption signal is detected at all in the energy range around 30-35 eV, where the Q_n resonances exhibit maximal absorption cross sections. Later, we focused on measuring transient data, thus recording TD-Scans for different iris values. The changes in the detection of the absorption signals are discussed at the end of the section.

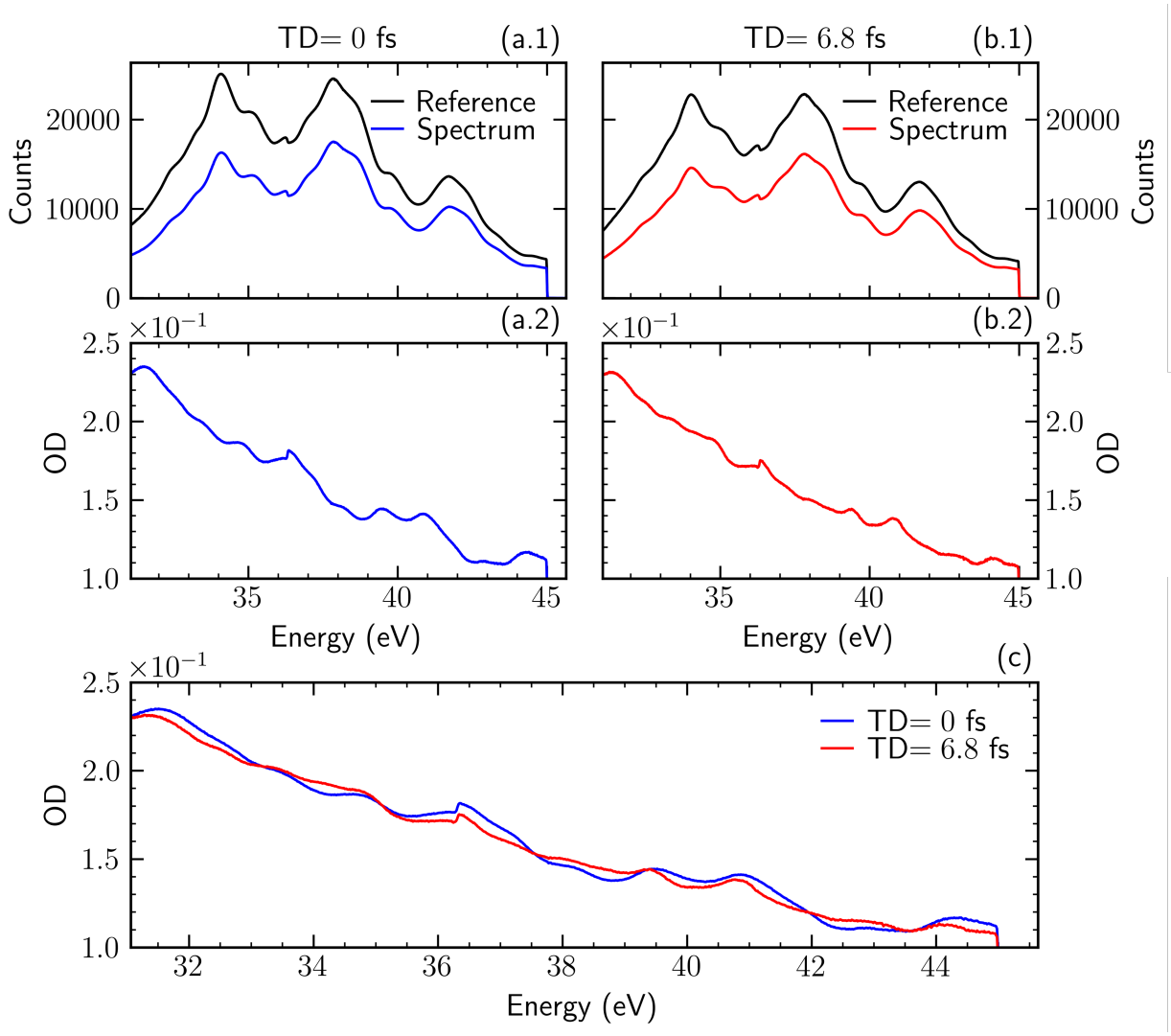

Figure 4.13: Static absorption signals in the hydrogen molecule for 0 fs and 6.8 fs time delay **(a)** and **(b)** Data for signals detected at time delay of 0 fs and 6.8 fs, respectively. **(a.1)** and **(b.1)** Raw data, with reference curve being the detected XUV reference signal, i.e. without target gas absorbing the XUV radiation. **(a.2)** and **(b.2)** Calculation of OD signal from data shown in **(a.1)** and **(b.1)**. **(c)** Comparison between the OD absorption signals measured at 0 fs and 6.8 fs time delay. Energy range between 30 and 45 eV.

4.3.1 Static Absorption Spectra

Absorption signals in the ionization continuum are difficult to detect. Therefore it could be especially complicated to detect changes in such continuum absorption signatures. For this reason, before doing any measurements to detect transient absorption, i.e. time-dependent signals, we first looked at the static absorption signals in the energy range between 30 and 45 eV where absorption from the Q_n doubly excited resonances in H_2 is expected to occur, Fig. 4.13. After evaluating the raw data, Fig. 4.13 (a.1) and (b.1), by means of calculating absorption OD signals, as in Eq. (1.13), Fig. 4.13 (a.2) and (b.2), we are definitely able to measure absorption in the ionization continuum of H_2. However, in the overall absorption signals, as shown in Fig.

4.13, both the continuum absorption of the first ionization threshold in H_2 as well as absorption from the Q_n resonances is detected simultaneously. On top of this, also geometrical effects from the target cell attenuate the measured signals. To detect changes in the absorption by the Q_n resonances only and look, for example, at the autoionization time dynamics of the Q_n states, direct ΔOD signals, for changes in the absorption data for different time delays is calculated, as in Eq. (4.1). The results of the time-dependent absorption experiments is discussed in the next section. Note, that in the data analysis the energy shift arising from the walk-off, discussed in the previous section, is not taken into account in the data evaluation. The reason for this is that the effect was considered at a very late stage and will be included in future data evaluation but not for the results presented in this thesis.

Apart from measuring time-dependent OD signals, in the beamline, where the experiments discussed here were carried out, different NIR intensities can be easily adjusted, Sec. 2.2.1. In the time-dependent absorption signal measurements we make use of the possibility to use different NIR intensities, since the autoionization dynamics of the Q_n resonance, just as the autoionization in helium or argon, 4.2.3, should be NIR-intensity-dependent. Therefore, before measuring time-dependent delta OD signals, we obtained data for determining ΔOD at three different NIR intensity values, but for a fixed time delay, Fig. 4.14, where (a.1), (b.1) and (c.1) show the raw data, (a.2), (b.2) and (c.2) the calculated ΔOD signals, and (a.3), (b.3) and (c.3) the data after evaluation with a notch filter. It should be noted that the spectra for the different iris settings were recorded after one another, measuring for $\approx$ 20 min with fixed iris. Therefore, the systematic drift of the incoming XUV spectra, as seen in the raw data, can be explained. Nevertheless, a change in OD is observed, which calls for a more careful investigation. To further examine the intensity dependence of the ΔOD signal, as measured in Fig. 4.14 for a fixed TD value, time-delay scans for a range of NIR intensities between iris set values 60 and 70 were measured, the results of which are discussed in the following.

4.3.2 Detection of Time-Dependent Absorption Signals

In this section, the experimental data from measuring changes in absorption, i.e. ΔOD signals, in a TD range between ≈ -20 fs and $\approx$ 20 fs (exact TD range dependent on the experimental run) and for different NIR intensities, is presented and discussed. The backing pressure for all data shown in the following is around 100 mbar, thus the usable iris set values are limited between 60 and 70.

We first performed a TD-Scan for two iris set values, 61 and 63, with data shown in Fig. 4.15 (a) and (b), respectively. For both iris apertures change in the ΔOD signal, i.e. change in the absorption, for the whole energy range between 28 and 47 eV was detected. Since this is the energy region where we expected to see absorption signal modifications due to the autoionization of the Q_n resonances, subsequent measurements with finer time delay steps than $\approx$ 3.4 fs, corresponding to 2 µm steps of the piezo movement of the inner mirror (settings for the data

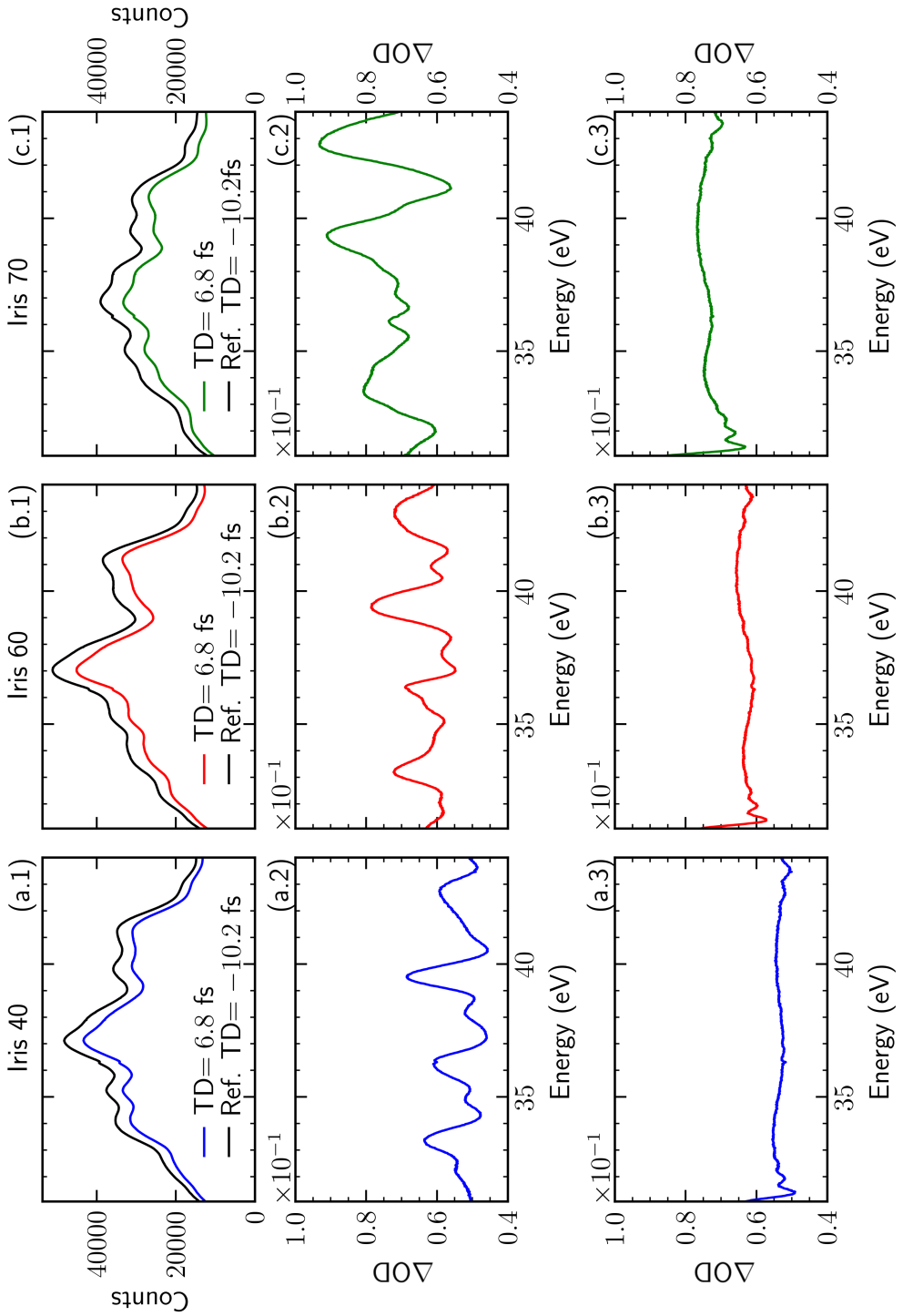

Figure 4.14: NIR-intensity-dependent measurment of ΔOD signals at a fixed TD of 6.8 fs **(a.1)**, **(b.1)** and **(c.1)** show the raw data, **(a.2)**, **(b.2)** and **(c.2)** the calculated ΔOD signals, and **(a.3)**, **(b.3)** and **(c.3)** the data after evaluation with a notch filter for iris set values of 40, 60 and 70, respectively. Note here, iris 40 was accessible, i.e. no HHG in hydrogen was detected, because the H_2 backing pressure, adjusted in this experimental run was only ≈ 40 mbar and therefore the HHG conversion efficiency in H_2 is not sufficient to produce XUV radiation.

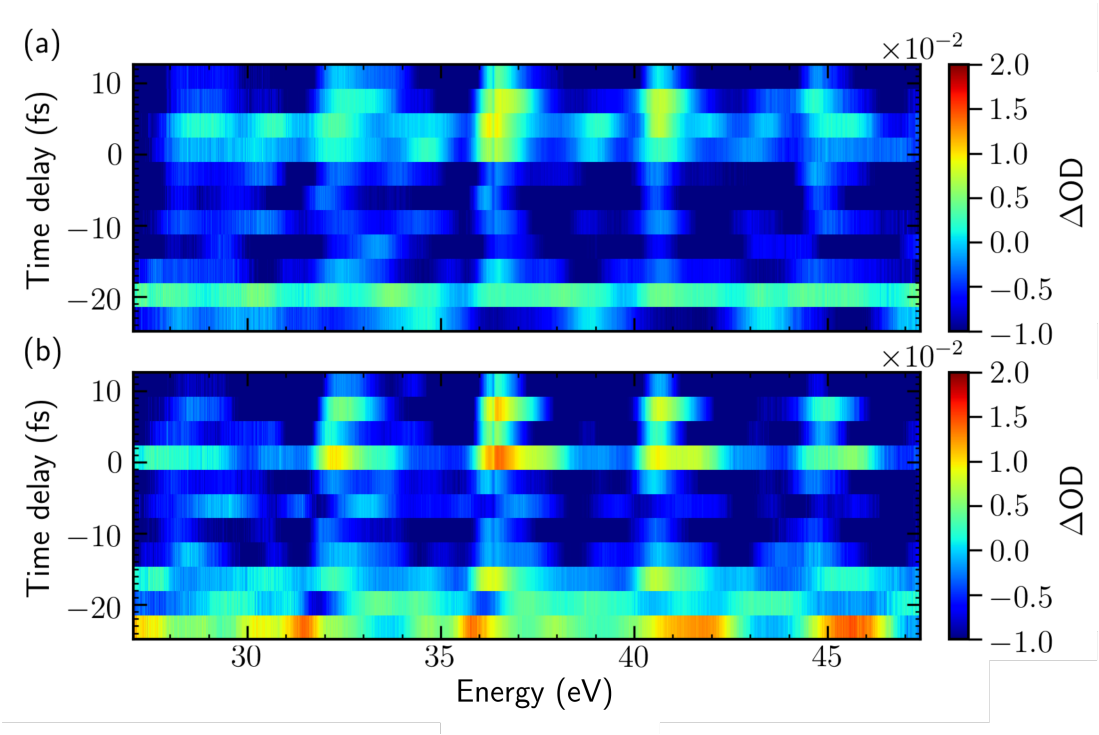

Figure 4.15: NIR-intensity-dependent TD-Scans in H_2
(a) and **(b)** TD-Scan for iris set values 61 and 63, respectively. TD steps of ≈ 3.4 fs, corresponding to 2 µm piezo steps of the inner mirror.

in Fig. 4.15), were carried out. The time delay step size was then set to ≈ 0.4 fs, so that even an NIR laser cycle can be resolved[1]. In the first measurement run, however, only the maximal possible iris opening was used, since the most prominent changes in the absorption signal are expected for the highest NIR intensities. To obtain the raw data, shown in Fig. 4.16 (a), averaged over 600 TD-Scans, the overall measurement time was around 14 hours with exposure time of 1000 ms. The data analyzed with the notch filter procedure, to exclude the effect of the harmonics modulation and obtain the energy dependent offset of the ΔOD signal, Fig. 4.16 (b), is summed over for the whole energy region between 29 and 49.5 eV for the TD lineout in Fig. 4.16 (c). An increase in the ΔOD signal is detected, which sets on at around zero TD. For time delays smaller than zero, i.e. NIR pulse coming before the XUV light pulse, the ΔOD is close to constant in value, oscillating around zero. The overall change over the whole region is on the order of 1.0×10^{-2}ΔOD units, which is on the same order of magnitude as the background systematic change of 0.5×10^{-2}ΔOD units, Fig. 4.12. However, even considering the uncertainty in the measurement, still a bigger change in the ΔOD value in the measured data, compared to the background data, is present.

To investigate the absorption changes in H_2 in the energy region of the highest absorption cross section of the Q_n resonances, in its time- and NIR-intensity dependence, a measurement, with similar settings as the one for iris 61, Fig. 4.16, was carried out. The TD region was

[1]For carrier frequency of ≈ 1.63 eV, wave length of 760 nm, one oscillation cycle has a duration of ≈ 2.54 fs.

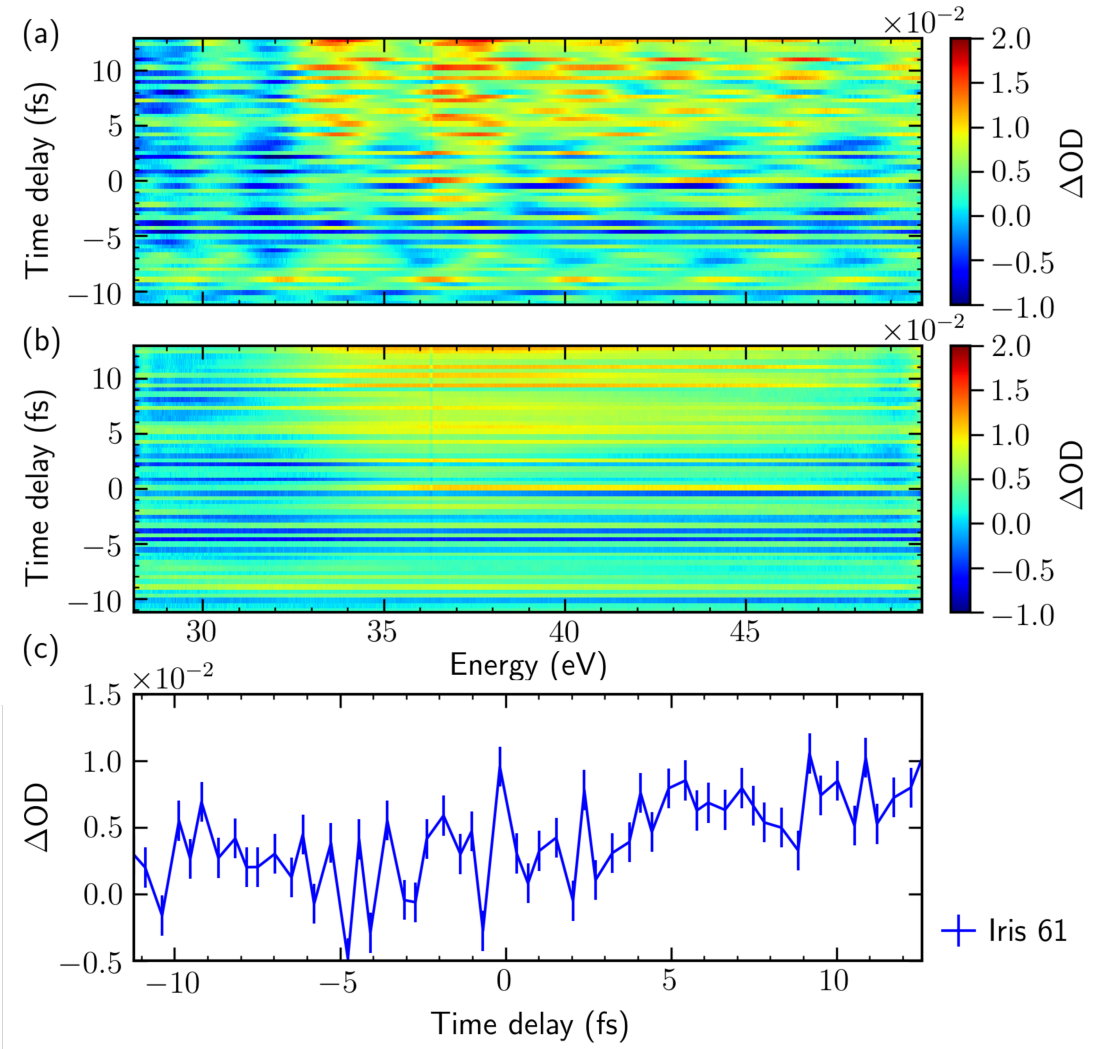

Figure 4.16: TD-Scans in hydrogen for maximal NIR intensity
(a) Raw data averaged over 600 TD-Scans with exposure time for one spectrum at a fixed time delay of 1000 ms. **(b)** Data analyzed with the notch filter procedure. **(c)** TD lineout over the energy region between 29 and 49.5 eV obtained from the notch-filtered data. H_2 backing pressure around 100 mbar.

doubled in length, thus extending between −20 and 20 fs, with TD steps of 0.2 µm ≡ 0.34 fs (iris 61) or 0.4 ≡ 0.68 fs (iris 63, 68), depending on the iris set value. The data recording time for the set of all data, when doing 600 TD-Scans for obtaining statistics, added up to almost 90 hours. The stability of the laser system and the pressure fluctuations can be followed in Fig. 4.17. On the measurement days, marked with a green vertical line in the pressure diagram, the H_2 pressure needed readjustment. The pause in the experimental run was used for slight realignment and to control the NIR pulse characteristics by means of the D-Scan technique. In between the CEP laser stability, or sometimes also the pressure needed slight realignment (green dotted lines in the pressure diagram). For the duration of the whole measurement, 11 days, the laser system was not turned off, realigned were only the incoupling in the CEP set, Fig. 2.1, and in the hollow-core fibre. The laser parameter thus remained almost constant with FWHM

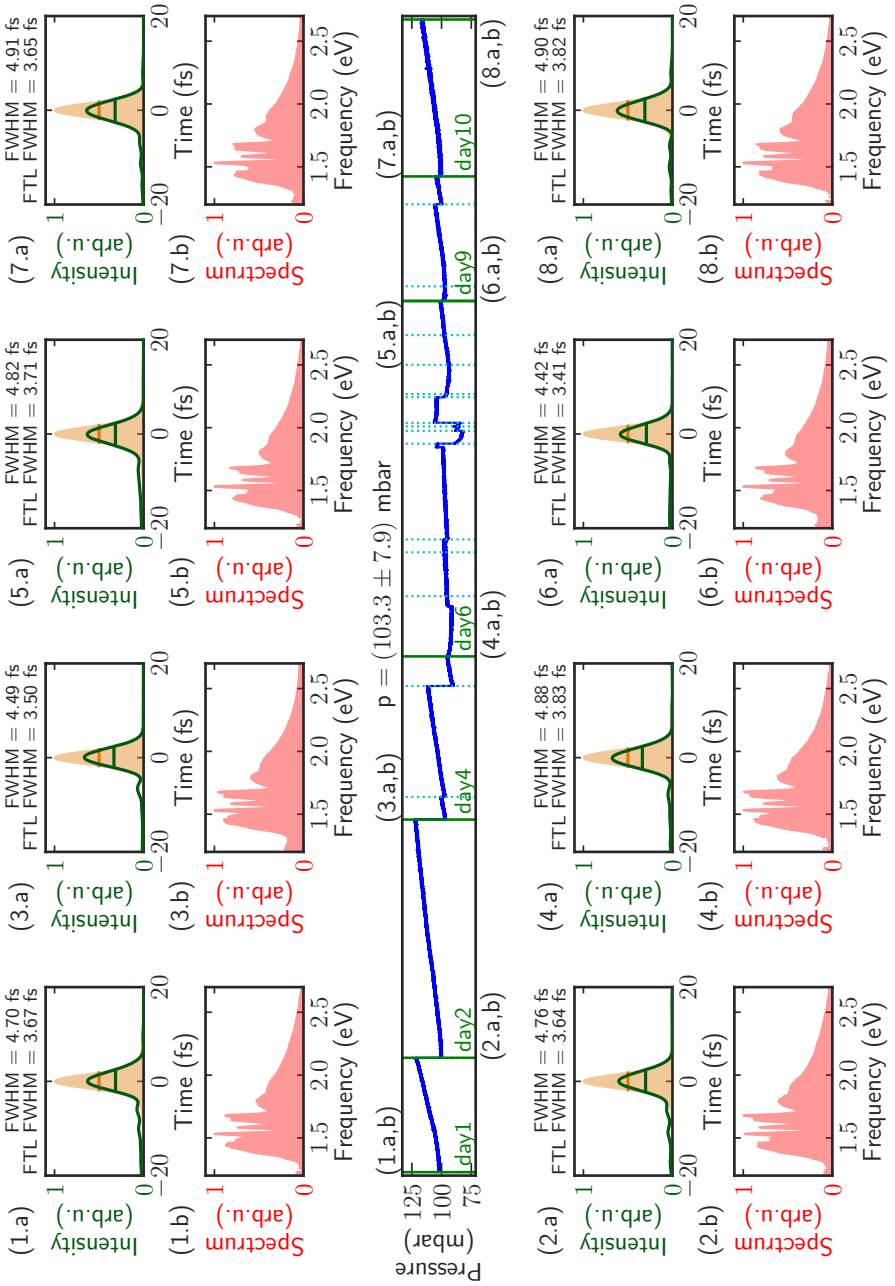

Figure 4.17: Longterm stability of the experimental parameters

H_2 pressure diagram (in the central part of the graph) over the whole measurement run for obtaining the TD-Scans for three iris set values: 61, 63 and 68. The average pressure value was determined to be $p = (103.3 \pm 7.9)$ mbar. The absorption data was corrected for the pressure change so that the TD-Scans for all three NIR intensity values can be directly compared. Green vertical lines in the pressure diagram show points in time where the data acquisition was paused to adjust the pressure and for slight laser realignment, as discussed in the main text. Parallel to this, D-Scan NIR-pulse characterization was performed (results inset). The vertical dotted lines in the pressure graph mark instances where the pressure or the alignment of the CEP set was readjusted, without changing anything else in the laser compression or beamline in-coupling. Each time the CEP set was readjusted, the wedges in front of the beamline were moved by less than 0.01 mm to obtain again isolated attosecond light pulses.

duration less than 5 fs and similar spectral profile during the whole measurement course. This experimental run is the first measurement of its kind in our research group, regarding duration and stability. It even reached the limits of the laser system capability to run without realignment, which became evident by the fact, that the output energy after the CPA compression stage, Sec. 2.1, has dropped slightly in intensity. This was measured in the power output: 9.0 W on day 1 and 8.85 W by the end of day 11. The spectral output, however, was only slightly less intensive and it was not observed that the effect changed the pulse length, energy and spectrum after pulse compression.

The results of the experiments are shown in Fig. 4.18 (raw data). The notch filter evaluation is shown in Fig. 4.19. The subfigures (a), (b) and (c) show the experimental outcome for iris values 61, 63 and 68, respectively, in both figures. A TD lineout over the energy range between 36 and 45 eV is obtained and shown in Fig. 4.20. The curves for the measurements at high NIR intensity, iris 61 and 63, exhibit similar time-delay modification, whereas the one for iris 68 changes linearly in the other direction. In this measurement, the data, obtained at iris 68 serve as a background value, because at iris 68 no NIR laser pulse reaches the target chamber with the H_2 target gas. It therefore corresponds to a measurement analog to the background measurement for finding out the sensitivity of the experimental apparatus, Fig. 4.12, with both data sets exhibiting the same linear change in the ΔOD signal (in amplitude).

4.3.3 Data Interpretation and Outlook on Data Analysis

Looking at Fig. 4.20 and agreeing that signatures of absorption signal changes have been measured, even beeing only slightly more intensive than the effects measured due to systematic problems, the following interpretation of the measured data for iris set values 61 and 63 can be given. Before conducting the experiments, searching for the Q_n resonances of molecular hydrogen in absorption signals, i.e. looking for changes in the continuum absorption due to the autoionazing character of the Q_n states, a change in the absorption signal, similarly as for the autoionizing states in helium and argon, Sec. 4.2.3, was expected. The time delay lineouts were believed to show change, different than an overall constant ΔOD offset, depending on which TD position is chosen as a reference value for the calculation of ΔOD. Since for all experiments, we have taken as a reference the spectra, measured for the most negative TD in the time delay range, we expected to see a "dip", i.e. less ΔOD signal, around zero TD. This would mean less absorption because of the autoionizing nature of the Q_n states. What we at the end measure partly resembles the initial prediction. Namely, the TD-ΔOD-lineout is constant for both negative and positive TD but it changes in strength around zero TD. To imagine what happens in the hydrogen molecule for both time-delay regions we recall the convention, employed in this thesis for the sign of a TD, Fig. 1.3, overlaying both figures in Fig. 4.21. For very far positive TDs we only measure absorption in the XUV light field, since the coherent time of molecular dissociating states is restricted to the Franck-Condon region. The wavefunction,

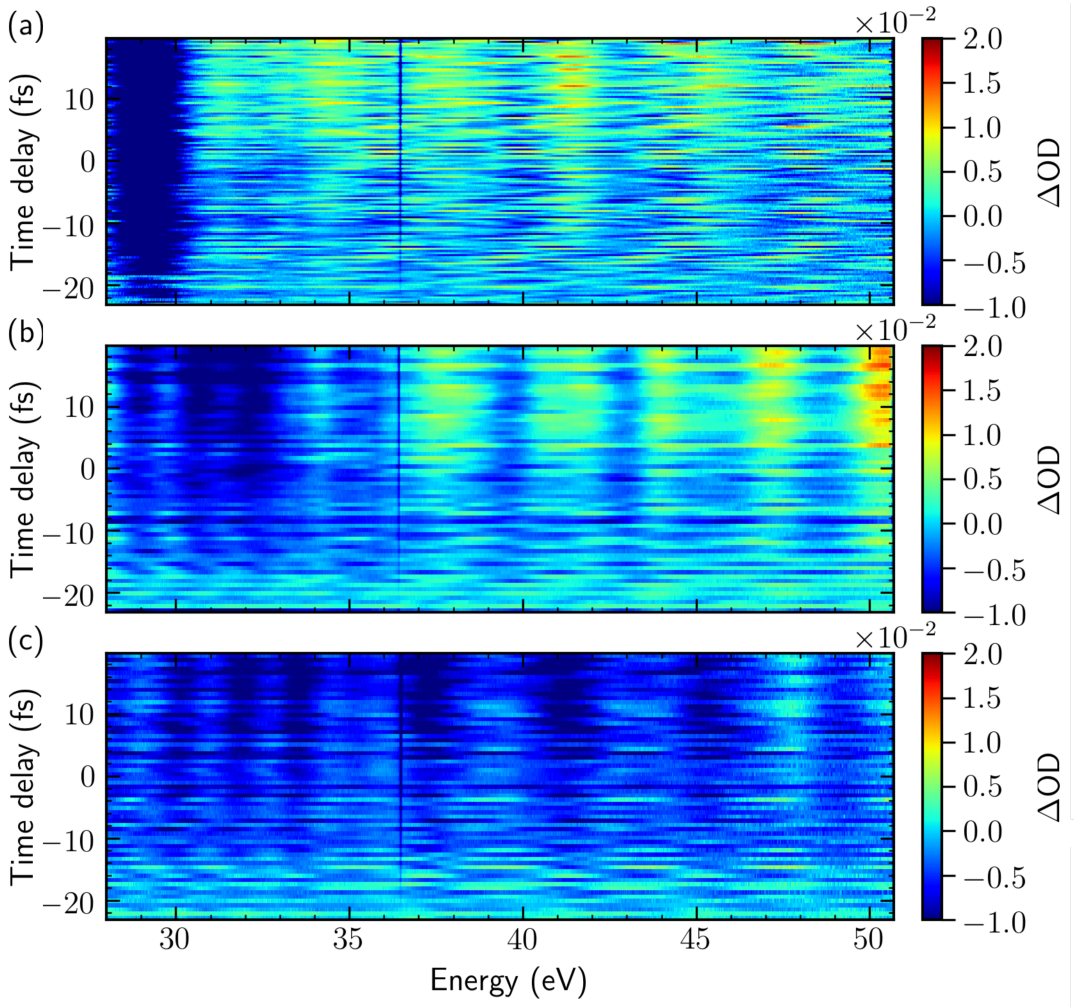

Figure 4.18: Raw data of TD-Scans in hydrogen in the energy region between 28 and 51 eV **(a)**,**(b)** and **(c)** obtained when measuring ΔOD for iris set values, 61, 63 and 68, respectively. The line around 36.4 eV is aluminium filter absorption cutoff in the second order, visible because of the slight energy shift with TD.

populating the Q_n states, however stays in this region only for a few femtoseconds at most. The transient coupling scheme is therefore not applicable for large time delays. The attenuation of the signal for negative TDs, compared to the reference case of only XUV absorption (large positive TDs), is due to changes in the ground state population of molecular hydrogen because of the NIR laser pulse coming before the XUV light pulse. The NIR pulse is already strong enough to ionize part of the H_2 molecules in the interaction region via tunneling ionization. An indication for such an ionization effect for negative TDs is the fact, that for iris set values 61 and 63 are near the XUV generation threshold in the HHG process driven by the NIR pulse, 4.5. The knee structure in the measured ΔOD arises because the absorption cross section values of the H_2^+ ion are different than the overall ionization cross sections of H_2 in the energy region of the presented measurements.

To conclude this section, all data presented in this chapter could be even further analyzed, which has to be subject of future studies and goes beyond the scope of this thesis. To mention

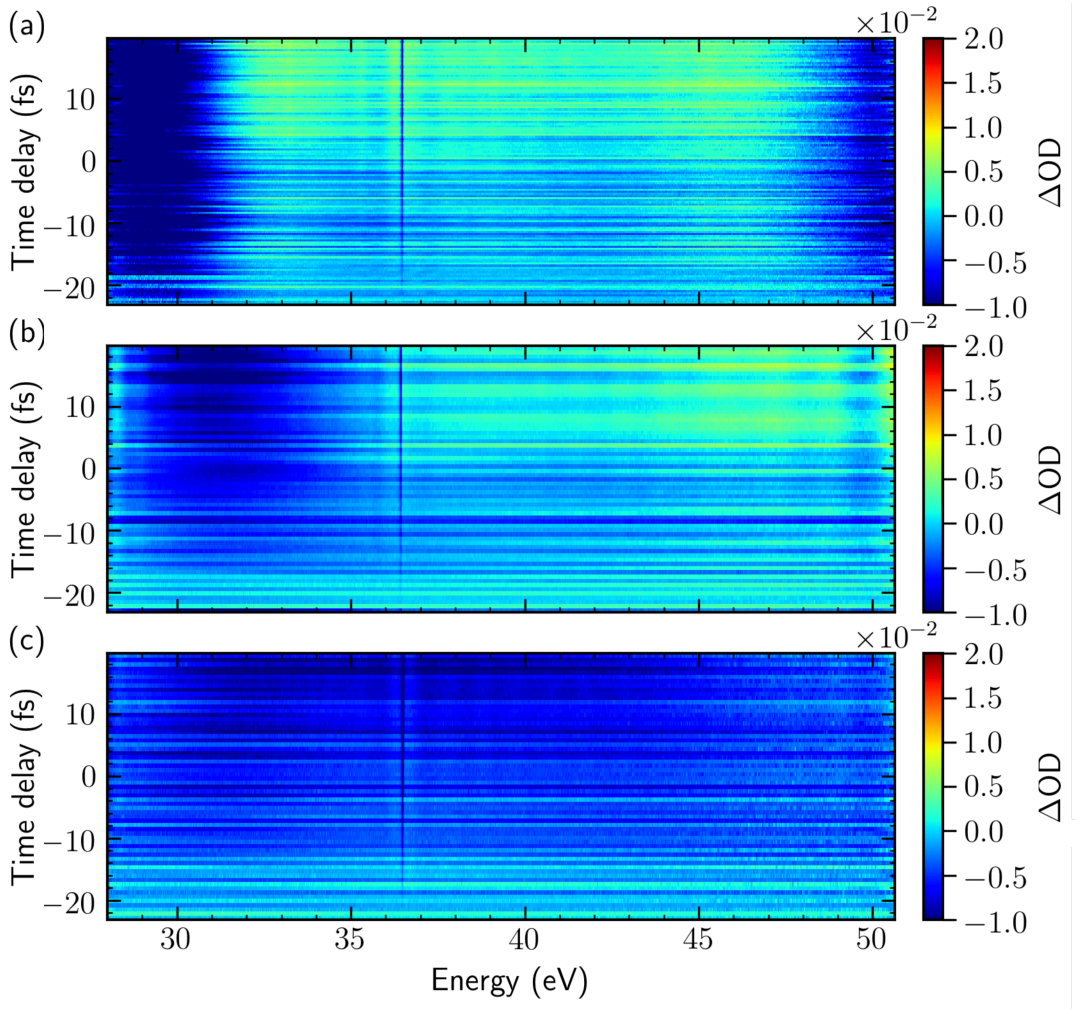

Figure 4.19: TD-Scans in hydrogen in the energy region between 36 and 45 eV from data analyzed with a notch filter

(a),**(b)** and **(c)** obtained when analyzing the ΔOD signal using a notch filter to remove the remaining harmonics modulation in the raw data for iris set values, 61, 63 and 68, respectively.

only but a few possibilities:

- Absorption change due to pressure difference in H_2: all true effects should scale with the target gas pressure in a linear way
- Evaluating the raw ΔOD data not with a notch filter but instead
  – employing proper energy backschifting, as described in Figs 4.8 and 4.9
  – building a sliding average of the data over a harmonics remaining modulation cycle
  – referencing each TD to an averaged value for the same TD over one cycle of the harmonics remaining modulation
  – rereferencing to another TD and not the most negative measured, thus shifting the offset of the TD-ΔOD-lineouts
- Continuing the course of the data analysis in this chapter by looking for energy-dependent

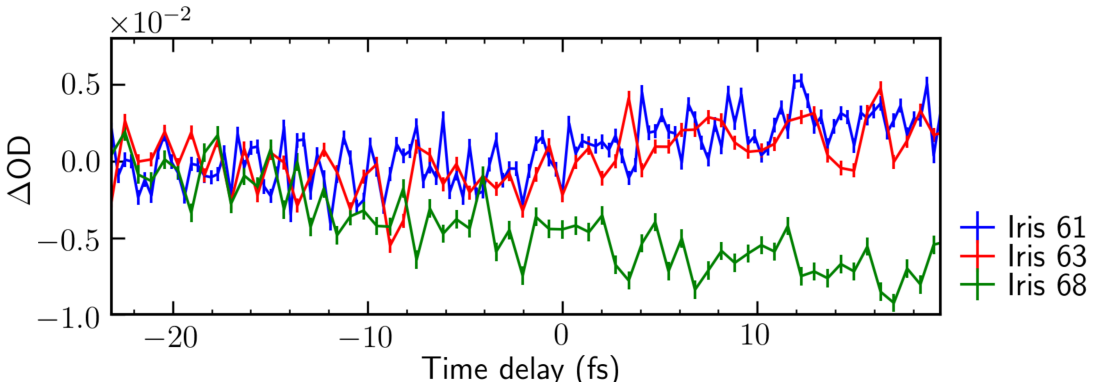

Figure 4.20: TD lineout over the energy region between 29 and 49.5 eV obtained from the notch-filtered data

The energy region for the TD lineout is constrained between 36 and 45 eV, since for energy less than 36 eV light in the second order diffraction order of the spectrometer is detected but the relevant energy region is in the first diffraction order.

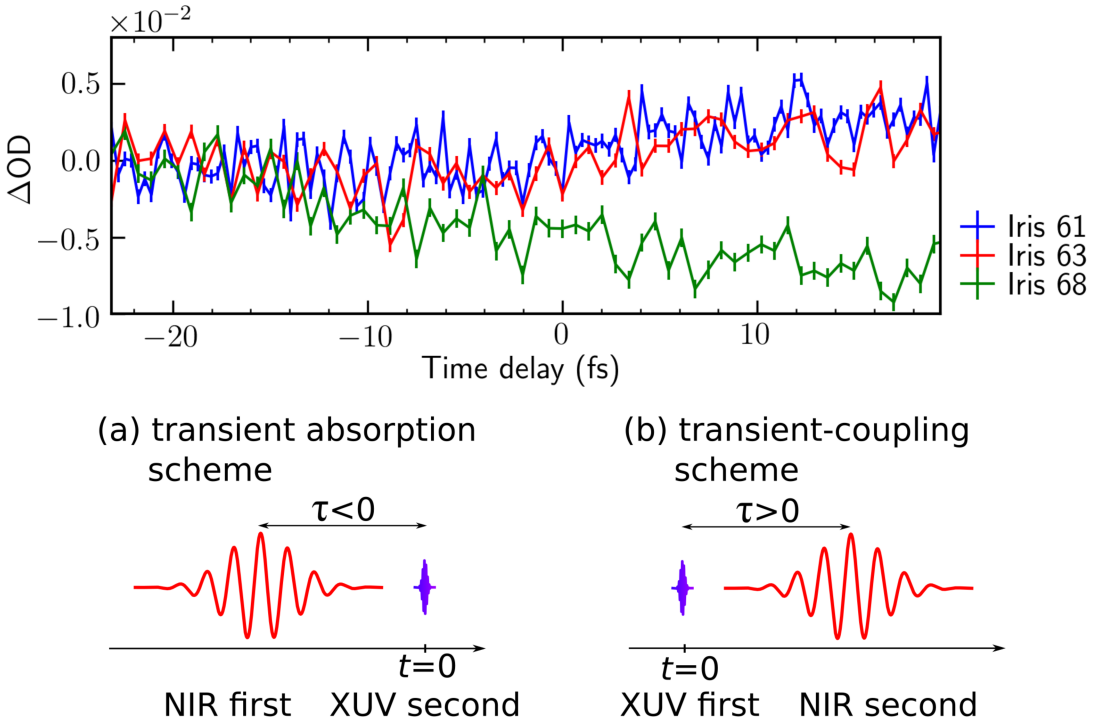

Figure 4.21: Figures 1.3 and 4.21 overlayed

The sketch, showing the TD-sign convention should help considering the physical meaning of the measured change in time-dependent ΔOD signals.

effects, as suggested by the data presented in Fig. 4.22.

All mentioned data analysis approaches should serve as an outlook on forthcoming work on the H_2 project, dealing with tiny absorption effects due to the Q_n doubly excited states of molecular hydrogen.

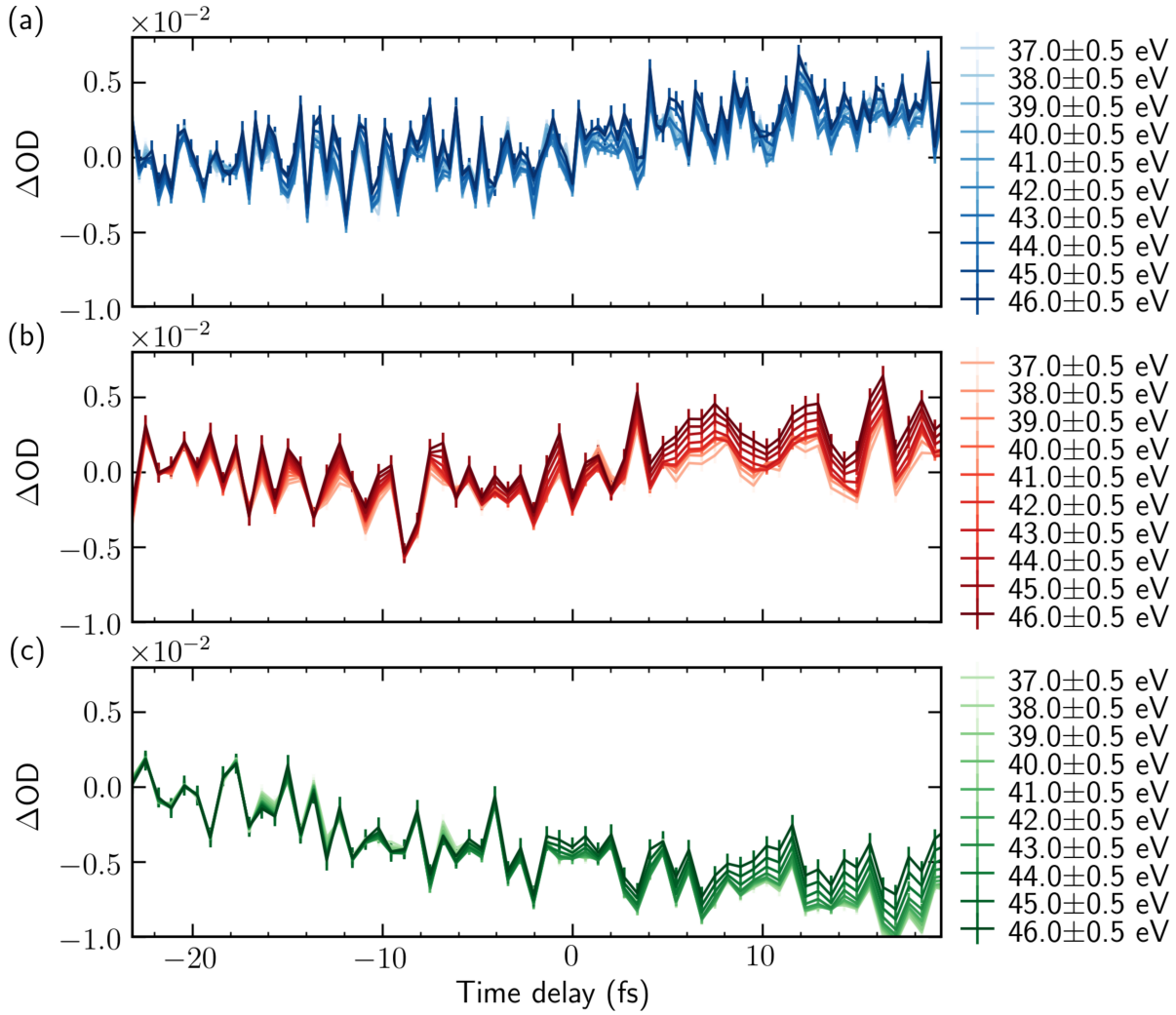

Figure 4.22: Energy dependence of the TD lineouts
(a),**(b)** and **(c)** obtained from the notch-filtered ΔOD data for iris set values, 61, 63 and 68, respectively.

4.4 A Two-Electron Model System of the Hydrogen Molecule

Parallel to the experimental studies in H_2, a two-electron model system of the hydrogen molecule was developed. The model treats each electron as well as each nucleus in one dimension, in the Born-Oppenheimer approximation, which is the assumption that the motion of nuclei and electrons can be separated [61]. The Born-Oppenheimer approximation, therefore, allows to separate the total wave function of a quantum system Ψ_{tot} into its electronic, Ψ_{el}, and nuclear, Ψ_n components:

$$\Psi_{tot} = \Psi_{el} \times \Psi_n. \tag{4.3}$$

In the here presented approach, both electrons are treated quantum-mechanically in a TDSE grid simulation, whereas the nuclei would move according to the classical Newtonian equations, thus replacing the wave-function probability approach for the the nuclear part with pointlike nuclei.

This chapter will only give an overview of the two-electron model system of the hydrogen

molecule. Its numerical implementation has been achieved within the scope of this thesis, however, no results of light-matter interaction simulations have been used to be compared to the experimental data, since the main interest of the hydrogen molecular studies was by all means the experimental part, presented in the previous section. The theoretical concepts being the basis for the numerical model implementation discussed in this section are briefly introduced in the following.

4.4.1 Theoretical Description of the Hydrogen Molecular System

Under the assumption that the laser field is linearly polarized and most of the dynamics in the studied molecular system occurs in the laser polarization direction, both electrons and nuclei are restricted to movement only in one dimension. In the following R_1 and R_2 indicate the positions of the nuclei, and x_1 and x_2 the electron positions. The masses of the nuclei and of the electrons are labeled as M and m, in atomic units: $M \approx 1836$ a.u. and $m = 1$ a.u..

The total Hamiltonian of the system, consisting of two nuclei and two electrons, is then given by:

$$\mathscr{H}_{\text{total}} = -\frac{\hbar^2}{2m}\left(\frac{\partial^2}{\partial x_1^2} + \frac{\partial^2}{\partial x_2^2}\right) - \frac{\hbar^2}{2M}\left(\frac{\partial^2}{\partial R_1^2} + \frac{\partial^2}{\partial R_2^2}\right) + U(R_1, R_2, x_1, x_2), \tag{4.4}$$

where $U(R_1, R_2, x_1, x_2)$ denotes the static potential. Considering light-matter interactions, the Hamiltonian is modified by $V(R_1, R_2, x_1, x_2; t)$ the time-dependent interaction potential with an external laser field:

$$\mathscr{H} = \mathscr{H}_{\text{total}} + V(R_1, R_2, x_1, x_2; t). \tag{4.5}$$

The potential energy of the system in the soft-core approximation is given by

$$U(R_1, R_2, x_1, x_2) = \sum_{i,j=1}^{2}\left(-\frac{e^2}{\sqrt{\left(x_i - R_j\right)^2 + a_{\text{en}}}}\right) + \frac{e^2}{\sqrt{(x_1 - x_2)^2 + a_{\text{e}}}} + \frac{e^2}{\sqrt{(R_1 - R_2)^2 + a_{\text{n}}}} \tag{4.6}$$

with the elementary charge $e = 1$ a.u.. In the dipole approximation, used throughout this work, the laser-molecule interaction energy reads

$$V(R_1, R_2, x_1, x_2; t) = e(x_1 + x_2 - R_1 - R_2)E(t), \tag{4.7}$$

with $E(t)$ being the time-dependent laser electric field strength in atomic units. Note that a soft-core potential, as in chapter 3, is used to model the relevant electrostatic interactions in order to prevent numerical divergence. The screening parameters a_{en}, a_e and a_n responsible for the softening of the interaction of the electron-nuclei, electron-electron and nucleus-nucleus interaction, respectively, are chosen so that some of the relevant parameters of the real system can be reproduced. The choice $a_{\text{en}} = a_{\text{e}} = 1.5$ a.u. and $a_{\text{n}} = 0.03$ a.u. gives $E_{\text{g}} = -1.162$ a.u. being the ground states energy of the real H_2 molecule, and equilibrium internuclear distance

$R_0 = 2.565$ a.u., differing from the real value $R_0 = 1.4$ a.u.. Such or any other choice of the soft-core parameters does not influence the qualitative description of the system.

According to the Born-Oppenheimer approximation, employed in the numerical model, the Hamiltonian for the studied system can be separated in two parts: one for the electrons and one for the nuclei, allowing to write:

$$\mathscr{H}_{\text{total}} = \mathscr{H}_{\text{el}} + \mathscr{H}_{\text{n}} \tag{4.8}$$

where

$$\mathscr{H}_{\text{el}} = -\frac{\hbar^2}{2m}\left(\frac{\partial^2}{\partial x_1^2} + \frac{\partial^2}{\partial x_2^2}\right) + U(R_1, R_2, x_1, x_2) \tag{4.9}$$

and $\mathscr{H}_{\text{n}}$ being the remaining part of total Hamiltonian, especially including the kinetic energy of the nuclei. For finding the ongoing dynamics of the electrons, the time-dependent Schrödinger equation (TDSE)

$$i\hbar\frac{\partial\Psi_{\text{el}}(x_1, x_2, t)}{\partial t} = \mathscr{H}_{\text{el}}(R_1, R_2, x_1, x_2; t)\Psi_{\text{el}}(x_1, x_2, t) \tag{4.10}$$

is solved by means of a split-step algorithm, exactly as implemented in Cha. 3.

Fixed Nuclei Approach for the Bare Molecule

First of all, the focus of the attention is directed on the particular case of nuclei fixed at the positions R_1 and R_2. In this case the Schrödinger equation for the electrons is solved, for which R_1 and R_2 are considered fixed parameters in the electronic Hamiltonian. The electron coordinates x_1 and x_2 are the only dynamical variables, apart from the laser field, which is also time-dependent. The potential energy term contains an explicit dependence on the Coulomb repulsion of the nuclei, hence on the distance between the nuclei R. Since R is kept constant and does not depend on any dynamical variables, this term could be considered as a shift in the state energies of the system. However, it is taken into account so that the correct energies of the system can be obtained. To sum up, setting the nuclear positions to be fixed at all times, the motion of the electrons can be solved exactly as discussed in the helium simulation of Cha. 3.

Eigenstates and Eigenenergies of the Bare System

The electronic eigenstates and eigenenergies of the model system are found by numerically solving Eq. (4.10) by means of a recursive imaginary time propagation [43], as employed also as a preparation for the helium simulation [43]. Here, implicit energy and state dependence on the internuclear distance is assumed. For the choice of all soft-core parameters, as discussed above, ground states for a range of internuclear distances $R = \|R_1(t) - R_2(t)\|$ are condensed out of an initial random wave function. For each obtained state, the eigenenergy is calculated and plotted against R, thus obtaining the potential energy curve for the ground states of H_2, Fig. 4.23. Doing exactly the same, but considering only one electron and not two, and the respective Hamiltonian, also the ground state potential curve of H_2^+ is obtained, also plotted in Fig. 4.23.

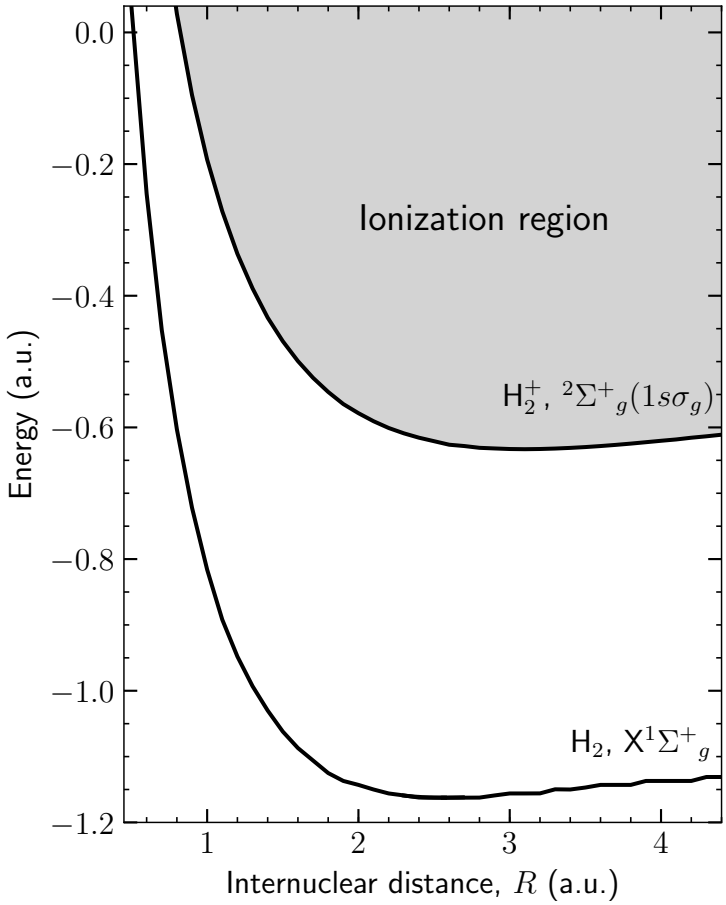

Figure 4.23: Calculated potential energy curves for the ground states of H_2 and H_2^+
H_2 ground state potential curve depending on the internuclear distance R and ionization threshold (ground state of H_2^+), obtained from a TDSE calculation with soft-core parameters as chosen in Sec. 4.4. Note that setting those parameters to other values, the potential energy curves for both the ground state and the ionization threshold would be shifted in energy and internuclear distance, but they will still have a binding character.

All states with energy and internuclear distance above the ground state potential curve of H_2^+ are embedded in the ionization continuum and can autoionize or dissociate, when populated. A selection of states condensed for obtaining the potential energy curve in Fig. 4.23 are shown in Fig. 4.24. According to the calculated potential curve for the ground state in H_2 the equilibrium distance is found to be at $R_0 = 2.565$ a.u.. The state, obtained by setting $R = R_0$ is hereafter referred as the ground state of the H_2 model system. It is plotted in Fig. 4.25.

4.4.2 The Laser-Driven Molecule

Since the main interest of this work is the laser-driven dynamics of H_2, here a numerical solution for finding the temporal evolution of the molecule is presented. Nuclear and electronic motion is separated according to the Born-Oppenheimer approximation.

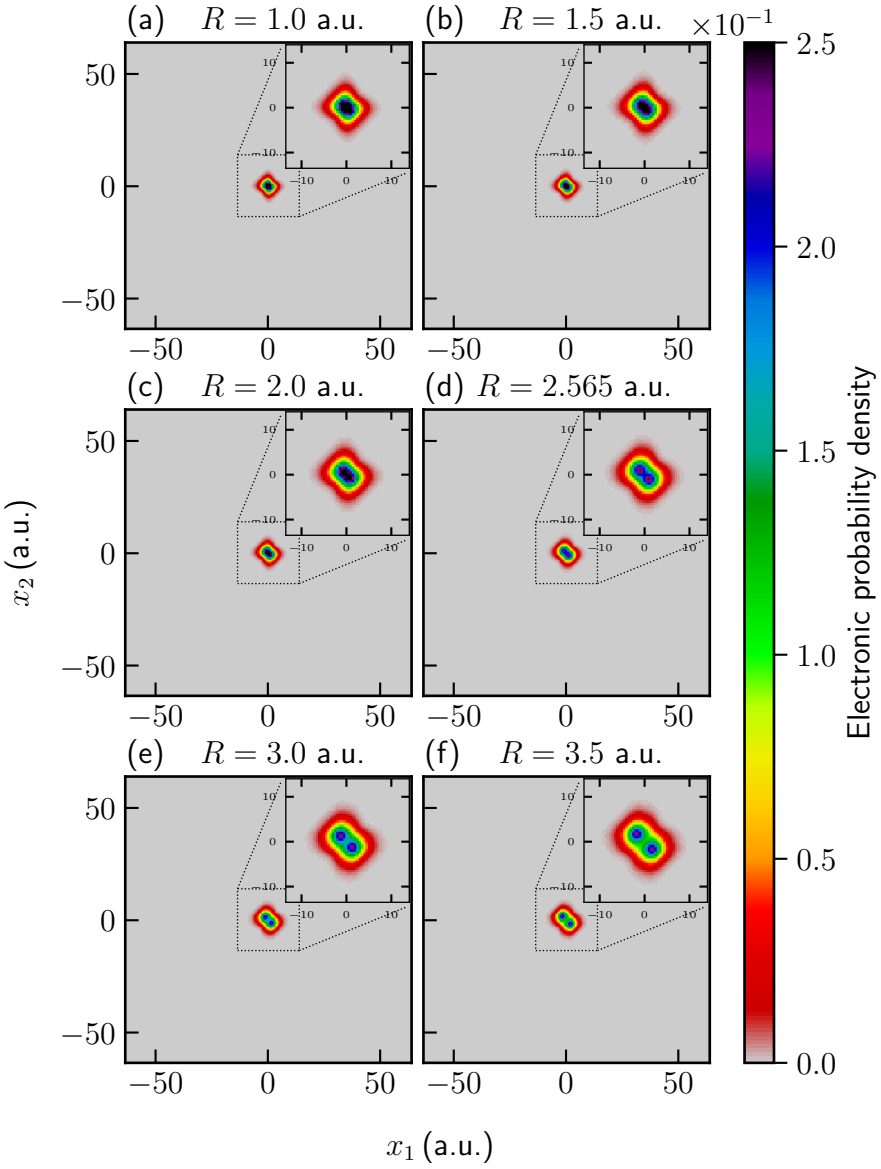

Figure 4.24: Selection of ground state wave functions with varrying intenruclear distance Ground state wave functions with internuclear distance between $R = 1.0$ a.u. and $R = 3.5$ a.u., (a) to (f), respectively. The separation between the nuclei is also imprinted in the electronic wave function, as seen in the changing central part of the shown wave functions (inset).

For finding the ongoing dynamics of the electrons, the time-dependent Schrödinger equation (TDSE) is solved:

$$i\hbar \frac{\partial \Psi_{\mathrm{el}}(x_1, x_2, t)}{\partial t} = (\mathscr{H}_{\mathrm{el}}(R_1, R_2, x_1, x_2; t) + e(x_1 + x_2)E(t))\,\Psi_{\mathrm{el}}(x_1, x_2, t) \tag{4.11}$$

with $R_1(t)$ and $R_2(t)$ being explicitly time-dependent since the nuclei are allowed to move. The difference between eq. (4.11) and eq. (4.10) is the introduction of the electron–laser interaction in eq. (4.11).

The separation of the Hamiltonian in two independent parts, hence the separation of elec-

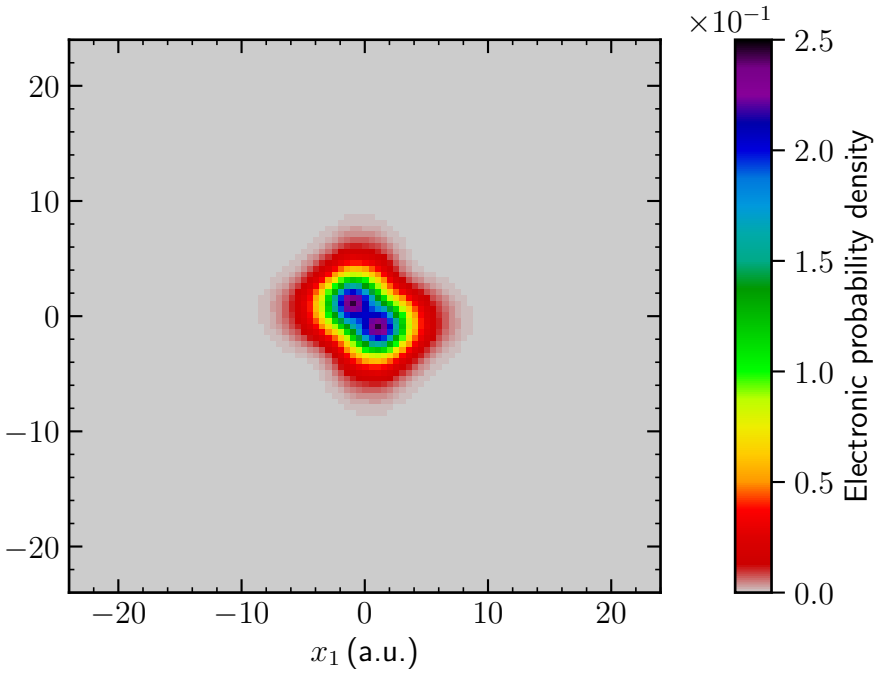

Figure 4.25: Ground state of the H_2 model system, $R_0 = 2.565$ a.u.

tronic and nuclear motion, is possible in the adiabatic approximation, which is applicable under the assumption that the electronic wave function adapts instantly to a change in the electronic Hamiltonian, i.e. to a change in the internuclear distance [61].

The nuclear motion is investigated in a classical approach, hence the time-dependent Newton equations are solved simultaneously when solving the TDSE for the electronic motion. The set of two Newton equations for the instantaneous position of the nuclei is solved by a widely-used Verlet algorithm [50] and references therein for solving coupled differential equations. The classical equations of motion read:

$$\begin{aligned} M\ddot{R}_1(t) &= F_{12}(t) + F_{1e}(t) + F_L(t), \\ M\ddot{R}_2(t) &= F_{21}(t) + F_{2e}(t) + F_L(t). \end{aligned} \tag{4.12}$$

The nuclei electrostatic interaction is

$$F_{12}(t) = e^2 \frac{R_1(t) - R_2(t)}{\left(\|R_1(t) - R_2(t)\|^2 + a_n\right)^{3/2}}, \tag{4.13}$$

with $F_{12}(t) = -F_{21}(t)$ and the force exerted on each nucleus by the laser field, in the dipole approximation, is $F_L = -eE(t)$. The force due to the electrons on the nth nucleus, $n = 1, 2$, is obtained by quantum averaging the Coulomb force, modified by the soft-core parameter a_{en},

over the electron wave function.

$$\begin{aligned} F_{ne}(t) = &- e^2 \int\int \frac{(R_n(t) - x_1)\,\|\psi(x_1, x_2, t)\|^2}{\left((R_n(t) - x_1(t))^2 + a_{en}\right)^{3/2}} \mathrm{d}x_1 \mathrm{d}x_2 \\ &- e^2 \int\int \frac{(R_n(t) - x_2)\,\|\psi(x_1, x_2, t)\|^2}{\left((R_n(t) - x_2(t))^2 + a_{en}\right)^{3/2}} \mathrm{d}x_1 \mathrm{d}x_2. \end{aligned} \tag{4.14}$$

Equations (4.11) and (4.12) must be solved simultaneously, starting from appropriately chosen initial values for the nuclei positions R_1 and R_2 and for the electron wave function $\psi(x_1, x_2, t_0)$. A favourable choice would be to start with the electronic ground state function, which is already obtained and let it interact with laser fields, an XUV and NIR pulse modelling functions for the electric field. Calculating then the dipole moment evolution of the ground state wave function, absorption spectra can be calculated for different time delays (TD-Scans), which would numerically reproduce the experiments discussed in this chapter. Alternatively, a wave function partition approach as in Cha. 3 could be employed to calculate overall ionization yields and therefore gaining insights into the ionization dynamics of the hydrogen molecule. A combined quantum and classical model simulation for the interaction of molecular hydrogen with XUV and NIR light has thus been successfully developed. Its application for a detailed study of physical observation and comparison with the experimental data however goes beyond the scope of this thesis, and has to be subject of future studies.

4.4.3 Numerical Parameters

For the sake of completeness, the relevant numerical parameters are summarized in this section. Wave functions are represented numerically in a two-dimensional discrete 256×256 grid with complex number entries at each point $\boldsymbol{x} = (x_1, x_2)$, with $\boldsymbol{x} \in \mathscr{X} = [-63.5\text{ a.u.}; -63\text{ a.u.}, \ldots, 64\text{ a.u.}] \times [-63.5\text{ a.u.}; -63\text{ a.u.}, \ldots, 64\text{ a.u.}] \cong [1, 2, \ldots, 256] \times [1, 2, \ldots, 256]$. As in Cha. 3 an absorbing boundary was employed to damp the electron occupation probability density at the borders of the considered grid. The potential used here is

$$\mathrm{Im}(\mathscr{V}) = \begin{cases} \cos^2\left(\frac{\pi}{2} \frac{r}{(R_{max} - R_{min})}\right) & \text{for } r \in [55\text{ a.u.}, 64\text{ a.u.}] \\ 0 & \text{for } r < R_{\mathrm{min}} = 55\text{ a.u.} \\ 1 & \text{for } r > R_{\mathrm{max}} = 64\text{ a.u.} \end{cases} \tag{4.15}$$

The temporal step for finding solutions of the TDSE is set to $\Delta t = 0.01$ a.u..

4.5 Brief Chapter Summary

This chapter gave a detailed overview on the transient-absorption spectroscopy studies of the (auto-)ionization dynamics of doubly excited Q_n resonant states, beginning with a brief summary on the literature research carried out parallel to the experimental and (preliminary) theoretical studies in the scope of this thesis. Fighting with systematic and statistical effects throughout the experimental investigation, which turned out to be much more severe than initially expected. After a first longterm measurement (over 85 hours data acquisition time), first results, of (auto-)ionization effects in the hydrogen molecule were obtained in an absorption spectroscopy study. Further data analysis and theoretical studies are intended to confirm the currently suggested interpretation of the evaluated data. As a direct achievement of the work presented in this thesis, the transient absorption experimental apparatus in our group has been significantly improved in its measurement protocols, allowing for absorption studies of tiny signals, down to absorbance changes on the order of 0.5×10^{-2} OD units.

Conclusions and Outlook

The main subject studied in the scope of this master's thesis was the process of ionization, especially double ionization in the theoretical work dealing with the helium system, and autoionization of doubly excited states in the absorption experiments in molecular hydrogen. The theoretically and experimentally investigated effects have something in common: they appear only in at least two-electron systems. Figuring out the driving principles of the (ionization) dynamics in species with two electrons is the first step towards understanding (the ionization of) more complex quantum systems.

First of all, the similarities and discrepancies between the two investigated systems, He and H_2, with details about their structure, were presented. The method of choice to study the intrinsic electronic processes in both helium and hydrogen is considering light–matter interactions by means of the attosecond transient-absorption spectroscopy technique and in the transient-coupling scheme. To carry out experiments and especially to understand the experimental results, detailed knowledge of the experimental setup, consisting of a femtosecond NIR laser system and a spectroscopic beamline, was required. As a result, awareness of systematic effects, being non-negligible, when looking at energetically broad absorption signals, like the Q_n-states absorption in molecular hydrogen, was raised.

In the experimental hydrogen study so far no direct autoionization effects were measured, which should have become evident through time-dependent changes in detected absorption signals. It nevertheless brought some insight into strong-field ionization of H_2 by suggesting a tunneling mechanism responsible for attenuation of the experimentally measured absorption attenuation for negative time delays between an NIR pulse, interacting first with the target system, and isolated attosecond XUV light pulse, subsequently probing the target.

Additionally to the carried out experiments in H_2, a two-electron model system of the molecule was numerically implemented, based on an already successfully used two-electron atomic model for theoretical studies of ionization dynamics in helium. Motivated by an absorption measurement in helium, theoretical results from a study of the electron dynamics in the atomic system, interacting with strong laser fields (XUV-excitation and NIR-perturbing pulse) were presented. The experimentally observed abrupt ionization of all doubly excited states in helium above a certain critical NIR intensity was linked to a double ionization effect. The theoretical results were obtained by numerically solving the one-dimensional Schrödinger equation for two electrons and employing a wave function partitioning technique to directly access the

time-dependent population of the relevant atomic states during their interaction with an NIR laser pulse. The numerical calculations confirm the experimental observations and point towards the importance of electron-electron interactions in the ionization process.

To sum up, theoretical and experimental studies of XUV multielectron (auto-)ionization dynamics in an atomic and a molecular system were carried out – helium and hydrogen, respectively. Further experimental and theoretical investigations of ionization dynamics should help gaining a more thorough understanding of the importance of electron–electron correlation effects for the ionization dynamics of both helium and molecular hydrogen.

Acknowledgments

Bevor ich zum letzten Mal das Manuskript dieser Arbeit schließe, möchte ich meinen herzlichen Dank an einigen wichtigen Personen ausdrücken. Hiermit richte ich mich an alle, die mir bei der Durchführung und dem Schreiben der Masterarbeit ihre Hilfe und Unterstützung angeboten haben.

Allermeist bin ich **Prof. Dr. Thomas Pfeifer** zu Dank verpflichtet. Mit seiner Begeisterung hat er mir gezeigt wie viel Spaß und Freude Lernen und Forschen bereiten können. In seinem vollen Terminkalender hat er magisch immer etwas Zeit geschaffen, um bei der Diskussion der neuesten Ergebnisse auch dabei zu sein. Jeder neue Vorschlag von ihm hat eine ganze neue Welt geöffnet, in der die Ergebnisse, über die man schon monatelang seinen Kopf zerbrochen hat, etwas mehr Sinn gemacht haben.

Als mein Zweitgutachter und allergrößter Auskenner des kleinsten Moleküls, H_2, hat **Priv. Doz. Dr. Robert Moshammer** häufig angeregt über die Ionisationsprozesse in Wasserstoff mitdiskutiert. Sein kritisches Auge hat mir die richtige Ansicht gegenüber Messdaten gezeigt: "Stimmt das alles?! Prüfe das da am besten nochmals, um sicher zu sein!" Herzlichen Dank dafür!

An dieser Stelle darf auch der Gruppenleiter der **InterAtto**- und **X-Music**-Teams, **Dr. Christian Ott**, sich angesprochen fühlen. Ich bedanke mich bei ihm für die Betreuung, die er mit voller Hingabe getan hat. Zusammen mit Thomas hat Christian sofort ein Projekt vorschlagen können, mit dem ich mich im Labor herausvordern konnte, wie ich mir im September 2016 vor Beginn der Masterarbeit gewünscht hatte. Mit seiner Erfahrung im Gebiet der Quantendynamik hat Christian jede Frage bezüglich Theorie und Experiment beantworten können. Auch stets hat er mich ermuntert, wenn die neuesten Messdaten doch immernoch welche unerklärbaren Effekte aufgewiesen haben, so dass letztendlich dadurch diese Arbeit entstanden ist.

Den *Chefs* wurde wohlverdient zuerst gedankt. Nun schulde ich meinen besten Dank meinen direkten Betreuern, die jeden Tag im Labor oder im Büro meinen hilfesuchenden Blick getroffen haben. Da ich mich eigentlich von allen gleichermassen betreut gefüllt habe und vor allem in den letzten Tage fühle, benenne ich sie alphabetisch: **Paul Birk, Dr. Alexander Blättermann, Maximillian Hartmann und Veit Stooß**.

Paul, der den "HHG-Knopf" erfunden hat, hat mir beigebracht mit Geduld an einem Experiment dranzugehen und jedes Mal von vorne alle technischen Aspekte der komplizierten Beamline

in Betracht zu nehmen. Diese Einstellung bringt er auch, wenn er sich gerade ausgewerteten Daten anschaut, wodurch ich häufig von ihm auf Effekte hingewiesen wurde, die man als unbedeutend bezeichnet, doch meistens eine Rolle spielen. Vielen Dank dafür!
Alex ist der lebendige Geist im Großraumbüro, der trotzdem immer nüchtern an Datenauswertung drangeht und eine große Hilfe war, um die grundlegenden Messkonzepten zu verstehen. Danke sehr für die Hilfe!
Max war stets hilfsbereit und hat sich mehrmals die Zeit genommen, um mit mir im Labor den Tag zu verbringen, da "alleine sein im Labor ja (gar) keinen Spaß macht." Vielen Dank für die Gesellschaft und Hilfe mit dem D-Scan!
Veit war mein direkter Ansprechpartner für alles, was Simulationen betrifft. Er hat mir jedes Mal weiterhelfen können, wenn ich Schwierigkeiten hatte und *Python* davon überzeugen wollte weiter mitzumachen. Auch im Labor hat mir Veit sehr viel gezeigt, so dass ich am Ende die Experimente selbst durchführen konnte, wofür ich sehr dankbar bin.
Alle InterAttos, zusammen mit Christian, haben sich auch viele Teile dieser Arbeit durchgelesen und viel dazu beigetragen, dass sie am Ende in diesem Format vorsteht.
Auch **Dr. Anne Harth** und **Dr. Martin Laux** haben mit vielen Kommentaren zur Verbesserung des Mannuskripts beigetragen, sowie bei der Durchführung einigen Experimenten, vorgestellt in dieser Arbeit, geholfen. Vielen Dank dafür.

Bei allen anderen Mitgliedern der **InterAtto-Gruppe: Yonghao Mi, Thomas Ding, Marc Rebholz, Lennart Aufleger, Patrick Rupprecht, Carina da Costa Castanhera, Arso Ivanovic, Alexander Magunia** und **Fabian Kaap** möchte ich mich für die freundschaftliche Atmosphäre bedanken. Die Zeit am MPIK während der Masterarbeit hat sehr viel Spaß gemacht.

In allen anderen Hinsichten hat mir stets **Daniel Heimfarth** bei allem geholfen und mich auch in den letzten stressigen Tagen immer ermuntert. Vielen, vielen lieben Dank!

Едно огромно благодаря за подкрепата, оказана ми от моето семейство: майка ми **Цветанка**, която винаги ме подкрепя, и баща ми **Димитър**, бдящ безмълвно над мен, както и моята по-голяма сестра **Мария**, учеща ме на постоянство и упоритост. Благодаря и на **Стефан Гандев**, който отдели от времето си, за да прочете части от тази дипломна работа!

An alle anderen, die mir auf die eine oder andere Art und Weise geholfen haben: Vielen Dank and Thank You!

Bibliography

[1] U. Fano, "Effects of Configuration Interaction on Intensities and Phase Shifts," *Physical Review*, vol. 124, pp. 1866–1878, Dec. 1961.

[2] C. Ott, *Attosecond multidimensional interferometry of single and two correlated electrons in atoms*. Dissertation, Ruperto-Carola-University of Heidelberg, Germany, 2012.

[3] A. Kaldun, *Fano Resonances in the Time Domain - understanding and controlling the absorption and emission of light*. Dissertation, Ruperto-Carola-University of Heidelberg, Germany, 2014.

[4] A. Kaldun, A. Blättermann, V. Stooß, S. Donsa, H. Wei, R. Pazourek, S. Nagele, C. Ott, C. D. Lin, J. Burgdörfer, and T. Pfeifer, "Observing the ultrafast buildup of a Fano resonance in the time domain," *Science*, vol. 354, no. 6313, pp. 738–741, 2016.

[5] A. Palacios, J. Feist, A. González-Castrillo, J. L. Sanz-Vicario, and F. Martín, "Autoionization of Molecular Hydrogen: Where do the Fano Lineshapes Go?," *ChemPhysChem*, vol. 14, no. 7, pp. 1456–1463, 2013.

[6] A. Palacios, J. L. Sanz-Vicario, and F. Martín, "Theoretical methods for attosecond electron and nuclear dynamics: applications to the H_2 molecule," *Journal of Physics B: Atomic, Molecular and Optical Physics*, vol. 48, no. 24, p. 242001, 2015.

[7] A. Fischer, A. Sperl, P. Cörlin, M. Schönwald, S. Meuren, J. Ullrich, T. Pfeifer, R. Moshammer, and A. Senftleben, "Measurement of the autoionization lifetime of the energetically lowest doubly excited $Q_1\,{}^1\Sigma_u^+$ state in H_2 using electron ejection asymmetry," *Journal of Physics B: Atomic, Molecular and Optical Physics*, vol. 47, no. 2, p. 021001, 2014.

[8] C. Ott, A. Kaldun, P. Raith, K. Meyer, M. Laux, J. Evers, C. H. Keitel, C. H. Greene, and T. Pfeifer, "Lorentz Meets Fano in Spectral Line Shapes: A Universal Phase and Its Laser Control," *Science*, vol. 340, no. 6133, pp. 716–720, 2013.

[9] A. Blättermann, *Impulsive control of the atomic dipole response in the time and frequency domain*. Dissertation, Ruperto-Carola-University of Heidelberg, Germany, 2016.

[10] "NIST Atomic Spectra Database Levels Form." http://physics.nist.gov/PhysRefData/ASD/levels_form.html.

[11] A. Burgers, D. Wintgen, and J. M. Rost, "Highly doubly excited S states of the helium atom," *Journal of Physics B: Atomic, Molecular and Optical Physics*, vol. 28, pp. 3163–3183, 1995.

[12] M. Domke, K. Schulz, G. Remmers, G. Kaindl, and D. Wintgen, "High-resolution study of 1Po double-excitation states in helium.," *Physical review. A*, vol. 53, no. 3, pp. 1424–1438, 1996.

[13] K. Schulz, G. Kaindl, M. Domke, J. D. Bozek, P. A. Heimann, A. S. Schlachter, and J. M. Rost, "Observation of New Rydberg Series and Resonances in Doubly Excited Helium at Ultrahigh Resolution," *Physical Review Letters*, vol. 77, no. 15, pp. 3086–3089, 1996.

[14] J. W. Cooper, U. Fano, and F. Prats, "Classification of Two-Electron Excitation Levels of Helium," *Phys. Rev. Lett.*, vol. 10, pp. 518–521, 1963.

[15] A. Fischer, *Dissociative Photoionization of Molecular Hydrogen, A Joint Experimental and Theoretical Study of the Electron-Electron Correlations induced by XUV Photoionization and Nuclear Dynamics on IR-Laser Dressed Transition States*. Dissertation, Ruperto-Carola-University of Heidelberg, Germany, 2015.

[16] E. M. García, J. Á. Ruiz, S. Menmuir, E. Rachlew, P. Erman, A. Kivimäki, M. Glass-Maujean, R. Richter, and M. Coreno, "Fluorescence study of doubly excited states of molecular hydrogen," *Journal of Physics B: Atomic, Molecular and Optical Physics*, vol. 39, no. 2, pp. 205–213, 2006.

[17] J.-C. Diels and W. Rudolph, *Ultrashort Laser Pulse Phenomena*. Academic Press, 2nd ed., 2006.

[18] J. W. Gallagher, C. E. Brion, J. A. R. Samson, and P. W. Langhoff, "Absolute Cross Sections for Molecular Photoabsorption, Partial Photoionization, and Ionic Photofragmentation Processes," vol. 17, no. 1, pp. 9–153, 1988.

[19] F. Martín, "Ionization and dissociation using B-splines: photoionization of the hydrogen molecule," *Journal of Physics B: Atomic, Molecular and Optical Physics*, vol. 32, pp. R197–R231, 1999.

[20] M. Glass-Maujean, "Photodissociation of doubly excited states of H_2, HD, and D_2," *The Journal of Chemical Physics*, vol. 85, no. 9, p. 4830, 1986.

[21] M. V. Ammosov, N. B. Delone, and V. P. Krainov, "Tunnel ionization of complex atoms and of atomic ions in an alternating electromagnetic field," *Sov. Phys. JETP*, vol. 64, p. 1191, 1986.

[22] L. V. Keldysh, "Ionization in the field of a strong electromagnetic wave," *Sov. Phys. JETP*, vol. 20, p. 1307, 1965.

[23] P. B. Corkum, "Plasma perspective on strong field multiphoton ionization," *Phys. Rev. Lett.*, vol. 71, no. 13, pp. 1994–1997, 1993.

[24] K. C. Kulander, K. J. Schafer, and J. L. Krause, "Dynamics of Short-Pulse Excitation, Ionization and Harmonic Conversion," in *Super-Intense Laser-Atom Physics III* (B. Piraux, A. L'Huillier, and K. Rzazewski, eds.), vol. 316, pp. 95–110, Springer, Boston, MA, 1993.

[25] D. Attwood and A. Sakdinawat, *X-Rays and Extreme Ultraviolet Radiation: Principles and Applications*. Cambridge University Press, 2 ed., 2017.

[26] "CEP4^{TM} Module for FEMTOSOURCE^{TM} rainbow^{TM}, Operator's Manual," tech. rep., FEMTOLASERS Produktions GmbH, 12 2013.

[27] H. Telle, G. Steinmeyer, A. Dunlop, J. Stenger, D. Sutter, and U. Keller, "Carrier-envelope offset phase control: A novel concept for absolute optical frequency measurement and ultrashort pulse generation," *Applied Physics B*, vol. 69, pp. 327–332, 1999.

[28] F. Lücking, A. Assion, A. Apolonski, F. Krausz, and G. Steinmeyer, "Long-term carrier-envelope-phase-stable few-cycle pulses by use of the feed-forward method," *Optics Letters*, vol. 37, pp. 2076–2078, 2012.

[29] S. Koke, C. Grebing, H. Frei, A. Anderson, A. Assion, and G. Steinmeyer, "Direct frequency comb synthesis with arbitrary offset and short-noise-limited phase noise," *Nature Photonics*, vol. 4, pp. 462–465, 2010.

[30] V. Stooß, *Time-resolved strong field effects in Helium observed with transient absorption spectroscopy*. Master's thesis, Ruperto-Carola-University of Heidelberg, Germany, 2015.

[31] M. D. Hartmann, *Characterization of Few-Cycle Laser Pulses*. Master's thesis, Ruperto-Carola-University of Heidelberg, Germany, 2016.

[32] P. Birk, *Time-dependent Strong-Field Effects in Atoms and Molecules observed by Attosecond Transient Absorption Spectroscopy*. Master's thesis, Ruperto-Carola-University of Heidelberg, Germany, 2016.

[33] M. Schönwald, *Phase-matched few-cycle high-harmonic generation: ionisation gating and half-cycle cutoffs*. Diploma thesis, Ruperto-Carola-University of Heidelberg, Germany, 2010.

[34] C. Ott, A. Kaldun, L. Argenti, P. Raith, K. Meyer, M. Laux, Y. Zhang, A. Blättermann, S. Hagstotz, T. Ding, R. Heck, J. Madroñero, F. Martín, and T. Pfeifer, "Reconstruction

and control of a time-dependent two-electron wave packet," *Nature*, vol. 516, no. December, pp. 374–378, 2014.

[35] A. Ivanovic, *In preparation*. Master's thesis, Ruperto-Carola-University of Heidelberg, Germany, 2017.

[36] "Lebow Co.." `http://henke.lbl.gov/optical_constants/`.

[37] L. Aufleger, *Measurement of electron dynamics in atoms and molecules with intense XUV FEL radiation*. Master's thesis, Ruperto-Carola-University of Heidelberg, Germany, 2016.

[38] T. Ding, *Quantum dynamics in weak and strong fields measured by XUV nonlinear spectroscopy*. Dissertation, Ruperto-Carola-University of Heidelberg, Germany, 2017, submitted.

[39] C. Ott, A. Kaldun, P. Raith, K. Meyer, M. Laux, J. Evers, C. H. Keitel, C. H. Greene, and T. Pfeifer, "Lorentz Meets Fano in Spectral Line Shapes: A Universal Phase and Its Laser Control," *Science*, vol. 340, no. May, pp. 716–720, 2013.

[40] R. Grobe and J. H. Eberly, "Photoelectron spectra for a two-electron system in a strong laser field," *Physical Review Letters*, vol. 68, no. 19, pp. 2905–2908, 1992.

[41] R. Grobe and J. H. Eberly, "One-dimensional model of a negative ion and its interaction with laser fields," *Physical Review A*, vol. 48, no. 6, pp. 4664–4681, 1993.

[42] T. Ding, *Modellatom mit zwei Elektronen in jeweils einer Raumdimension in Wechselwirkung mit XUV- und IR-Laserfeldern*. Bachelor's thesis, Ruprecht-Karls-Universität Heidelberg, 2010.

[43] G. D. Borisova, *Einfluss der Elektron-Elektron-Korrelation auf die Ionisation von Atomen in starken, ultrakurzen Laser-Impulsen*. Bachelor's thesis, Ruprecht-Karls-Universität Heidelberg, Deutschland, 2015.

[44] S. L. Haan, R. Grobe, and J. H. Eberly, "Numerical study of autoionizing states in completely correlated two-electron systems," *Phys. Rev. A*, vol. 50, pp. 378–391, 1994.

[45] L. Roso, L. Plaja, P. Moreno, E. C. Jarque, J. R. V. de Aldana, J. San Roman, and C. Ruiz, "Multielectron atomic models using the Rochester one-dimensional potential," *Laser Physics*, vol. 15, no. 10, pp. 1393–1409, 2005.

[46] A. D. Bandrauk and H. Shen, "Improved exponential split operator method for solving the time-dependent Schrödinger equation," *Chemical Physics Letters*, vol. 176, pp. 428–432, 1991.

[47] D. Bauer, "Two-dimensional, two-electron model atom in a laser pulse: Exact treatment, single-active-electron analysis, time-dependent density-functional theory, classical calculations, and nonsequential ionization," *Physical Review A*, vol. 56, no. 4, pp. 3028–3039, 1997.

[48] V. Kapoor, "Autoionization in time-dependent density-functional theory," *Physical Review A*, vol. 93, no. 6, pp. 1–8, 2016.

[49] G. Lagmago Kamta and A. F. Starace, "Multielectron system in an ultrashort, intense laser field: A nonperturbative, time-dependent two-active-electron approach," *Physical Review A*, vol. 65, no. 5, p. 053418, 2002.

[50] M. Vafaee, F. Sami, B. Shokri, B. Buzari, and H. Sabzyan, "Precise description of single and double ionization of hydrogen molecule in intense laser pulses.," *The Journal of Chemical Physics*, vol. 137, no. 4, p. 044112, 2012.

[51] G. Camiolo, G. Castiglia, P. P. Corso, E. Fiordilino, and J. P. Marangos, "Two-electron systems in strong laser fields," *Physical Review A - Atomic, Molecular, and Optical Physics*, vol. 79, no. 6, p. 063401, 2009.

[52] S. Saugout, C. Cornaggia, A. Suzor-Weiner, and E. Charron, "Ultrafast electronuclear dynamics of H_2 double ionization," *Physical Review Letters*, vol. 98, no. 25, p. 253003, 2007.

[53] C. J. Latimer, K. F. Dunn, F. P. O'Neill, M. A. MacDonald, and N. Kouchi, "Photoionization of hydrogen and deuterium," *The Journal of Chemical Physics*, vol. 102, no. 2, p. 722, 1995.

[54] K. L. Ishikawa and T. Sato, "A Review on Ab Initio Approaches for Multielectron Dynamics," *IEEE Journal on Selected Topics in Quantum Electronics*, vol. 21, no. 5, p. 8700916, 2015.

[55] R. Daniele, G. Camiolo, G. Castiglia, P. Corso, F. Morales, and E. Fiordilino, "Dynamics of H_2 molecule driven by an ultra-short laser field," *Applied Physics B: Lasers and Optics*, vol. 78, no. 7-8, pp. 813–816, 2004.

[56] F. Sami, M. Vafaee, and B. Shokri, "Nuclear classical dynamics of H_2 in an intense laser field," *Journal of Physics B: Atomic, Molecular and Optical Physics*, vol. 44, no. 16, p. 165601, 2011.

[57] A. Fischer, A. Sperl, P. Cörlin, M. Schönwald, H. Rietz, A. Palacios, A. Gonzalez-Castrillo, F. Martin, T. Pfeifer, J. Ullrich, A. Senftleben, and R. Moshammer, "Electron localization involving doubly excited states in broadband extreme ultraviolet ionization of H_2," *Physical Review Letters*, vol. 110, no. 21, p. 213002, 2013.

[58] M. F. Jager, C. Ott, P. M. Kraus, C. J. Kaplan, W. Pouse, R. E. Marvel, R. F. Haglund, D. M. Neumark, and S. R. Leone, "Tracking the insulator-to-metal phase transition in VO_2 with few-femtosecond extreme UV transient absorption spectroscopy," *Proceedings of the National Academy of Sciences*, vol. 114, no. 36, pp. 9558–9563, 2017.

[59] R. Kienberger, E. Goulielmakis, M. Uiberacker, A. Baltuska, V. Yakovlev, F. Bammer, A. Scrinzi, T. Westerwalbesloh, U. Kleineberg, U. Heinzmann, M. Drescher, and F. Krausz, "Atomic transient recorder," *Nature*, vol. 427, p. 817, 2004.

[60] H. Wang, M. Chini, S. Chen, C. H. Zhang, F. He, Y. Cheng, Y. Wu, U. Thumm, and Z. Chang, "Attosecond time-resolved autoionization of argon," *Physical Review Letters*, vol. 105, no. 14, p. 143002, 2010.

[61] J. J. Sakurai and J. Napolitano, *Modern Quantum Mechanics*. Addison Wesley, 2010.

Erklärung

Diese Arbeit ist von mir selbstständig verfasst worden. Ich habe keine anderen als die von mir angegebenen Quellen und Hilfsmittel benutzt.

Heidelberg, den 01.12.2017 .....